Solidification and Segregation in Continuously Cast Steel

鋼の連続鋳造における凝固と偏析に関する研究

by

Toshio Fujimura

A thesis submitted in partial fulfilment for the requirements for the degree of Doctor of philosophy in Engineering

Hokkaido University
Sapporo, Japan

September 2018

ABSTRACT

In this study, the approximate analytical solutions for the solidus temperature which strongly depends on the steel composition were sought as the part of the solutions of the nonlinear heat- and solutes- transfer equations in the mushy zone of the continuously cast steel. Because the conventional theories of the solidification of the multicomponent steel were not well grounded due to the highly nonlinear phenomenon complicated by the time depending phase change interface. Neither analytic nor approximate solutions existed that describe the relation between the size of the mushy zone (the solid-liquid zone) and the volumetric energy generation. In addition, owing to the lack of the reliable measurements in the real casting process due to the difficulties of measurements, the significant discrepancies exist between the estimates of the solidus temperature and the thermo-analytical measurements by the small specimens of the various grades steel. This may cause the considerable errors in the accuracy of the numerical heat analysis to estimate the shell thickness and the solid fraction at the target point in the mushy zone of the continuously cast steel. The simultaneous solutions of the non-linear heat- and solutes equations were sought step by step through the three model, assuming the linear relation between solid fraction and temperature in the mushy zone.

(1) Model I: Develop the mathematical treatment to simultaneously solve the heat- and solutes- transfer equations, with the simple boundary conditions (Dirichlet conditions), adopting the measured solidification constants which represent the boundary positions with respect to time. (2) Model II: Incorporate the Neumann's boundary conditions (*i.e.,* equal derivative values at the boundary front and back) which are generally used in the numerical analysis for the solid- liquid zone in the model. The solidification of the Fe-C binary steel was investigated to make the model as simple as possible. The model predictions were in good agreement with the numerical heat analysis and were also consistent with Neumann's solution at the low carbon range. (3) Model III: Obtain the solidus temperature of the multicomponent general steel by expanding the Model II to the multicomponent steel. The predicted solidus temperatures of the various grades steel were in reasonable agreement with the measured zero ductility temperature of the high manganese steel and the thermo- analytical measurements. It was also shown that the conventional numerical heat analysis, such as the equivalent specific heat method, adopting the solidus temperature predicted by the model was in good agreement with that of Model III. The model can reduce the extensive numerical computational load to seek the solidus temperature.

The models and the predicted solidus temperature were, subsequently, used in the numerical heat analyses to estimate the solid fraction at which the electro magnetic stirring was applied in the continuously cast steel

slabs. The industrial findings with these numerical heat analyses and the analog study with Pb-Sn alloy showed that the stirring at the low fraction solid was important to refine crystals and to improve the macro-segregations, in the continuously cast steel.

The methods to transform the partial differential equations to ordinary equations and the boundary conditions adopted in the models were as shown in Table 1.

Table 1 The main objective of the model, the method to transform the partial differential equations (P.D.E) to the ordinary differential equations and the boundary conditions adopted in models

		Model I	Model II	Model III
Main objective of the model		Develop the mathematical treatment to solve the equations	Incorporate the Neumann's boundary conditions,	Obtain the solidus temperature of the multicomponent general steel
Steel type		Multi-component alloy steel	Fe-C Binary steel	Multi-component alloy steel
Analyzed zone		— a solid-liquid zone —	a sold zone a solid-liquid zone a liquid zone	a solid zone a solid-liquid zone a liquid zone
Method to transform P.D.E. to ordinary differential equations		Moving coordinate method	Similarity value method	Similarity value method
Boundary conditions	Dirichlet conditions (Constant boundary values)	adopted	adopted	adopted
	Neumann conditions (Equal derivative values at the boundary front and back)	not adopted	adopted	adopted
	Solidification constants	used	not used	not used

TABLE OF CONTENTS

Chapter 1

INTRODUCTION

1.1 Development of the Technology in the Steelmaking Process

The blast furnace on the landfill in Chiba works, Kawasaki steel (JFE Steel), put into operation in June 1953, brought an increase in the momentum of productivity that continued throughout the ensuing decades. Since then, Japanese steel industries devoted the effort to modernizing its plants and increasing its production capacity to keep its competitive edge, based on the early use of new technology. In the steelmaking shops, LD converters (Linz-Donawitz converters with the oxygen blowing through the top lance commercialized in 1952-1953) started in operations in the place of the open hearth furnaces and the continuous casters were also constructed in succession. The expansion continued through 1970's and the basic technologies of these facilities drastically increased the capacity to produce the semi-finished products, slabs or blooms. Fig.1.1 shows the typical process flow in the integrated steel works.

In the following period (1975-), the new technologies, such as the bottom blowing through the oxygen hearths installed in the bottom of the converter [1], spurred the developments in the refining process. The oxygen potential of the molten steel was considerably reduced by both of the strong stirring in converters and secondary refining process. In addition, the newly developed process of the hot metal pretreatment (removing silicon-phosphorous-sulfur of the hot metal in advance of the refining at the LD converters) increased the productivities of the high grades steel [2,3]. The casting methods for the clean steel were also developed. These newly developed processes warranted the surface qualities of the ultra-low carbon steel sheets for automobiles in the cold mill adopting the continuous annealing process (the cleanliness of the steel is essential to reduce the defects such as blisters and sliver defects of the ultra-low carbon steel because the ultra-low carbon sheets are highly sensitive to the oxide inclusions).

The technologies developed in the continuous casting were shown in Fig.1.2 The drastic improvement in controlling the casting process, *i.e.,* controlling of the surface temperature based on the thermal analysis of the continuous casting, also warranted the surface qualities of slabs for the high grades steel for plate use or pipe use. The technologies to prevent the internal cracks and the irregular macro segregations in slabs or blooms also warranted the mechanical properties of the high grades steel products. The electro-magnetic stirrers installed in a mould or at the strands of the caster reduced the macro-segregations (*i.e*., centerline segregation) in the central region of slabs or blooms [4-7]. The unique developments were also made by T. Fujimura et al. [8] and H. Kojima et al. [9] to continuously forge the solidifying shells of the blooms. This continuous forging

process drastically improved the durability of the inner race products for bearing use and the ductile fracture of the steel for bar use. However, the further improvements of the segregations in slabs or blooms are necessary to meet the more severe requirements for the high grades steel products.

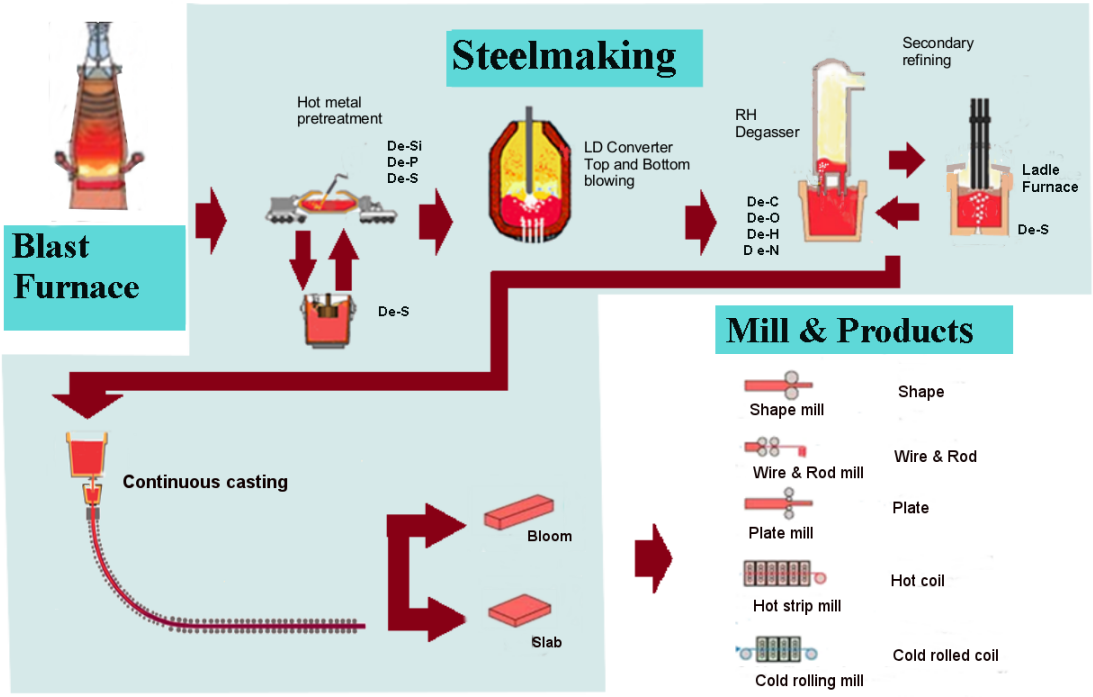

,

Fig.1.1 Process flow of the typical steel works.

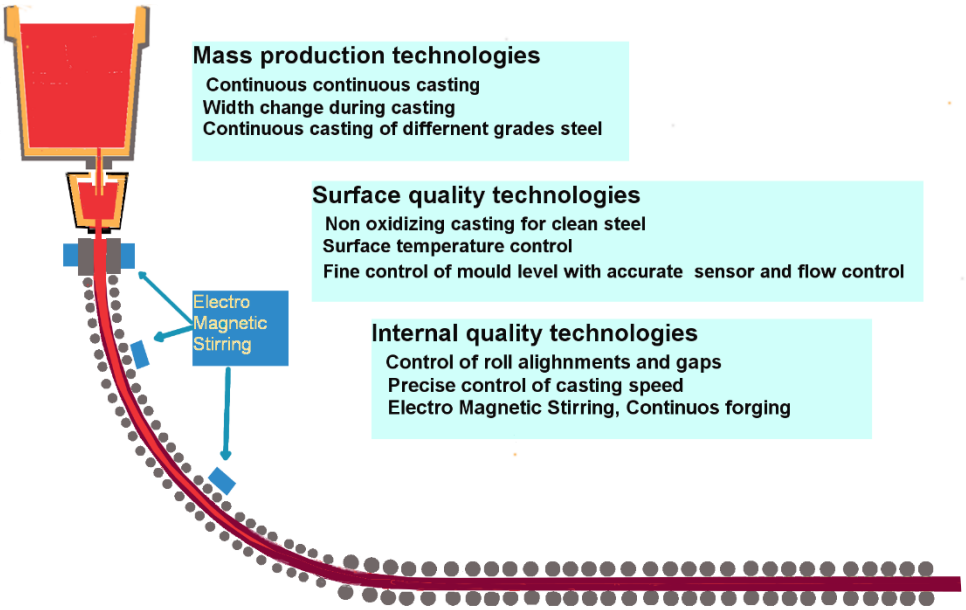

Fig.1.2 Technologies developed in the continuous casting process.

1.2 Segregation and Theories of Solidification

The schematic of the solidification of the general steel in the continuous caster is shown in Fig.1.3. The solidification of the molten steel begins in a water-cooled mould, followed by the water spraying in the strands of the caster. A mushy zone forms at the solidification front where both solid and liquid exist. It typically has a complicated, irregular morphology as dendrites grow. The latent heat is generated in accordance with the growth of the solid dendrite. At the same time, the solutes, generally are rejected from the solid into the liquid because of the low solubility of alloy elements in solid comparing to that in liquid. The solutes balance of the inflows from solid and the outflows by diffusions yields the solutes enriched liquid at the vicinity of the root of the primary dendrite (or secondary arms, Fig.1.3). The solidus temperature at these solute enriched regions decreased in accordance with the concentrations of solutes. Thus, hence, the amount of the latent heat generation and the solutes concentrations are linked together through the change of the solid fraction in the mushy zone. However, many of models focus, in general, only on the heat balance or on the solutes balances in the mushy zone because of the complexity of the problems.

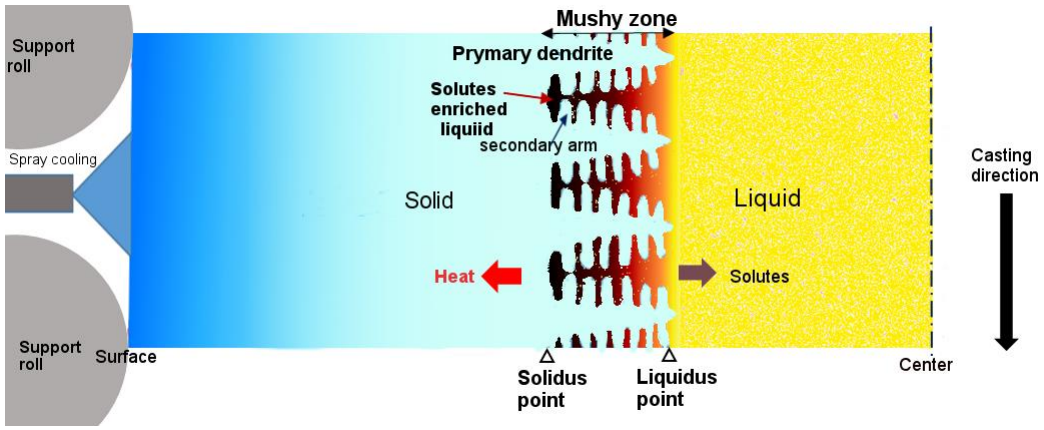

Fig.1.3 Schematic of the solidification of the continuously cast steel.

The segregation may appear on the micro scale between dendrite arms or on the larger macro or semi-macro scale. Macro and semi-macro segregations in the central region of slabs or blooms are particularly undesirable in slabs for plate application because they may give rise to welding cracks, ultrasonic-inspection defects, hydrogen-induced cracks. Ohashi et al. [10] reported the precipitated MnS inclusion deteriorated both the ductile fracture and brittle fracture of the steel plate. It was also found that manganese and phosphorous in the segregated region of the steel plate decreased the nil-ductility transition temperature in notch tensile tests due

to the transformation to the multensite-bainite duplex structure. The hydrogen induced cracks are also induced by the segregations of manganese and phosphorous [11]. The macro or semi-macro segregations appear at the centerline or as spots distributed in the central region in continuously cast slabs.

To control the process and to reduce these macro segregations, the thermal analyses of the solidification are indispensable. The numerical thermal analyses provide reliable surface temperatures (*i.e.*, those calibrated with the measured values). However, these analyses do not always provide the accurate solidification profiles because the inner temperatures are not generally calibrated with the actual (measured) values. In particular, the solidus position with the associated solidus temperature is hardly checked by measurements.

The main reason for these problems lies in the difficulty [12] of achieving reliable measurements of the solidus temperature of general steel in a real casting process (these measurements are difficult owing to the unavailability of a small durable sensor to detect the infinitesimal change of temperature at the high temperature range over 1700K). In addition, the fraction of solid in a mushy zone remains unclarified [13,14]. It should be noted that the problems of the solidification with a mushy zone are frequently referred to as the Stefan [15] boundary problem which is a nonlinear phenomenon, complicated by a time depending phase change interface.

The morphology of a mushy zone is difficult to predict and no analytic solutions are known to exist that describe the relation between the size of a mushy zone and volumetric heat generation [13].

With respect to the liquidus temperature, while it is not also generally measured during the casting process, the problems are not serious because microsegregation at the dendrite tips is so small that super-cooling is limited to only a few degrees. Therefore, the liquidus temperature for general steel can be estimated from the phase diagram or from measurements, which are in reasonable agreement with each other. However, with regard to the solidus temperature of steel, significant discrepancies exist among the estimates based on the phase diagram and models accounting for microsegregation. (*i.e.*, 40 K discrepancies [16–18]). Recently, Gryc et al. [19] thermo-analytically measured the solidus temperature of the small specimens for various grades steel and reported significant discrepancies between the measurements and the values obtained from the reported formulae (up to 42 K) or thermodynamic calculations (up to 50 K). These discrepancies could lead to considerable errors in estimating the shell thickness with respect to time. These errors may give the fatal errors to estimate the solid fraction in the mushy zone at the target position because the magnitude of these errors are almost even to that of the solidification range ΔT (from the liquidus temperature to the solidus temperature, *i.e.*, 40K for 0.15%C,0.7%Mn,0.22%Si general steel).

The lack of knowledge about the fraction of solid in the mushy zone has spurred the onset of numerous methods

based on heat analysis. They can be classified into three major models (A)–(C): (A) methods [20–22] assuming a linear relationship between the solid fraction and the temperature (*e.g.*, equivalent specific heat model); (B) methods [23,24] based on the equilibrium lever rule, the Scheil equation, and back diffusion models [25–29]; (C) methods [30] recovering the temperature with the latent heat release after solidification. However, these methods are not always consistent with the real solidification process. For example, (C) methods assume that the primary dendrites should grow after solidification. When the (B) methods such as Scheil equation with a large domain are used along the dendrite axial direction, a flat boundary surface should be assumed for the dendritic mushy zone. Thus, the fraction of solid used in the thermal analysis should be consistent with general solidification.

Instead of a large domain, for the (B) methods with a small scale of domain, as small as a secondary arm spacing, the microsegregation in the dendritic mushy zone can be analytically evaluated assuming a constant cooling rate with the uniform temperature in a domain and neglecting the diffusion along the primary dendrite axis direction. The lever rule assumes the complete diffusion in both liquid and solid, while Scheil's equation assumes no diffusion of solutes in solid and complete diffusion in liquid, which are considered to be two significant limitations for microsegregation predictions (*i.e.*, infinite diffusion and negligible diffusion in solid). Because this small domain is assumed to be blockaded by secondary arms as soon as secondary arms develop. Brody & Flemings [25] developed a model to consider the back diffusion of solutes in solid with the assumption of finite diffusion in solid and complete diffusion in liquid. Clyne & Kurz [26] treated the Brody & Flemings model in a mathematical way that allowed the model approach the lever rule and Scheil's model for infinite and negligible diffusion in a solid, respectively. Ohnaka [27] considered a columnar dendrite rather than the plate dendrite and derived the model through solving the overall mass balance. Voller et al. [28] also proposed a model that considered the coarsening of secondary arms. These models are effectively used to investigate the microsegregation of numerous alloys. However, the cooling rate considerably varies during solidification and the diffusions of solutes in liquid, which are neglected in these models along the primary dendrite axis, are not negligible since the effective partition ratio of carbon is typically close to 0.9 (0.85–1.0) for continuously cast steel [31]. Furthermore, these assumptions make it difficult to incorporate the heat-transfer equation in back diffusion models, because the assumption of a constant cooling rate with the uniform temperature in a mushy zone is not always consistent with a general solidification process. In addition, the estimates of the solidus temperature by these back diffusion models are highly dependent on the assumed cooling rate.

To resolve the issue, an enlarged domain as large as a primary dendrite arm divided into small volume elements

is considered. This enlarged domain involves the continuum liquid, which allows the diffusion of the solutes along the primary dendrite axis direction (solidification direction). It should be noted that taking account of diffusion in liquid, which is much larger (generally two order magnitude larger) than that in solid, composes the limitation at the end of solidification and makes it easier to incorporate the heat transfer along the solidification direction in the diffusion model. Considering the large domain wherein both solute and heat are transferred along the primary dendrite axis direction (solidification direction), Asai et al. [32], Hills et al. [33], and Alexandrov et al. [34] obtained analytical or approximate analytical solutions for the solute- and heat-transfer simultaneous equations under a steady-state conditions (*i.e.*, constant solidification velocity). However, these analytical solutions cannot be directly used for general heat analysis because the solidification velocity significantly changes with time.

Regarding the unsteady state solidification, Takeshita [35] obtained simultaneous solutions for unsteady state solidification using an extensive numerical computation model for a NH_4Cl aqueous eutectic system (a binary system); in advance of the numerical computation, the model analytically eliminated the solid fraction-related terms in the equations in the case of negligible solute diffusion in a solid. However, to use this model for multi-component alloy steel, more complicated computations are required. Huppert et al. [36] and Alexandrov et al. [37] proposed models for aqueous chimney-type unsteady state solidifications (a binary system); their models, however, focused on particular scenarios, such as if a liquidus point develops, whereas the solidus point barely develops. This limits the applicability of their models for the solidification of steel, because the solidus point of the general steel typically develops along with an associated liquidus point during solidification. Although, thus, many models and numerical analyses were demonstrated, the solidus temperature along with the solid fraction in a mushy zone of the general steel still remains unclarified.

1.3 Objectives and Scope of the Study

The objective of this study is to analytically solve the nonlinear heat- and solutes- transfer equations in the mushy zone of the multi-component alloy steel and to obtain the solidus temperature as the part of the solutions for the unsteady state solidification [38-40]. In addition, the method to provide the more reliable numerical analysis is also sought in this study by obtaining the consistencies between the analytical solutions and the numerical analyses. It is noted that these equations are one of the Stefan problems for the solidification of the multicomponent general steel and the analytical solutions were not found to exit.

The studies were made through the three models. In chapter 2 (Model I), the mathematical treatment to simultaneously solve the heat-and solutes- transfer equations adopting the measured solidification constants was developed and examined. In chapter 3 (Model II), the mathematical treatment to solve the equations with Neumann's conditions in addition to the Dirichlet conditions for boundaries was developed. The simple case, Fe-C binary steel, was chosen. In chapter 4 (Model III), finally, the limited applicability of the model II was expanded to the multicomponent alloy steel. The solidus temperature of the general steel was obtained as aimed and compared with measurements and with those of other models. In the chapter 5, the numerical heat analyses based on these models with adopting the predicted solidus temperature were used to investigate the industrial findings on the electro-magnetic stirring to reduce the macro-segregation in the continuously cast slab in chapter 5.

1.4 Outline of the Dissertation

Chapter 1 Introduction

The background of the problems, objectives and scope of study are presented.

Chapter 2 Model I

Mathematical Analysis of Solidification Behavior in Multicomponent Alloy Steel [38]

The mathematical treatment to simultaneously solve the heat- and solutes- transfer equations is developed with the simple boundary conditions (Dirichlet conditions), adopting the measured solidification constants which represent the boundary positions with respect to time. The results were in good agreement with generally accepted values and temperature measurements. However, the solutions were not fully consistent with the conventional heat analysis [20-22] owing to insufficient boundary conditions.

Chapter 3 Model II

Mathematical Analysis of the Solidification Behavior of Plain Steel Based on Solute- and Heat-Transfer Equations in the Liquid–Solid Zone [39]

The Neumann's boundary conditions (*i.e.,* equal derivative values at the boundary front and back) which were generally used in the numerical analysis for the solid- liquid zone were incorporated into the model. The simple Fe-C binary steel was investigated to make the model as simple as possible. The model predictions were in good agreement with the numerical heat analysis and were also consistent with Neumann's solution [41] at the low carbon range.

Chapter 4 Model III

Mathematical Analysis of the Solidification Behavior of Multi-Component Alloy Steel Based on Heat- and Solute-Transfer Equations in the Liquid–Solid Zone [40]

The solidus temperature of the multicomponent general steel was obtained by expanding the Model II to the multicomponent steel. The predicted solidus temperatures of the various grades steel were in reasonable agreement with the measured zero ductility temperature of the high manganese steel [42] and the thermo- analytical measurements [19]. It was also shown that the conventional numerical heat analysis, such as the equivalent specific heat method, adopting the solidus temperature predicted by the model was in good agreement with that of Model III.

Chapter 5 ***Effect of Stirring on Crystal Morphologies and on Macro Segregation*** [6,7]

The models and the predicted solidus temperature were, subsequently, used in the numerical heat analyses to estimate the solid fraction at which the electro-magnetic stirring was applied in the continuously cast steel slabs. The industrial findings with these numerical heat analyses and the analog study with Pb-Sn alloy showed that the stirring at the low fraction solid was important to refine crystals and to improve the macro-segregations, in the continuously cast steel.

Chapter 6 Conclusion

Conclusions are presented.

References

[1] A. Ejima and K. Sanbongi, Recent Development of OBM/QBOP Steelmaking Process, Japan Institute of Metal and Materials 17(1978) 483-489.

[2] T. Fujimura, K. Kushida and H. Hongo, Improvement of Refining and Casting Technique for High Grade Wire and Bar Products, Technical Report, Kawasaki Steel, 28(1996) 39-45.

[3] T. Ehara, K. Kurose and T. Fujimura, Mass Production of High Quality I.F. Steel at Mizushima Works, Iron and Steel Society (ISS), 79th steelmaking conf., proc. ISS,PA., (1996) 485-486.

[4] T. Fujimura, H. Yamasaki, K. Ayano and M. Kawaberi, Effect of Electro Magnetic Stirring on the Centerline Segregation of Continuously Cast Steel,70th steelmaking conf.,AIME, (1987) 47.

[5] H. Kitaoka,T. Fujimura,T. Nozaki,H. Habu,S. Kakihara,H. Bada,S. Shiraishi and H. Tanigawa, Semimacroscopic Features of Centerline Segregation in CC Slabs and their Effects on Product Quality ,Tetsu-to-Hagane, 69(1983) A201.

[6] T. Fujimura,E. Takeuchi and J.K. Brimacombe, Segregation Phenomina in the Continuous Casting of Steel Slabs, Japan-Canada Seminar on Secondary Steelmaking, C-5-1-15, December 3-4,1985,Tokyo, Japan,The Iron and Steel Institute of Japan,Tokyo

[7] T. Fujimura and J.K. Brimacombe, Effect of Stirring on Crystal Morphologies and Macro-Segregation, Journal of Material Science Research, 7 (2018) 37-48.

[8] T. Fujimura, S. Takata, T. Matsukawa, H. Mizota and S. Kojima, Internal Quality Improvement of Continuously Cast Blooms by Continuous Forging during Solidification, Iron and Steel Society(ISS),75th Steelmaking cnf., AIME 1992.

[9] S. Kojima, T. Imai, H. Mizota, T. Fujimura and T. Matsukawa, Improvement of Centerline Segregation in Continuously Cast Strand by Continuous Forging Process, Tetsu-to-Hagane 78(1992)1794-1801.

[10] N. Ohashi, Effect on Ftracure Thoghness of Steel, Tetsu-to-Hagane 72 (1986) 747-757.

[11] K. Yamanaka,The Microstrucure and Thoghness of Steels Corresponding to the Chemical Composition of the Segregated Zone of the Plate, Tetsu-to-Hagane 66 (1980) 1367-1373.

[12] T. Kawawa, H. Sato, S. Miyahara, T. Koyano and H. Nemoto, Determination of Solidifying Shell Thickness of Continuously Cast Slab by Rivet Shooting, Tetsu-to-Hagane 60 (1974) 206-216.

[13] J.C. Crepeau, A. Siahpush and B. Spotten, On the Stefan Problem with Volumetric Energy Generation, Heat Mass Transf. 46 (2009) 119–128.

[14] F. Cheung, T. Chawala and D. Penderson, The Effect of Heat Generation and Wall Interaction on Freezing and Melting in a Finite Slab, Int. J. Heat Mass Transfer, 27(1984) 29-37.

[15] J. Stefan, Über die Theorie der Eisbildung, Insbesondere über die Eisbildung im Polarmeere. Sizungsberichte der k.k.Akademie der Wissenschaften in Wien, Mathematisce-Nat-urwissenschaften, Abteilung II,965-983.

[16] T. Kawawa and H. Tuchida, Tekko-no-Gyouko (Solidification of steel), Appendix 4, ed. By Solidification Comm., Joint Sc. on Iron and Steel Basic Research of ISIJ, ISIJ, Tokyo, 1977.

[17] M. Hirai, K. Kanamaru and H. Mori, Tekko-no-Gyouko (Solidification of steel), Appendix 4, ed. By Solidification Comm., Joint Sc. on Iron and Steel Basic Research of ISIJ, ISIJ, Tokyo, 1977.

[18] A. Suzuki, T. Suzuki, Y. Nagaoka, and Y. Iwata, On Secondary Dendrite Arm Spacing in Commercial Steels Having Different Carbon Contents, J. Jpn. Inst. Met. 32 (1968) 1301–1305.

[19] K. Gryc, B. Smetana, M. Zaludova, K. Michalek, P. Klus, M. Tkadleckova, L. Socha, J. Dobrovska, P. Machovcak, L. Valek, R. Pachlopnik and B. Chmiel, Determination of the Solidus and Liquidus Temperatures of the Real-Steel Grades with Dynamic Thermal-Analysis Methods, Mater. Technol. 47 (2013) 569–575.

[20] E.A. Mizikar, Mathematical Heat Transfer Model for Solidification of Continuously Cast Steel Slabs, Trans. AIME 239 (1967) 1747–1753.

[21] J. Szekely and V. Stanek, On Heat Transfer and Liquid Mixing in the Continuous Casting of Steel, Metall. Trans. 1 (1970) 119–126.

[22] J. Matsuno, H. Nakato and H. Ohi, An analysis of Solidification Rate and Surface Temperature of Continuous Casting Slabs, Tetsu-to-Hagane, 60 (1974) 1023–1032.

[23] Y.K. Chaung and K. Schwerdfeger, Experimentelle und Theoretische Untersuchung der Erstarrung einer Eisen-Kohlenstoff-Legierung mit 0.6%C, Arch. Eisenhüttenwes 44 (1973) 341–347.

[24] P.H. Shingu, K. Takeshita, R. Ozaki and T. Akiyama, An analysis of the Solidification of a Binary Eutectic System Considering Temperature and Solute Distribution, J. Jpn. Inst. Met. 42 (1978) 172–179.

[25] H.D. Brody and M.C. Flemings, Solute Redistribution during Dendritic Solidification, Trans. Met. Soc. AIME 236 (1966) 615–624.

[26] T.W. Clyne and W. Kurz, Solute Redistribution during Solidification with Rapid Solid State Diffusion, Met. Trans. 12A (1981) 965–971.

[27] I. Ohnaka, Mathematical Analysis of Solute Redistribution during Solidification with Diffusion in Solid Phase, Trans. ISIJ 26 (1986) 87–96.

[28] V.R. Voller and C. Beckermann, Approximate Models of Microsegergation with Coarsening, Metall. Trans. A 30A (1999) 3016–3019.

[29] Y.M. Won and B.G. Thomas, Simple Model of Microsegregation during Solidification of Steels, Metall. Mate. Trans. A 32A (2001) 1755–1767.

[30] I. Ohnaka and T. Fukusako, Calculation of Solidification of Castings by a Matrix Method, Trans. Iron Steel Inst. Jpn. 17 (1977) 410–418.

[31] K. Kumai, A. Sano, T. Ohashi, E. Nomura and H. Fujii, Study on Solidification Behavior, Solute Segregation and Fluid Flow in Continuously Cast Slab, Tetsu-to-Hagane 7 (1974) 894–914.

[32] S. Asai and I. Muchi, Analysis of Effective Distribution Coefficient Based of Transport Phenomena in Liquid and Solid Region, Tetsu-to-Hagane 64 (1978) 1685–1692.

[33] R.N. Hills, D.E. Looper and P.H. Roberts, A Thermodynamically Consistent Model of a Mushy Zone, Q. J. Mech. Appl. Math. 36 (1983) 505–539.

[34] D.V. Alexandrov, Solidification with a Quasi-Equilibrium Mushy Region: Exact Analytical Solution of Nonlinear Model, J. Crystal Growth 222 (2001) 816–821.

[35] K. Takeshita, An Analysis of the Solidification of a Binary Eutectic System in Consideration of Both Heat and Solute Diffusion, J. Jpn. Inst. Met. 47 (1983) 647–653.

[36] H.E. Huppert and M.G. Worster, Dynamic Solidification of a Binary Melt, Nature 314 (1985) 703–707.

[37] D.V. Alexandrov and V.P. Malygin, Self-Similar Solidification of an Alloy from a Cooled Boundary, Int. J. Heat Mass. Transf. 49 (2006) 763–769.

[38] T. Fujimura and J.K. Brimacombe, Mathematical Analysis of Solidification Behavior of Multicomponent Alloys, Trans. Iron Steel Inst. Jpn. 26 (1986) 532–539.

[39] T. Fujimura, K. Takeshita and R.O. Suzuki, Mathematical Analysis of the Solidification Behavior of Plain Steel Based on Solute- and Heat- Transfer Equations in the Liquid-Solid zone, Metall. Mate. Trans. B 49 (2018) 644–657.

[40] T. Fujimura, K. Takeshita and R.O. Suzuki, Mathematical Analysis of the Solidification Behavior of Multi-Component Steel Based on Solute- and Heat- Transfer Equations in the Liquid-Solid Zone, accepted for publication to International Journal of Heat and Mass Transfer, 130 (2019) 797-812.

[41] H.S. Carslaw and J.G. Jaeger, Conduction of Heat in Solids, 2nd ed., Oxford University Press, New York, Tronto, Tokyo, 1959, 283–291.

[42] G. Shin, T. Kajitani, T. Suzuki and T. Umeda, Mechanical Properties of Carbon Steels during Solidification, Tetsu-to-Hagane 78 (1992) 587–593.

Chapter 2 Model I

Mathematical Analysis of Solidification Behavior in Multicomponent Alloy Steel

Abstract

A mathematical model of dendrite solidification in multi-component alloys has been developed to predict microsegregation and to obtain a better understanding of the relation between the solid fraction and temperature in the solid/liquid zone. An analytical solution to the solute- and heat-balance equations in the model has been obtained by assuming that equilibrium exists at the solid/liquid interface and that the solidus and liquidus grow in proportion to the square root of time.

Effective partition ratios predicted by the model for the continuous casting of steel are in good agreement with generally accepted values. Model predictions of temperature distribution in the mushy zone fit well with measured temperatures. However predictions of micro-segregation of Cr and Ni in a unidirectionally solidified stainless steel were less satisfactory, presumably because the model neglects segregation between adjacent secondary dendrite arms. The model also has provided a theoretical basis for the relationship between temperature and solid fraction in the mushy zone. It is possible to assume a linear relationship between temperature and solid fraction in cases, general steel, where one of the solutes has a dominant effect on depression of the liquidus temperature with respect to its concentration. This assumption simplifies the computation of solidification behavior without introducing severe errors.

[Note] Model I adopts the Dirichlet conditions with the measured solidification constants as the boundary conditions.

2.1 Introduction

Prediction of solidification phenomena in the mushy zone of a casting process is important for the determination of solute concentration distributions and of the solidification profile. But the problem, from a theoretical standpoint, is difficult because solute transport and heat flow within the mushy zone are coupled: variation of the solid fraction within the mushy zone influences both inter-dendritic solute segregation and latent-heat evolution. Thus mathematical equations describing heat and mass transport must be solved simultaneously.

Recently mathematical models have been formulated in which both heat conduction and diffusion in the mushy zone have been taken into account. Asai et al. [1] have considered a binary alloy system in which heat and

mass transfer proceed under, quasi-steady state conditions. A constant solidification rate was assumed and an analytical solution to the transport equations was achieved. The assumption of constant solidification rate poses problems, however, because in general, with the exception of the initial and final stages of solidification, the position of the solidus and liquidus positions vary linearly with the square root of time. In another study, Takeshita [2] has developed a numerical solution for a similar model of a binary eutectic system. Tacke et al. [3] also have employed a numerical solution to solve the simultaneous transport equations applied to a multicomponent alloy.

In the present study, an analytical solution is sought to the heat- and mass- transfer equations applied to the solidus and liquidus positions depend on the square root of time. The validity of the solution also is checked against reported measurements.

2.2 Mathematical Model

2.2.1 Solidification Problems

The solidification problem being mathematically modelled is shown schematically in Fig.2.1. Heat is extracted unidirectionally and a solid shell grows from the cooled surface. In the mushy zone heat flows by conduction and solutes are transferred solely by diffusion. From the mathematical point of view, the equations describing these process in the mushy zone should be solved simultaneously for the liquid and solid phases in the mushy zone subjected to boundary conditions at moving solidus and liquidus boundaries, and initial conditions. The problem can be simplified, however, if the boundary values (temperature and solute concentration) at the solidus and liquidus positions are assumed to be constant. The same assumption has been made previously by Asai et al. [1] and Takeshita [2].

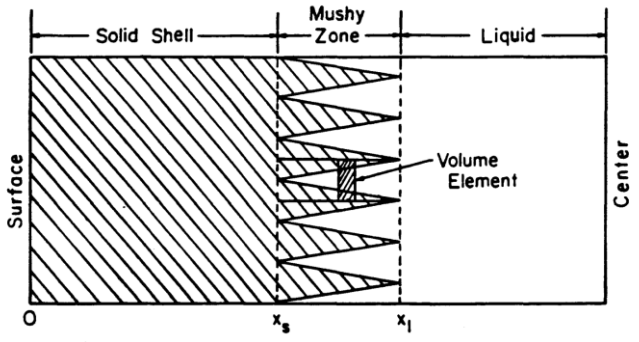

Fig. 2.1 Schematic diagram of the solidification problem under study.

2.2.2 Assumptions

The principal assumptions made in the model formulation are as follows:

(1) The density and specific heat of the liquid are the same as in the solid.

(2) Liquid and solid are in equilibrium at the solid-liquid interface.

(3) Heat is extracted only by heat conduction along the x axis.

(4) Solutes are transported only by diffusion subject to moderate fluid flow in the mushy zone.

(5) The dependence of the equilibrium partition ratios and the diffusion coefficients on solute concentration is negligible.

(6) The effect of the dendrite tip curvature on liquidus temperature is negligible.

(7) Undercooling within the mushy zone is negligible.

(8) Diffusion of solutes in the liquid is sufficiently rapid to yield a homogeneous composition in the direction normal to that of heat extraction over distances of the order of the dendrite arm spacing.

(9) The solidus and liquidus move according to the square root of time.

(10) The heat and solute transport are in steady state relative to a normalized coordinate system which moves with the solidus point.

2.2.3 Mathematical Formulation

The volume element considered is shown in Fig. 2.l. The variation of the solute concentration within the volume element of component *i* with respect to time is given by

$$\frac{\partial \overline{C_i}}{\partial t} = \frac{\partial (f\, C_i + f_s \overline{C_{si}})}{\partial t} = \frac{\partial (f C_i)}{\partial t} + C_{si} \frac{\partial f_s}{\partial t} + \alpha_i f_s \frac{\partial C_{si}}{\partial t} \tag{2.1}$$

where α_i represents the extent of diffusion of the solute *i* in the solid(*i.e.,* α_i =0 when diffusion of component *i* in the solid is negligible and α_i = 1 when diffusion in the solid is rapid enough to result in an homogeneous composition over distances of the order of the dendrite arm spacing).

C_{si} and f_s are related to C_i and f by the following equations.

$$C_{si} = \mathrm{k}_i C_i \tag{2.2}$$

$$f_s = 1 - f \tag{2.3}$$

The solute flux of component *i* due to diffusion in a multicomponent alloy within the volume element is

$$J_i = -\sum_j f\, E_{ij} \frac{\partial C_j}{\partial x} - \sum_j \alpha_j f_s \mathrm{D}_{ij} \frac{\partial C_{sj}}{\partial x} \tag{2.4}$$

Then a mass balance on component *i,* based on Eqs. (2.l) to (2.4) yields the following

$$\begin{aligned}(1-\alpha_i \mathrm{k}_i) f \frac{\partial C_i}{\partial t} + (1-\mathrm{k}_i) C_i \frac{\partial f}{\partial t} + \alpha_i \mathrm{k}_i \frac{\partial C_i}{\partial t} \\ = \sum_j (E_{ij} - \alpha_j \mathrm{k}_j D_{ij}) \frac{\partial}{\partial x}\left(f \frac{\partial C_j}{\partial x}\right) + \sum_j \alpha_j \mathrm{k}_j \mathrm{D}_{ij} \frac{\partial^2 C_j}{\partial x^2}\end{aligned} \tag{2.5}$$

A heat balance gives

$$\rho_2 \mathrm{Cp}_2 \frac{\partial T}{\partial t} + \rho_2 L \frac{\partial f}{\partial t} = \mathrm{K}_2 \frac{\partial^2 T}{\partial x^2} \tag{2.6}$$

It is reasonable to assume that the inter-dendritic liquid is in chemical equilibrium with the solid at the solid/liquid interface. Hence, its composition is coupled with temperature by the liquidus Surface of the phase diagram which can be represented by

$$T = T_{\mathrm{M}} + \sum_i \mathrm{m}_i C_i \tag{2.7}$$

Substituting Eq.(2.7) into Eq.(2.6) yields

$$\rho C_p \sum_i m_i \frac{\partial C_i}{\partial t} = K \sum_i m_i \frac{\partial^2 C_i}{\partial x^2} - L\rho \frac{\partial f}{\partial t} \tag{2.8}$$

The boundary conditions for Eq.(2.8) can be characterized as follows:

$$x = x_l \ : \ C_i = C_i^{\circ} \ , \ f = 1 \tag{2.9}$$

$$x = x_s \ : \ C_i = C_i^{*} \ , \ f = 0 \tag{2.10}$$

Next it is assumed that

$$f = \lambda_i C_i + s_i = \lambda_j C_j + s_j \tag{2.11}$$

which is in fact one of the solutions to the simultaneous equations.

Then, the concentration of *i* is related to that of *j* in the liquid by

$$C_j = \frac{\lambda_i}{\lambda_j} C_i + \frac{s_i - s_j}{\lambda_i} \tag{2.12}$$

Moreover, as has been stated earlier, the solidus point and the liquidus point are assumed to be related to time by the following equations

$$x_l = \nu_l \sqrt{t} - d \tag{2.13}$$

$$x_s = \nu_s \sqrt{t} - d \tag{2.14}$$

The normalized coordinate X moving with the solidus point is related to the original coordinate x fixed in space by

$$X = \frac{x - x_s}{x_l - x_s} = \frac{x' - \nu_s \sqrt{t}}{(\nu_l - \nu_s)\sqrt{t}} \tag{2.15}$$

where x' is

$$x' = x + d \tag{2.16}$$

Equations (2.5) and (2.8) have been transformed according to Eq.(2.15) and Eq.(2.l6) and unsteady terms have been neglected (Applying the Neumann-type solution gives the same results). Equations (2.11) and (2.12) have been substituted into the resulting equations which then have been rearranged to give

$$\frac{\mathrm{d}^2 C_i}{\mathrm{d}x^2} = a(\mathrm{A}+\mathrm{B}_i\lambda_i)(X+b)\frac{\mathrm{d}C_i}{\mathrm{d}X} \tag{2.17}$$

$$(X+b)\,f\,\frac{\mathrm{d}C_i}{\mathrm{d}X} + \mathrm{W}_i(X+b)C_i\frac{\mathrm{d}f}{\mathrm{d}X} + \mathrm{Q}_i(X+b)\frac{\mathrm{d}C_i}{\mathrm{d}X} + \mathrm{M}_i\frac{\mathrm{d}}{\mathrm{d}X}\left(f\frac{\mathrm{d}C_i}{\mathrm{d}X}\right) + \mathrm{P}_i\frac{\mathrm{d}^2 C_i}{\mathrm{d}X^2} = 0 \tag{2.18}$$

where

$$a = (\nu_l - \nu_s)^2 / 2 \tag{2.19}$$

$$b = \nu_l / (\nu_l - \nu_s) \tag{2.20}$$

$$\mathrm{W}_i = (1-k_i)/(1-\alpha_i k_i) \tag{2.21}$$

$$\mathrm{Q}_i = \alpha_i k_i / (1-\alpha_i k_i) \tag{2.22}$$

$$\mathrm{P}_i = (\sum_j \alpha_j k_j D_{ij}\lambda_i/\lambda_j)/a(1-\alpha_i k_i) \tag{2.23}$$

$$\mathrm{M}_i = \sum_j (E_{ij} - \alpha_j k_j D_{ij})\lambda_i/\lambda_j/a(1-\alpha_i k_i) \tag{2.24}$$

$$\mathrm{A} = -\rho C_p / K \tag{2.25}$$

$$\mathrm{B} = -\frac{\rho L}{K\sum_j m_j \lambda_i/\lambda_j} \tag{2.26}$$

The boundary conditions are rewritten by substituting Eq.(2.11) to yield the following.

$$X = 1 \;:\; 1 = \lambda_i C_i^{\circ} + s_i \tag{2.27}$$

$$X = 0 \;:\; 0 = \lambda_i C_i^{*} + s_i \tag{2.28}$$

Hence, C_i^* is

$$C_i^* = C_i^{\circ} - 1/\lambda_i \tag{2.29}$$

Integrating Eq.(2.17) twice from X = 0 to X = 1 and applying the approximation

$$\mathrm{erf}(\xi_i) \approx 1 - \frac{\exp(-\xi_i^2)}{\sqrt{\pi}\xi_i} \tag{2.30}$$

where

$$\xi_i = \sqrt{-\frac{(\mathrm{A}+\mathrm{B}_i\lambda_i)}{2}}(X+b) \tag{2.31}$$

gives

$$C_i = \frac{\gamma_i \exp\left\{\dfrac{a(\mathrm{A}+\mathrm{B}_i\lambda_i)}{2}\cdot(X+b)^2\right\}}{a(\mathrm{A}+\mathrm{B}_i\lambda_i)(X+b)} + C_i^* - \frac{\gamma_i \exp\left\{\dfrac{a(\mathrm{A}+\mathrm{B}_i\lambda_i)}{2}\cdot b^2\right\}}{a(\mathrm{A}+\mathrm{B}_i\lambda_i)b} \tag{2.32}$$

The error for this approximation is less than 0.05% when ξ_i>2.

Substituting Eq.(2.11) and Eq.(2.17) into Eq.(2.18) yields

$$C_i = \frac{\gamma_i \exp\left\{\dfrac{a(\mathrm{A}+\mathrm{B}_i\lambda_i)}{2}\cdot(X+b)^2\right\}}{F_i(X+b)} - \frac{G_i}{F_i} \tag{2.33}$$

where F_i and G_i are

$$F_i = -\frac{(1+W_i)+M_i a(\mathrm{A}+\mathrm{B}_i\lambda_i)}{M_i} \tag{2.34}$$

$$G_i = -\frac{s_i+Q_i+(s_iM_i+P_i)a(\mathrm{A}+\mathrm{B}_i\lambda_i)}{M_i\lambda_i} \tag{2.35}$$

Comparing Eq.(2.32) and Eq.(2.33) and substituting Eq.(2.21) to Eq.(2.24), one obtains

$$\lambda_i = -\frac{(1+W_i)(1-\alpha_i k_i)}{2\mathrm{B}_i\sum_j (E_{ij}-\alpha_j k_j D_{ij})\dfrac{\lambda_i}{\lambda_j}} - \frac{\mathrm{A}}{\mathrm{B}_i} \tag{2.36}$$

$$\gamma_i = \frac{2bF_i}{(1+W_i)\exp(\dfrac{F_i}{2}b^2)}\cdot\left[W_iC_i^* + \frac{1}{\lambda_i}\left\{\frac{\alpha_i k_i}{1-\alpha_i k_i} - \frac{(1+W_i)\sum_j \alpha_i k_i D_{ij}\dfrac{\lambda_i}{\lambda_j}}{2\sum_j (E_{ij}-\alpha_i k_i D_{ij})\dfrac{\lambda_i}{\lambda_j}}\right\}\right] \tag{2.37}$$

Consequently, C_i and f are given as follows;

$$C_i = \eta_i\left[\frac{b\exp\left\{\dfrac{F_i}{2}X(X+2b)\right\}}{(X+b)} - 1\right] + C_i^* \tag{2.38}$$

$$\eta_i = \frac{2}{(1+W_i)}\left[W_iC_i^* + \frac{1}{\lambda_i}\left\{\frac{\alpha_i k_i}{1-\alpha_i k_i} - \frac{(1-W_i)\sum_j \alpha_j k_j D_{ij}\dfrac{\lambda_i}{\lambda_j}}{2\sum_j (E_{ij}-\alpha_j k_j D_{ij})\dfrac{\lambda_i}{\lambda_j}}\right\}\right] \tag{2.39}$$

$$C_i^* = C_i^\circ - 1/\lambda_i \tag{2.40}$$

$$f = \lambda_i(C_i - C_i^\circ) + 1 \tag{2.41}$$

$$F_i = a(\mathrm{A}+\mathrm{B}_i\lambda_i) \tag{2.42}$$

$$\lambda_i\eta_i = \lambda_j\eta_j \tag{2.43}$$

For the case where diffusion in the solid is rapid, the effective partition ratio for component *i*, defined as the ratio of the average solute concentration in the solid to the solute concentration in the bulk liquid, is

$$\begin{aligned}\alpha_i = 1 \ : \quad k_i^{\mathrm{ef}} &= k_i C_i^* / C_i^\circ \\ &= k_i(1-1/\lambda_i C_i^\circ)\end{aligned} \tag{2.44}$$

For the other case,

$$\begin{aligned}\alpha_i = 0 \ : \quad k_i^{\mathrm{ef}} &= \int_0^1 C_{si} / C_i^\circ \, \mathrm{d}f_s \\ &= k_i(1-1/2\lambda_i C_i^\circ)\end{aligned} \tag{2.45}$$

2.3 Model Predictions and Discussion

2.3.1 Physical Properties

The physical properties used in the calculations are listed in Table 2.1.

Selection of the values for thermal conductivity in the mushy zone warrants discussion because measurements have not been made under conditions corresponding to in this solid/liquid region, particularly with respect to fluid flow. Thermally driven flow adjacent to the solidification front can give rise to estimated velocities of 0.1 to 1 cm/s [5,6] while solidification shrinkage may generate a fluid velocity of about 0.01 cm/s [7-9]. Consequently, the thermal conductivity in the mushy zone could be larger than that measured in a stagnant liquid. However, the difference is not expected to be great because heat flow by conduction is large compared to that by convection at the low fluid velocities estimated in the inter-dendritic region. Moreover, a significant fraction of the mushy zone consists of fixed solid dendrites unaffected by fluid flow. Thus a thermal conductivity measured under stagnant conditions has been used for the mushy zone, Table 2.1.

The same argument does not hold when considering inter-diffusion coefficients in the inter-dendritic liquid because the rate of solute transport by diffusion is low relative to that by convection. Hence inter-diffusion coefficients measured in a stagnant liquid cannot be adopted for the inter-dendritic region. However, if the thermal conductivity and solidification constants, ν_l and ν_s, are known, the inter-diffusion coefficients, as well as other constants involved in the model, can be determined. This is the approach taken in this study; hence the estimated inter-diffusion coefficients include the influence of fluid flow and should be larger than values obtained under stagnant conditions. The problem of characterizing the solidification constants remains but is taken up in a later section.

Questions also arise concerning the determination of liquidus and solidus temperatures in the presence of microsegregation. With respect to liquidus temperature, the problem is not serious because microsegregation at the dendrite tips is so small that super-cooling is only a few degrees [10]. Therefore, it is reasonable to estimate the liquidus temperature from the phase diagram [11,12] or from measurements [13] which are in reasonable agreement. Such is not the case with the solidus temperature. Discrepancies exist between estimates of solidus temperature based on the phase diagram and models accounting for microsegregation. Consequently, the solidus temperature has been taken from measurements employing the "shooting bullet" technique [15]. It may be noted that any other temperature could be used in place of the solidus temperature provided that its location is known.

Table 2.1 Nomenclature and physical properties used in the present model.

Property		Value
L	Heat of fusion	276 kJ/kg [16]
ρ	Density	7.5×10^3 kg/m [17]
C_p	Specific heat	0.77 kJ/kgK [18]
K	Thermal conductivity	31.8 W/mK [18]
k_C	Partition ratio of C in δ-Fe	0.235 [19,20]
	Partition ratio of C in γ-Fe	0.36 [21]
k_{Mn}	Partition ratio of Mn in δ-Fe	0.73 [22]
k_{Si}	Partition ratio of Si in δ-Fe	0.77 [23]
k_{Cr}	Partition ratio of Cr in γ-Fe	0.86 [21,24]
k_{Ni}	Partition ratio of Ni in γ-Fe	0.89 [21,24]
T°	General steel	$T^\circ = T_M - 78*(\%C) - 4.9*(\%\mathrm{Mn}) - 7.6*(\%\mathrm{Si})$ [11]
	Stainless steel	$T^\circ = T_M - 83.9*(\%\mathrm{C}) - 5.1*(\%\mathrm{Ni}) - 1.5*(\%\mathrm{Cr})$ [25]
α_C	Parameter	1
$\alpha_{Mn}, \alpha_{Si}, \alpha_{Cr}, \alpha_{Ni}$	Parameter	0

2.3.2 Comparison of Model Predictions with Reported Measurements

The effective partition ratios and apparent inter-diffusion coefficients first have been predicted by the model for the continuous casting of steel. The dependence of the positions of the liquidus and solidus temperatures

on time (t=0 at the meniscus) is shown in Fig. 2.2. As mentioned earlier, the shooting bullet technique was employed to obtain this data [15]. The two solid lines in Fig. 2.2 have been fit to the data by Asai et al. [15]. It is clear that the liquidus and solidus positions depend on the square root of time; the solidification constants, ν_s and ν_l were determined from Fig.2.2 for the steel which is effectively an Fe-C-Mn-Si quaternary alloy. The apparent inter-diffusion coefficients (see Appendix) and effective partition ratios have been predicted with the model using this data and the results are presented in Tables 2.2 and 2.3 and Fig. 2.3. It is difficult to make a direct comparison of the estimated partition ratios to measured results because they have not been determined for this steel. Generally, however, $k_{\mathrm{C}}^{\mathrm{ef}}$, $k_{\mathrm{Si}}^{\mathrm{ef}}$ and $k_{\mathrm{Mn}}^{\mathrm{ef}}$ are in the range of 0.9 to 1.1 in continuously cast steel [26] except in the chill and center regions. Hence the estimates of effective partition ratios in Table 2.2 appear sound. It should be noted that the approximation employed in formulating the model, given by Eq.(2.30), is reasonable since the minimum value of ξ (=2.9) is sufficiently large.

The estimated carbon diffusivity, parameter M_{C}, 5.58 $\times 10^{-7}$ m^2/s, was in good agreement with the carbon inter-diffusion coefficient estimated by Asai et al. [19] (4.7 $\times$ 10^{-7} m^2/s) for a Fe-0.15%C-0.70%Mn-0.22% Si continuously cast steel. Although these values are somewhat larger than that measured by Grace et al. [27] (2–4 $\times$ 10^{-7} m^2/s) under stagnant conditions, these are reasonable as discussed earlier.

Table 2.2 Estimations of model parameters based on the shot bullet measurements [15] of the liquidus and solidus positions in the continuously cast steel (Steel composition: 0.15%C, 0.70%Mn, 0.22%Si, 0.017%P, 0.019%S : $\xi = 2.91 \sim 3.397$)

	$\lambda(\%^{-1})$	k^{ef}	Estimated inter-diffusion coefficients in the inter-dendritic liquid $(\times 10^{-7}\ \mathrm{m}^2/\mathrm{s})$
C	-2.33	0.91	$E_{\mathrm{CC}} + 1.12E_{\mathrm{CMn}} + 0.29E_{\mathrm{CSi}} = 3.98$
Mn	-2.07	0.98	$E_{\mathrm{MnMn}} + 0.89E_{\mathrm{MnC}} + 0.26E_{\mathrm{MnSi}} = 3.30$
Si	-8.12	0.99	$E_{\mathrm{SiSi}} + 3.49E_{\mathrm{SiC}} + 3.92E_{\mathrm{CMn}} = 3.20$

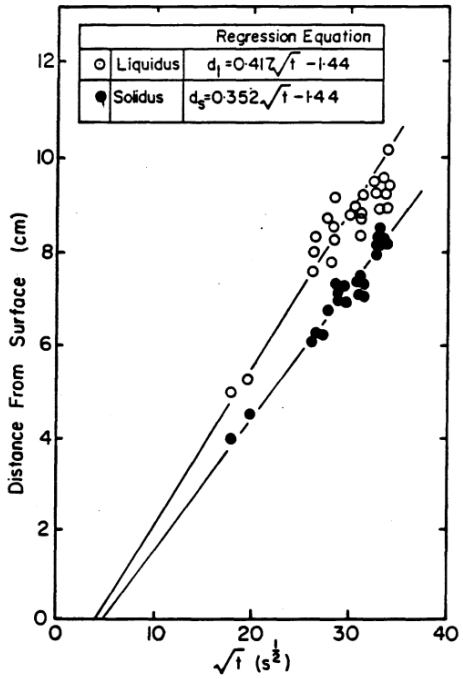

Fig. 2.2 Square-root time dependence of position liquidus and solidus temperatures in a continuously cast slab as measured by the shooting bullet technique[15].

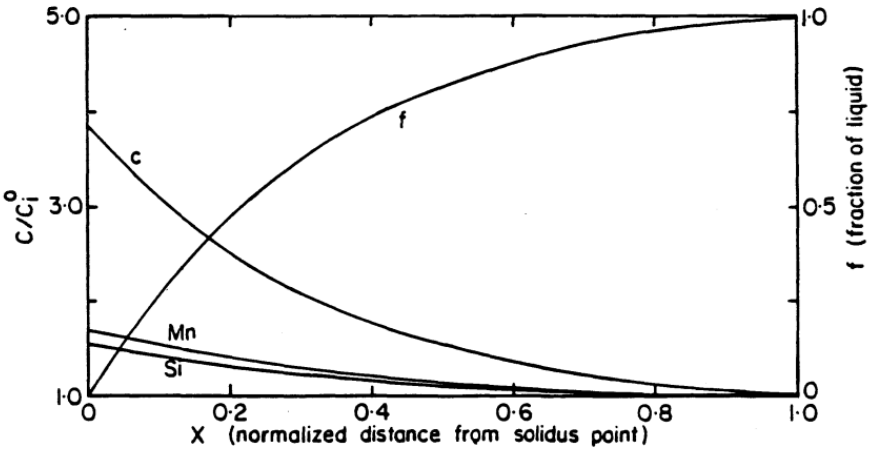

Fig. 2.3 Distribution of solute concentration in the liquid and of fraction liquid in the mushy zone.

Next the model was evaluated using measurements by Mori et al. [28] of temperature in the mushy zone of a 240-mm square bloom; again the shooting bullet technique had been applied in the experiments. The measured temperatures at different locations relative to the liquidus position are shown in Fig. 2.4. In this case the solidification constant, ν_s was not measured but ν_l was reported to be 0.42 $cm s^{-1/2}$. This value was adapted and the unknown parameters including ν_s were adjusted to fit model predictions of the temperature

distribution in the mushy zone to the measurements within ± 2°C. The resulting estimates of effective partition ratios and apparent inter-diffusion coefficients are given in Table 2.3 and seen to be in relative agreement with the values derived from the other case, Table 2.2. Also, as before, the minimum value of a (ξ = 2.45) is large enough to justify the approximation given by Eq.(30). In Fig. 2.4 the fitted temperature distribution in the mushy zone is observed to closely match the measurements of Mori et al. [28].

Table 2.3 Estimations of model parameters based on the shot bullet measurements [28] of the continuously cast steel (Steel composition: 0.2%C, 1.33%Mn, 0.36%Si, 0.029%P, 0.038%S : ξ = 2.45 ~ 3.10)

	$\lambda(\%^{-1})$	k^{ef}	Estimated inter-diffusion coefficients in the inter-dendritic liquid ($\times 10^{-7}$ m^2 / s)
C	-1.65	0.95	$E_{CC} + 1.56E_{CMn} + 0.34E_{CSi} = 5.58$
Mn	-1.06	0.99	$E_{MnMn} + 0.64E_{MnC} + 0.22E_{MnSi} = 4.63$
Si	-4.82	0.99	$E_{SiSi} + 2.92E_{SiC} + 4.56E_{CMn} = 4.48$

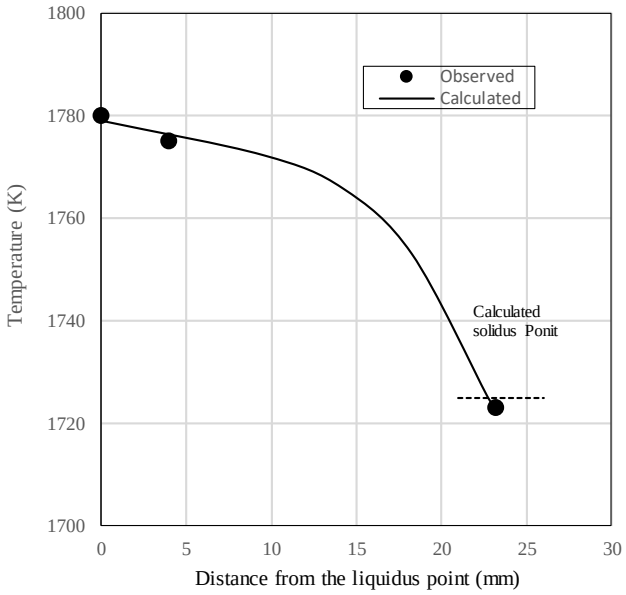

Fig. 2.4 Temperature distribution in the mushy zone of a continuously cast 240-mm square bloom.

Finally, the model has been evaluated for the case of stainless steel that contains a considerable concentration of alloy components. Sugiyama et al. [29] and Umeda et al. [30] have investigated micro-segregation in unidirectionally solidified 25 Cr - 20 Ni austenitic stainless steel. In order to obtain ν_s and ν_l, their

temperature measurements at different distances from the chill face have been rearranged as shown in Fig. 2.5. The liquidus temperature of this steel has been estimated to be 1666K (1393°C) and the solidus, temperature is expected to be between 1603K(1330°C) [29] and 1658K(1385°C) [31]. Since the estimate of the solidus temperature is not reliable, a value of ν_s cannot be obtained directly from Fig. 2.5. However, the unknown constants, λ_C, λ_{Ni} and λ_{Cr} can be fixed by using the maximum observed concentrations of Ni and Cr rather than by specifying ν_s. In this study, C_{Ni}^{max}=26.8% and C_{Cr}^{max}=19.8% have been adopted and all unknown constants have been fitted. The minimum value of ξ is 2.92. The solidus temperature, with respect to the maximum concentrations C_{Ni}^{max} and C_{Cr}^{max} adopted, was estimated to be 1635K(1362°C) (A different solidus temperature is obtained depending on the values chosen for C_{Ni}^{max} and C_{Cr}^{max} ,e.g. 1629K(1356°C) for C_{Ni}^{max} =27.8% and C_{Cr}^{max}=20.4%, but the difference is not large). This is within the range where isotherm position is proportional to the square root of time, Fig. 2.5.

Figure 6 shows the measured [29] and estimated micro-segregation of Ni and Cr in the stainless steel. It should be noted that Sugiyama et a1. [29] defined the fraction of solid as the area ratio of each iso-concentration contour in the transverse section of the primary dendrites; this corresponds to the definition of f_s adopted in the present model. Micro-segregation of Cr was measured by Sugiyama et al. [29] in two sections: one on the axis of the secondary dendrite arm and the other intermediate between two secondary dendrite arms. In both sections the Cr concentration - fraction solid plots exhibit more pronounced curvature than the model-prediction. With respect to Ni micro-segregation the difference between the measurements and model predictions is even greater. This difference is likely due, at least in part, to micro-segregation between adjacent secondary dendrite arms which is not considered in the present model. Unfortunately, the location. of the measured section relative to secondary dendrite arms has not been reported for the Ni micro-segregation. For both Cr and Ni, the model predictions of minimum and maximum concentrations at fs = 0 and 1 respectively are in good agreement with measurements.

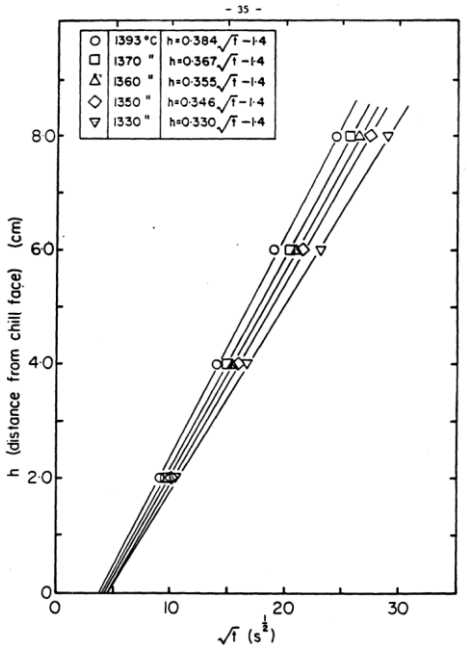

Fig. 2.5 Variation of isotherm locations with the square root of time during the unidirectional solidification of 25%Cr-20%Ni stainless steel (based on temperature measurements of Sugiyama et al. [29]).

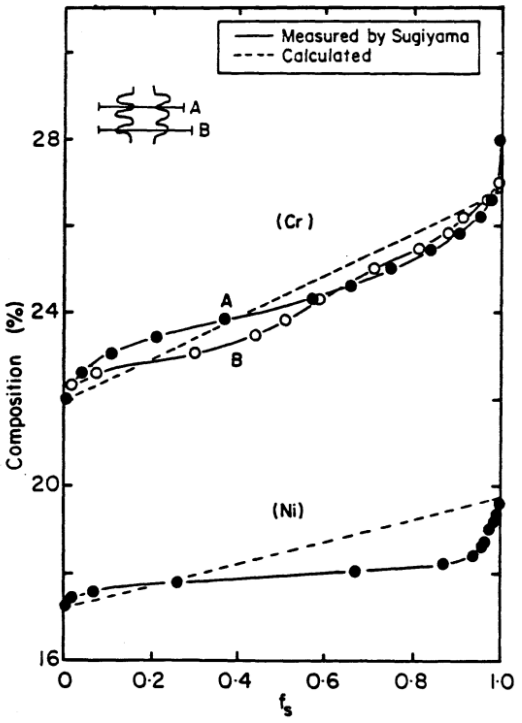

Fig. 2.6 Measured [29] and calculated Cr and Ni compositions as a function of fraction solid in stainless steel(0.08%C,25.6%Cr,19.1%Ni). (A: Section between neighboring secondary dendrite arms. B: Section close to the axis of the secondary dendrite arm.)

2.3.3 Relationship between Temperature and Fraction Liquid in the Mushy Zone

The linear relationship between solute concentration and the fraction liquid, denoted by Eq.(2.41), deserves further comment particularly with respect to steel in which the predominant alloying component is carbon.

Considering that $m_c >> m_{\mathrm{Mn}}, m_{\mathrm{Si}}$, Eq.(2.7) can be simplified as follows

$$T \simeq T_{\mathrm{M}} + m_{\mathrm{C}} C_{\mathrm{C}} \tag{2.46}$$

Then substituting Eqs.(2.40) and (2.46) into Eq.(2.4l) yields

$$f \simeq \frac{T - T^*}{T^\circ - T^*} \tag{2.47}$$

that is, the fraction liquid increases linearly with temperature between the liquidus and solidus temperatures. In earlier studies [16,31], Eq.(2.47) has been adopted for solidification calculations without a firm theoretical basis. The present model provides the fundamental basis for this conventional assumption.

2.4 Conclusion of this Chapter

A mathematical model of dendrite solidification in which the liquidus and solidus points move in proportion to the square root of time has been formulated and an analytical solution has been sought. The applicability of the model has been examined by comparing model predictions to measurements reported from several solidification studies. For the continuous casting of steel, reasonable agreement between predictions and measurements was obtained for the effective partition ratios of C, Mn and Si. Also the estimated temperature in the mushy zone could be fit closely to reported values. For a unidirectionally solidified austenitic stainless steel, model predictions of Cr and Ni concentration as a function of fraction solid were less satisfactory, presumable because the micro-segregation between the neighboring secondary dendrite arms was neglected in the model.

Finally, the model provides a theoretical basis for the conventional assumption of the linear relationship between temperature and fraction liquid in the mushy zone.

NOMENCLATURE

$\overline{C}_i$: Average concentration of component *i* in volume element.
C_i : Concentration of component *i* in inter-dendritic liquid.
C_{si} : Concentration of component *i* in solid.
C_i° : Concentration of component *i* at the liquidus point.
C_i^{*} : Concentration of component *i* at the solidus point.
f : Fraction of liquid.
f_s : Fraction of solid.
J_i : Diffusion flux of component *i* in volume element.
E_{ij} : Interdiffusion coefficient in inter-dendritic liquid.
D_{ij} : Interdiffusion coefficient in solid.
α_i : parameter describing the extent of diffusion of component *i* in solid.
k_i : partition ratio of component *i.*
k_i^{ef} : effective partition ratio of component *i*.
K : Thermal conductivity.
ρ : Density.
C_p : Specific heat.
L : Heat of fusion.
m_i : Slope of liquidus temperature with respect to the concentration of component *i.*
x : Distance
X : Normalized distance from the solidus point.
λ_i : Arbitrary constant.
ν_s : Solidification constant for solidus point.
ν_l : Solidification constant for liquidus point.
γ_i : Arbitrary constant defined in Eq.(2.36).
ξ_i : Parameter corresponding to the distance from the solidus point.
d : Arbitrary constant.
t : Time
T_{M} : Melting temperature of pure metal.
T° : Liquidus temperature.
T^{*} : Solidus temperature.

Appendix

Estimation of the unknown parameters

When $X=1,\ C_{\mathrm{C}}=C_{\mathrm{C}}^{\circ}$ and from Eqs.(2.38) and (2.4), one obtains the following:

$$1=\lambda_{\mathrm{C}}\eta_{\mathrm{C}}\left[\frac{b\exp\left\{\frac{F_{\mathrm{C}}}{2}(1+2b)\right\}}{(1+b)}-1\right] \tag{2.A1}$$

Where F_{C} is given by Eq.(25), (26) and (27) as follows:

$$F_{\mathrm{C}}=-\frac{a\rho C_{\mathrm{p}}}{K}-\frac{a\rho L}{K\left(\frac{m_{\mathrm{C}}}{\lambda_{\mathrm{C}}}+\frac{m_{\mathrm{Mn}}}{\lambda_{\mathrm{Mn}}}+\frac{m_{\mathrm{Si}}}{\lambda_{\mathrm{Si}}}\right)} \tag{2.A2}$$

Eq.(2.39) can be simplified by neglecting D_{ij} ,which is much smaller than E_{ij} as follows:

$$\eta_{\mathrm{C}}=\frac{2}{(1+W_{\mathrm{C}})}\left\{W_{\mathrm{C}}\left(C_{\mathrm{C}}^{\circ}-\frac{1}{\lambda_{\mathrm{C}}}\right)+\frac{\alpha_{\mathrm{C}}k_{\mathrm{C}}}{\lambda_{\mathrm{C}}(1-\alpha_{\mathrm{C}}k_{\mathrm{C}})}\right\} \tag{2.A3}$$

$$\eta_{\mathrm{Mn}}=\frac{2}{(1+W_{\mathrm{Mn}})}\left\{W_{\mathrm{Mn}}\left(C_{\mathrm{Mn}}^{\circ}-\frac{1}{\lambda_{\mathrm{Mn}}}\right)+\frac{\alpha_{\mathrm{Mn}}k_{\mathrm{Mn}}}{\lambda_{\mathrm{Mn}}(1-\alpha_{\mathrm{Mn}}k_{\mathrm{Mn}})}\right\} \tag{2.A4}$$

$$\eta_{\mathrm{Si}}=\frac{2}{(1+W_{\mathrm{Si}})}\left\{W_{\mathrm{Si}}\left(C_{\mathrm{Si}}^{\circ}-\frac{1}{\lambda_{\mathrm{Si}}}\right)+\frac{\alpha_{\mathrm{Si}}k_{\mathrm{Si}}}{\lambda_{\mathrm{Si}}(1-\alpha_{\mathrm{Si}}k_{\mathrm{Si}})}\right\} \tag{2.A5}$$

where $W_{\mathrm{C}}, W_{\mathrm{Mn}} and\ W_{\mathrm{Si}}$ are given by Eq.(2.22) as follows:

$$W_{\mathrm{C}}=\frac{1-k_{\mathrm{C}}}{1-\alpha_{\mathrm{C}}k_{\mathrm{C}}} \tag{2.A6}$$

$$W_{\mathrm{Mn}}=\frac{1-k_{\mathrm{Mn}}}{1-\alpha_{\mathrm{Mn}}k_{\mathrm{Mn}}} \tag{2.A7}$$

$$W_{\mathrm{Si}}=\frac{1-k_{\mathrm{Si}}}{1-\alpha_{\mathrm{Si}}k_{\mathrm{Si}}} \tag{2.A8}$$

Substituting Eq.(2.A3) to (2.A5) into Eq.(2.43) yields λ_{Mn} and λ_{Si} with λ_{C} ,considering $\alpha_{\mathrm{C}}=1,\ \alpha_{\mathrm{Mn}}=\alpha_{\mathrm{Si}}=0$. Thus, then Eq.(2.A1) is solved with respect to λ_{C} by combining Eq.(2.A2) and (2.A3). Substituting this solution into Eq.(2.36) yields E_{ij}.

References

[1] S. Asai and I. Muchi, Analysis of Effective Distribution Coefficient Based of Transport Phenomena in Liquid and Solid Region, Tetsu-to-Hagane 64 (1978) 1685–1692

[2] K. Takeshita, An Analysis of the Solidification of a Binary Eutectic System in Consideration of Both Heat and Solute Diffusion, J. Jpn. Inst. Met. 47 (1983) 647–653.

[3] K. Tacke, A. Grill, K. Miyazawa and K. Schweldtfeger, Macro Segregation in Strand Cast: Computation of Concentration Profile with a Different Model, Arch Eisenhüttenwes., 52 (1981) Nr. 1, Jan. 15.

[4] I. Muchi, M. Takatsu, E. Sada and A. Moriyama, Yakin-Jitsuyo-Sugaku, Kagaku-Gijutsu-Sha, Maruzen, Tokyo, (1975), p.156.

[5] J. Szekely and V. Stanek, On Heat Transfer and Liquid Mixing in the Continuous Casting of Steel, Metall. Trans. 1 (1970) 119–126.

[6] T. Mitsuo, T. Horigome, S. Saito, E. Nomura, Y. Kitamuta and R.Kono, On the Accumulation Mechanism and Reducing Process of Large Non-Metalic Inclusions in the Bottom Equiaxed Zone of Ingots, Tetsu-to-Hagane, 57 (1971) 915-941

[7] M. C. Flemings and G. E. Nero, Macro Segregation Part I, Trans. Met. Soc. AIME, 239 (1967) 1449-1461.

[8] H. Nomura, Y. Tarutani and K. Mori, Mathematical Model of Formation of Segregation Zone Caused by Volume Change in Solidification of Iron Steel, Tetsu-to-Hagane, 67 (1981) 1449-1461

[9] N. Mori, K. Ohgi and K. Matsuda, An Analytical Study of Macrosegregation in Ingot, Journal. of the Japan Institute of Metals, 43 (1979) 858-865.

[10] M.H. Burden and J.D. Hunt, Cellar and Dendritic Growth. I, J. of Crystal Growth 22 (1974) 99-108.

[11] T. Kawawa, Tekko-no-Gyouko (Solidification of steel), Appendix 4, ed. By Solidification Comm., Joint Sc. on Iron and Steel Basic Research of ISIJ, ISIJ, Tokyo, 1977.

[12] J. Chipman, Basic Open-Hearth Steelmaking, Physical Chemistry of Steelmaking Committee, Iron and Steel division, AIME, 1951, 632.

[13] M. Hirai, K. Kanamaru and H. Mori, Tekko-no-Gyouko (Solidification of steel), Appendix 4, ed. By Solidification Comm., Joint Sc. on Iron and Steel Basic Research of ISIJ, ISIJ, Tokyo, 1977.

[14] T. Kawawa and H. Tuchida, Tekko-no-Gyouko (Solidification of steel), Appendix 4, ed. By Solidification Comm., Joint Sc. on Iron and Steel Basic Research of ISIJ, ISIJ, Tokyo, 1977.

[15] T. Kawawa, H. Sato, S. Miyahara, T. Koyano and H. Nemoto, Determination of Solidifying Shell Thickness of Continuously Cast Slab by Rivet Pin Shooting, Tetsu-to-Hagane 60 (1974) 206–216

[16] J. Matsuno, H. Nakato and H. Ohi, An analysis of Solidification Rate and Surface Temperature of Continuous Casting Slabs, Tetsu-to-Hagane, 60 (1974) 1023–1032.

[17] E. Widawski, F. Sauerwald and Z. Anorg. , Allegem. Chem., 192 (1930) 145.

[18] Y.S. Touloukian, Thermophysical Properties of Matter, the TRPC Data Series, IFL/Plenum (1970), New York.

[19] W.A. Fisher, H. Splizer and M. Hishinuma, Das Zonenschmelzen von Eisen und die Ermittlung der Verteilungskoeffizienten für Kohlenstoff, Phosphor, Schwefel und Sauerstoff, Arch. Eisenhüttenwes. 31 (1960) 365–371.

[20] R. Tanaka, On the Recent Iron-Carbon Equilibrium Diagram, Tetsu-to-Hagane 53 (1967) 1586-1604.

[21] J. Chipman, Basic Open-Hearth Steelmaking, Physical Chemistry of Steelmaking Committee, Iron and Steel division, AIME, 1951, 632.

[22] T. Takahashi, M. Kudo, K. Ichikawa and Tanaka, Tekko-no-Gyoko (Solidification of Steel), Appendix 4, ed. by Solidification Comm. Joint Sc. on Iron and Steel Basic Research of ISIJ, ISIJ, Tokyo, (1977)

[23] W.A. Fisher and H. Frye, Arch. Eisenhüttenwes., 41 (1970) 293.

[24] T. Wada and H. Wada, Tekko-no-Gyoko (Solidification of Steel), Appendix 4, ed. by Solidification Comm. Joint Sc. on Iron and Steel Basic Research of ISIJ, ISIJ, Tokyo, (1977)

[25] K. Watanabe, T Tekko-no-Gyouko (Solidification of steel), Appendix 4, ed. By Solidification Comm., Joint Sc. on Iron and Steel Basic Research of ISIJ, ISIJ, Tokyo, 1977.

[26] K. Kumai, A. Sano, T. Ohashi, E. Nomura and H. Fujii, Study on Solidification Behavior, Solute Segregation and Fluid Flow in Continuously Cast Slab, Tetsu-to-Hagane 7 (1974) 894–914.

[27] R.E. Grace and G. Derge, Diffusion of Third Elements in Liquid Iron Saturated with Carbon, Trans. Metall. Soc. AIME 212 (1958) 313–337.

[28] T. Mori, K. Ayata, J. Fujisawa and H. Sako, Temperature and Thermal Stress in the Solidifying Shell of the Continuously Cast Steel, Tekko-no-Gyouko (Solidification of steel), ed. By Solidification Comm., Joint Sc. on Iron and Steel Basic Research of ISIJ, ISIJ, Tokyo, 1977, 237–239.

[29] M. Sugiyama, T. Umeda and J. Matsuyama, On Microsegregation and Microstructure in 18Cr-8Ni and 25Cr-20Ni Austenitic Stainless Steels, Tetsu-to-Hagane, 60 (1974) 1094-1113.

[30] T. Umeda, J. Matsuyama, H. Murayama and M. Sugiyama, Dendrite Morphology and Solute Redistribution during Solidification of 25Cr-20Ni Austenitic Stainless Steel, Tetsu-to-Hagane, 63 (1977) 441-449.

[31] K. Miyazawa and I. Muchi, Mathematical Model for Determining Solidification Profiles of Slab in the Vertical Type and Circular-arc Type Continuous Casting Machines, Trans. IJIS, 15 (1975) 37-44.

Chapter 3 Model II

Mathematical Analysis of the Solidification Behavior of Plain Steel Based on Solute- and Heat-Transfer Equations in the Liquid–Solid Zone

Abstract

An analytical approximate solution to nonlinear solute- and heat-transfer equations in the unsteady-state mushy zone of Fe–C plain steel has been obtained, assuming a linear relationship between the solid fraction and the temperature of the mushy zone. The heat transfer equations for both the solid and liquid zone along with the boundary conditions have been linked with the equations to solve the whole equations. The model predictions (e.g., the solidification constants and the effective partition ratio) agree with the generally accepted values and with a separately performed numerical analysis. The solidus temperature predicted by the model is in the intermediate range of the reported formulas. The model and Neumann's solution are consistent in the low carbon range.

A conventional numerical heat analysis (i.e., an equivalent specific heat method using the solidus temperature predicted by the model) is consistent with the model predictions for Fe–C plain steels. The model presented herein simplifies the computations to solve the solute- and heat-transfer simultaneous equations while searching for a solidus temperature as a part of the solution. Thus, this model can reduce the complexity of analyses considering the heat- and solute-transfer phenomena in the mushy zone.

[Note] Model II adopts the Dirichlet conditions and Neumann conditions as the boundary conditions.

3.1 Introduction

Numerical methods are effectively used to simulate heat transfer phenomena during solidification processes. While these methods provide reliable surface temperatures (i.e., those calibrated with the measured values), inner temperatures, especially at the solidus point, are not generally confirmed with the actual (measured) values. The main reason for these problems lies in the difficulty [1] of achieving reliable results while measuring the solidus position during the casting process with an associated solidus temperature for general carbon steels. In addition, the fraction of solid in a solid–liquid coexisting zone (i.e., mushy zone) remains partly unknown.

With respect to the liquidus temperature, while it is not also generally measured during the casting process, the problems are not serious because micro-segregation at the dendrite tips is so small that super-cooling is limited only a few degrees. Therefore, the liquidus temperature for Fe–C plain steel can be estimated from the phase diagram or from measurements which are in reasonable agreement with each other. However, with regard to the solidus temperature of steel, discrepancies exist between estimates of solidus temperature based on the phase diagram and models accounting for microsegregation. (i.e. 40 K discrepancies [2-5]). Recently, Gryc et al. [6] thermoanalytically measured the solidus temperature for various steel grades and reported significant discrepancies between the measurements and the values obtained from reported formulas (up to 42 K) or thermodynamic calculations (up to 50 K). These discrepancies could lead to considerable errors while estimating the position at which the shell develops with a target thickness.

The lack of knowledge about the fraction of solid in the mushy zone has spurred the onset of numerous methods based on heat analysis: (A) methods [7-9] assuming a linear relationship between the solid fraction and the temperature (e.g., equivalent specific heat model); (B) methods [10,11] assuming the equilibrium lever rule, the Scheil equation, and back diffusion models such as the Brody–Flemings model [12] or the Clyne–Kurz [13] model; (C) methods [14] recovering the temperature with the latent heat release after solidification. However, these methods are not always consistent with the real solidification process. For example, (C) methods assume that the primary dendrites should grow after solidification. When the (B) methods are used along the dendrite axial direction, a flat boundary surface should be assumed for the dendritic mushy zone. When the (B) models are applied along to the normal to the dendrite axis direction (radial direction), diffusion along the dendrite axis direction should be neglected. However, diffusion along the primary dendrite axis is not negligible since the effective partition ratio of carbon is typically close to 0.9 (0.85–1.0) for continuously cast steels [15]. Thus, the fraction of solid used in the thermal analysis should be consistent with general findings (e.g., solute diffusions along the primary dendrites axis) such that these heat analysis results are in line with general findings.

At the early stage of the solidification process (e.g., the chill zone), the issues mentioned above are not relevant because the mushy zone is not fully developed and because the solidus and liquidus surfaces are close together forming a substantially planar boundary.

At the middle stage of the solidification process, the mushy zone is fully developed, and the solidification process in this region should be taken into account. Asai et al. [16], Hills et al. [17], and Alexandrov et al. [18] obtained analytical or approximate analytical solutions assuming steady-state conditions (i.e., constant solidification velocity). However, these analytical solutions cannot be directly used for general solidification

processes because the solidification velocity significantly changes with time. In addition, general thermal analysis assuming unsteady state solidification does not provide the data which are consistent with those obtained from the steady-state analyses.

In the case of unsteady state solidification at the middle stage, numerical analyzes are generally performed because of the difficulties to obtain the exact simultaneous solutions for the non-linear heat- and solute-transfer equations. Takeshita [19] obtained the simultaneous solutions for the NH_4Cl aqueous eutectic system after analytically eliminating the solid fraction-related terms in the equations. Although extensive numerical computation was required to obtain the unknown solid fraction at the eutectic point where the solidus temperature and the solute concentration are given by the phase diagram, the solution was obtained as simultaneous solutions of the nonlinear heat- and solute-transfer equations.

Regarding the analytical solutions for unsteady state solidification, Huppert et al. [20] and Alexandrov [21] proposed models for aqueous chimney-type solidifications. However, these models focusing on a special cases, such as a liquidus position develops exclusively while the solidus point hardly develops, cannot be applied for the solidification of general steels, because it is well known that the solidus point typically develops with the associated liquidus point during the solidification of general steels.

The approximate analytical solutions for a multi-component alloy system have been demonstrated by Fujimura et al. [22] solving the nonlinear heat- and solute-transfer equations with a moving coordinate system. The predicted effective partition ratios for a typical steel and shell thickness were in good agreement with the reported measurements. However, only the Dirichlet conditions (e.g., constant temperature and solute concentrations at the solidus point) at the boundaries have been assigned without adopting the boundary conditions generally used in heat analysis (i.e., Neumann-type boundary conditions). Consequently, this solution needs the measured solidification constants for the solidus and liquidus positions, and the accuracy of the model predictions strongly depends on the dispersion of these measurements. In addition, the results of the analysis cannot be directly linked with the thermal analysis results because of the insufficient boundary conditions.

To resolve these issues and obtain more reliable thermal analysis data, we expanded the analyzed regions to the entire system as compared to the previous model that considered only the mushy zone. The unknown solidification constants should be obtained as part of the solutions upon assigning the additional boundary conditions. A plain Fe–C binary system is subjected to analysis since carbon is the dominant solute influencing the phase diagram. Additionally, the simplifications that help making a model as simple as possible have been adopted.

3.2 Mathematical Model

3.2.1 Solidification Problems

The solidification problems mathematically modeled and the volume element studied are schematically shown in Fig. 3.1. Heat is unidirectionally extracted and a solid shell is considered to grow from the surface. In the mushy zone, heat and solute are considered to transfer by conduction and diffusion, respectively. The main assumptions made in the model formulation, which are in agreement with the previous model[22] for multicomponent alloy systems, are as follows:

(1) Heat is exclusively extracted by heat conduction along the primary dendrite axis (i.e., x axis) direction.

(2) The density and specific heat of the liquid are the same as those of the solid in a mushy zone.

(3) The solute is exclusively transported by diffusion via moderate fluid flow in the mushy zone.

(4) The dependency of the equilibrium partition ratio and the solute interdiffusion coefficient on the solute concentration is negligible.

(5) The effect of the dendrite tip curvature on the liquidus temperature is negligible.

(6) Undercooling within the mushy zone is negligible.

(7) The diffusion of the solute, carbon, in the liquid within the mushy zone is sufficiently rapid to achieve a homogeneous composition in the direction normal to that of the heat extraction (i.e., primary dendrite radial direction) over a distance in the order of the primary dendrite arm spacing. Generally, the magnitude of the primary dendrite arm spacing in cast steels (continuously cast or into static ingot) is in the range of 50–500 μm except in the chill zone.

(8) Local equilibrium between the liquid and the solid surfaces in the volume element is achieved (This assumption was also considered by Asai et al., [16] Takeshita [19], Huppert et al. [20] and Fujimura et al. [22]).

(9) As considered in conventional heat analysis, the fraction of solid in the mushy zone is assumed to be linear to the temperature.

From the mathematical point of view, the heat- and solute-transfer equations should be simultaneously solved for the liquid and solid in the mushy zone which are subjected to the boundary conditions of the moving solidus and liquidus boundaries at initial conditions. However, the problem can be simplified upon the assumption that the boundary values (i.e., temperature and solute concentration) are constant. The same assumption was previously made by Asai et al. [16], Takeshita [19], and Fujimura et al. [22].

Another important methodology of the models is achieved by the assumption (8) as follows: If the models (B) mentioned before (i.e., the equilibrium lever rule) are adopted in the volume element, the solidus temperature should be that dictated on the solidus line of the phase diagram with the initial bulk liquid concentration (Fig. 1, c‐f temperature line). On the other hand, the solidus temperature is obtained on the liquidus line of the phase diagram liquidus line where the residual liquid completes the solidification (Fig. 3.1, b–e temperature line). This is the key methodology of the model which was adopted in many models [16,19,20,22].

In the following analysis, the diffusion of the solute along the primary dendrite axis direction (i.e., x axis) resulting the dilution of the solute in the mushy zone is considered, and the solute- and heat-transfer equations will be simultaneously solved.

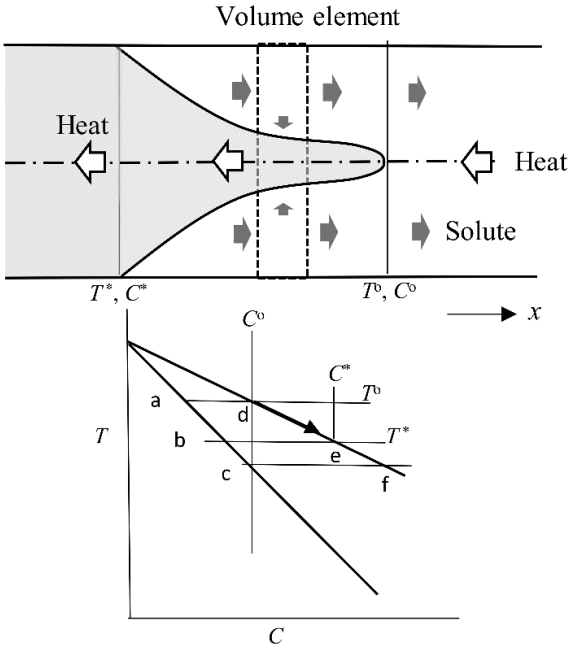

Fig. 3.1 Schematic of the solidification problem under study.

3.2.2 Mathematical Formulations

The preconditions and assumptions made in the model are as follows, which correspond to three zones, [I] solid zone, [II] mushy zone, and [III] liquid zone, are as follows:

[I zone]

(I) The liquid initially held at T^{i} is instantaneously kept at T^{s} at the surface ($x = 0$) and solidification begins.

(II) As is typical of continuously cast steels, the thickness of the cast steel is large.

[II zone]

(II1) The objective steel is Fe–C binary steel.

(II2) The liquidus temperature is coupled with the solute concentration by the liquidus surface of the phase diagram that can be represented by the following equation, as proposed by Kawawa et al. [23].

$$T = T_M + mC \quad (3.1)$$

T_M：Solidus temperature of pure liquid (K)

m ： Temperature gradient of the liquidus line with respect to the solute concentration（K/%）

C : Solute concentration (%) of the liquid in the mushy zone.

(II3) A linear relationship between the liquid fraction f and the temperature T is assumed as follows:

$$f = \frac{T - T^*}{T^o - T^*} \quad (3.2)$$

T^o: Liquidus temperature

T^*: Solidus temperature

The following equation is obtained using 1) and 2):

$$f = \lambda C + s \quad (3.3)$$

By the definition of solid fraction f_s and f, one obtains:

$$1 = f + f_s \quad (3.4)$$

f_s ：fraction solid

λ、s ：unknown constants

(II3) $T = T^*$ at Ⅰ / Ⅱ boundary ($x = x^*$ solidus point)

(II4) $T = T^o$ at Ⅱ / Ⅲ boundary ($x = x^o$ liquidus point)

[III zone]

The liquid temperature at the center of cast steel is assumed to remain constant at T^i (as will be discussed later, the numerical analysis showed that this assumption is practically reasonable). We denote the solute concentration at the liquidus and solidus positions as C^o and C^*, respectively, and the following equations are obtained:

At the liquidus point:

$$1 = \lambda C^o + s \quad : x = x^o,\ f = 1 \quad (3.5)$$

$$T^o = T_M + mC^o \quad : x = x^o,\ T = T^o,\ C = C^o \quad (3.6)$$

At the solidus point:

$$0 = \lambda C^* + s \quad : x = x^*,\ f = 0 \quad (3.7)$$

$$T^* = T_M + mC^* \quad : x = x^*,\ T = T^*,\ C = C^* \quad (3.8)$$

Combining Eq. (3.4)– (3.8), the following equations are obtained:

$$\lambda = \frac{\mathrm{m}}{T^{\mathrm{o}} - T^{*}} \tag{3.9}$$

$$s = \frac{T_{\mathrm{M}} - T^{*}}{T^{\mathrm{o}} - T^{*}} \tag{3.10}$$

The density, the specific heat, and the thermal conductivity of each zone are referred as ρ_i, Cp_i, K_i (i represents the zone), while L represents the latent heat. The heat balance equations are as follows in the three zones.

[I zone]

$$\rho_1 Cp_1 \frac{\partial T}{\partial t} = K_1 \frac{\partial^2 T}{\partial x^2} \tag{3.11}$$

$$x = 0 \quad : T = T^{\mathrm{s}} \tag{3.12}$$

$$x = x^{*} \; : T = T^{*} \tag{3.13}$$

[II zone]

$$\rho_2 Cp_2 \frac{\partial T}{\partial t} + \rho_2 L \frac{\partial f}{\partial t} = K_2 \frac{\partial^2 T}{\partial x^2} \tag{3.14}$$

$$x = x^{*} \quad : T = T^{*} \tag{3.15}$$

$$x = x^{\mathrm{o}} \quad : \; T = T^{\mathrm{o}} \tag{3.16}$$

By substituting 2) in 14) we obtain:

$$\left\{ \rho_2 Cp_2 + \rho_2 L/(T^{\circ} - T^{*}) \right\} \frac{\partial T}{\partial t} = K_2 \frac{\partial^2 T}{\partial x^2} \tag{3.17}$$

The Neumann's boundary equation [24] is needed if mushy zone does not exist. The heat accumulation by the conduction at the interface and the latent heat generation due to the moving of interface should be related to the velocity of moving interface. However, the boundary conditions are simplified as are used in the conventional heat analysis for the present case.

$$-K_1 \left.\frac{\partial T}{\partial x}\right|_{x^{*}} + K_2 \left.\frac{\partial T}{\partial x}\right|_{x^{*}} = 0 \tag{3.18}$$

$$-K_2 \left.\frac{\partial T}{\partial x}\right|_{x^{\circ}} + K_3 \left.\frac{\partial T}{\partial x}\right|_{x^{\circ}} = 0 \tag{3.19}$$

[III zone]

$$\rho_3 Cp_3 \frac{\partial T}{\partial t} = K_3 \frac{\partial^2 T}{\partial x^2} \tag{3.20}$$

$$t = 0 \quad : T = T^{\mathrm{i}} \tag{3.21}$$

$$x = x^{\mathrm{o}} \; : T = T^{\mathrm{o}} \tag{3.22}$$

These equations are transformed with the similarity variables defined as Eq. (3.23), (3.24), and (3.25) that are conventionally used to yield the ordinary differential equations as shown below. It should be noted that

these transformations fit well with an infinite molten liquid. However, the thickness of the continuously cast steel is generally large enough to yield constant temperature at the central region of the slab.

$$\eta_1 = \frac{x}{2\sqrt{\beta_1 t}} \tag{3.23}$$

$$\eta_2 = \frac{x}{2\sqrt{\beta_2 t}} \tag{3.24}$$

$$\eta_3 = \frac{x}{2\sqrt{\beta_3 t}} \tag{3.25}$$

$$\beta_1 = \frac{K_1}{\rho_1 Cp_1} \tag{3.26}$$

$$\beta_2 = \frac{K_2}{\rho_2 Cp_2 + \frac{\rho_2 L}{(T^\circ - T^*)}} \tag{3.27}$$

$$\beta_3 = \frac{K_3}{\rho_3 Cp_3} \tag{3.28}$$

The following ordinary differential equations and solutions in three zones are obtained by the above transformations.

[I zone]

$$-2\eta_1 \frac{dT}{d\eta_1} = \frac{d^2T}{d\eta_1^2} \tag{3.29}$$

$$x = 0 \quad \eta_1 = 0 \quad : T = T^s \tag{3.30}$$

$$x = x^* \quad \eta_1 = \eta_1^* \quad : T = T^* \tag{3.31}$$

$$T = \frac{(T^* - T^s)}{\mathrm{erf}(\eta_1^*)} \mathrm{erf}(\eta_1) + T^s \tag{3.32}$$

[II zone]

$$-2\eta_2 \frac{dT}{d\eta_2} = \frac{d^2T}{d\eta_2^2} \tag{3.33}$$

$$x = x^* \quad \eta_2 = \eta_2^* \quad : T = T^* \tag{3.34}$$

$$x = x^o \quad \eta_2 = \eta_2^o \quad : T = T^o \tag{3.35}$$

$$T = \frac{(T^* - T^o)\{\mathrm{erf}(\eta_2) - \mathrm{erf}(\eta_2^o)\}}{\{\mathrm{erf}(\eta_2^*) - \mathrm{erf}(\eta_2^o)\}} + T^o \tag{3.36}$$

[III zone]

$$-2\eta_3 \frac{dT}{d\eta_3} = \frac{d^2T}{d\eta_3^2} \tag{3.37}$$

$$t = 0 \quad \eta_3 = \infty \qquad : T = T^i \tag{3.38}$$

$$x = x^o \quad \eta_3 = \eta_3^o \qquad : T = T^o \tag{3.39}$$

$$x = x^c \quad \eta_3 = \eta_3^c \qquad : \; T = T^c \approx T^i \tag{3.40}$$

$$T = \frac{(T^o - T^i)\{\, 1 - \mathrm{erf}(\eta_3)\}}{\{1 - \mathrm{erf}(\eta_3^o)\}} + T^i \tag{3.41}$$

where $T^c\,(\eta_3{}^c) \approx T^i$ because $\eta_3{}^c$ at the center of the slab is kept large in a general continuous casting (*i.e.* the temperature drop of T^c is few degrees as shown in the later chapter).

Note that the following T^∞ obtained from Eq.(3.36) by adopting $\eta_2 = \infty$ was the extrapolated temperature out the range of the zone (II). This T^∞ will be used in the later chapter.

$$T^\infty = \frac{(T^* - T^o)\{1 - \mathrm{erf}(\eta_2^o)\}}{\{\mathrm{erf}(\eta_2^*) - \mathrm{erf}(\eta_2^o)\}} + T^o \tag{3.42}$$

3.2.3 Heat and Solute Transportations in the Mushy Zone

The solute discharged from the growing solid is transferred to the solidification direction (along the primary dendrite axis direction) by diffusion. The diffusivity, inter-diffusion coefficient, of the solute in the solid was referred as D while that in the liquid is denoted as E.

The variation of the solute concentration within a volume element with respect to time is given by:

$$\frac{\partial(f\,C + f_s \overline{C}_s)}{\partial t} = \frac{\partial}{\partial x}\left\{E f \frac{\partial C}{\partial x}\right\} + \frac{\partial}{\partial x}\left\{D f_s \frac{\partial \overline{C}_s}{\partial x}\right\} \tag{3.43}$$

C_s : solute concentration of the solid surface, which is in equilibrium with the liquid

$\overline{C}_s$: averaged solute concentration in solid

The variation of the solute concentration in the solid (i.e., the second term of the left-hand of Eq. (3.43) is given by using the parameter α:

$$\frac{\partial(f_s \overline{C}_s)}{\partial t} = C_s \frac{\partial f_s}{\partial t} + f_s \frac{\partial(\alpha\, C_s)}{\partial t} \tag{3.44}$$

where α is a parameter [16] having a value of 0 or 1 that defines the diffusion limits in the solid (i.e., α = 0 when the diffusion of the solute in the solid is negligible and α = 1 when the diffusion in the solid, such as the case of carbon, is rapid enough to result in homogeneous composition over distances in the order of the primary dendrite diameter).

C_s is related to C with the partition ratio k by the following equation:

$$C_s = \mathrm{k}\, C \tag{3.45}$$

Substituting Eqs.(3.4), 44), and (3.45) into (3.43) yields:

$$\frac{\partial\{f(1-\alpha\mathrm{k})C+\alpha\mathrm{k}C\}}{\partial t} = E\frac{\partial}{\partial x}\left\{f\frac{\partial C}{\partial x}\right\}+\alpha\mathrm{k}D\frac{\partial}{\partial x}\left\{(1-f)\frac{\partial C}{\partial x}\right\} \tag{3.46}$$

Transforming with Eq.(3.24) provides the following ordinary equation.

$$\begin{aligned}&\{\lambda(2-\mathrm{k}\text{-}\alpha\mathrm{k}\}C+s(1-\alpha\mathrm{k})+\alpha\mathrm{k}\}(\text{-}2\eta_2\beta_2)\frac{\mathrm{d}C}{\mathrm{d}\eta_2}\\ &\quad=\lambda(E-\alpha\mathrm{k}D)\left(\frac{\mathrm{d}C}{\mathrm{d}\eta_2}\right)^2+\{\lambda(E-\alpha\mathrm{k}D)C+s(E-\alpha\mathrm{k}D)+\alpha\mathrm{k}D\}\frac{\mathrm{d}^2C}{\mathrm{d}\eta_2^2}\end{aligned} \tag{3.47}$$

Substituting Eq.(3.1) to the heat balance Eq.(3.33) gives

$$\text{-}\,2\eta_2\frac{\mathrm{d}C}{\mathrm{d}\eta_2} = \frac{\mathrm{d}^2C}{\mathrm{d}\eta_2^2} \tag{3.48}$$

The boundary conditions Eqs.(3.34) and (3.35) can be characterized as follows:

$$\text{at } x = x^* \qquad \eta_2 = \eta_2^*\ ,\ C = C^*\ ,\ f = 0 \tag{3.49}$$

$$\text{at } x = x^{\mathrm{o}} \qquad \eta_2 = \eta_2^{\mathrm{o}}\ ,\ C = C^{\mathrm{o}}\ ,\ f = 1 \tag{3.50}$$

To simultaneously solve Eqs.(3.47) and (3.48), the unknown constants are determined to match both the first-order differential equation obtained by Eq.(3.48) and that obtained by eliminating the second-order differential terms from Eq.(3.47). Integrating Eq.(3.48) twice with Eqs.(3.49) and (3. 50) yields

$$C = \frac{(C^*-C^{\mathrm{o}})\{\mathrm{erf}(\eta_2)\text{ - }\mathrm{erf}(\eta_2^{\mathrm{o}})\}}{\{\mathrm{erf}(\eta_2^*)\text{ - }\mathrm{erf}(\eta_2^{\mathrm{o}})\}} + C^{\mathrm{o}} \tag{3.51}$$

Differentiating Eq.(3.51) gives

$$\frac{\mathrm{d}C}{\mathrm{d}\eta_2} = \frac{(C^*\text{- }C^{\mathrm{o}})}{\{\mathrm{erf}(\eta_2^*)\text{ - }\mathrm{erf}(\eta_2^{\mathrm{o}})\}}\cdot\frac{2\exp(\text{-}\eta_2^2)}{\sqrt{\pi}} \tag{3.52}$$

Eliminating the second-order differential terms from Eqs.(3.47) and (3.48) and defining the constants F^{o} and G^{o} as follows yields

$$\frac{\mathrm{d}C}{\mathrm{d}\eta_2} = (\text{-}2\eta_2)(F^{\mathrm{o}}C + G^{\mathrm{o}}) \tag{3.53}$$

$$F^{\circ} = \frac{(2-\mathrm{k}-\alpha\mathrm{k})}{(E-\alpha\mathrm{k}D)}\beta_2 - 1 \tag{3.54}$$

$$G^{\circ} = \frac{s}{\lambda}\left\{\frac{(1-\alpha\mathrm{k})}{(E-\alpha\mathrm{k}D)}\beta_2 - 1\right\} + \frac{\alpha\mathrm{k}(\beta_2 - D)}{\lambda(E-\alpha\mathrm{k}D)} \tag{3.55}$$

Substituting Eq.(3.51) into (3.53) gives

$$\frac{dC}{d\eta_2} = (-2\eta_2)\left[\left[\frac{(C^* - C^o)\{\mathrm{erf}(\eta_2) - \mathrm{erf}(\eta_2^o)\}}{\{\mathrm{erf}(\eta_2^*) - \mathrm{erf}(\eta_2^o)\}} + C^o\right]F^o + G^o\right] \tag{3.56}$$

The following equation is a good approximation [22] of the error-function of η for large η (Appendix 3.1).

$$\mathrm{erf}(\eta) \approx 1 - \frac{\exp(-\eta^2)}{\eta\sqrt{\pi}} \tag{3.57}$$

Adopting this approximation to Eq. (3.56) yields

$$\frac{dC}{d\eta_2} = F^o\frac{(C^* - C^o)}{\{\mathrm{erf}(\eta_2^*) - \mathrm{erf}(\eta_2^o)\}}\cdot\frac{2\exp(-\eta_2^2)}{\sqrt{\pi}} - (2\eta_2)\left[\left[\frac{(C^* - C^o)\{1 - \mathrm{erf}(\eta_2^o)\}}{\{\mathrm{erf}(\eta_2^*) - \mathrm{erf}(\eta_2^o)\}} + C^o\right]F^o + G^o\right] \tag{3.58}$$

The followings expressions are obtained to match Eq.(3.52) with (3.58).

$$F^o = 1 \tag{3.59}$$

$$\left[\frac{(C^* - C^o)\{1 - \mathrm{erf}(\eta_2^o)\}}{\{\mathrm{erf}(\eta_2^*) - \mathrm{erf}(\eta_2^o)\}} + C^o\right]F^o + G^o = 0 \tag{3.60}$$

Substituting Eq.(3.59) into (3.54) results in

$$\beta_2 = \frac{2(E - \alpha k)}{(2 - k - \alpha k)} \tag{3.61}$$

Substituting Eq.(3.27) into (3.9) gives

$$\lambda_2 = \frac{m}{\rho_2 L}\left(\frac{K_2}{\beta_2} - \rho_2 C p_2\right) \tag{3.62}$$

Substituting Eq.(3.62) into (3.5) gives

$$s = 1 - \frac{m}{\rho_2 L}\left(\frac{K_2}{\beta_2} - \rho_2 C p_2\right) \tag{3.63}$$

Note that β_2, λ, and s satisfy Eqs.(3.27),(3.9) and (3.10). C^* is obtained using Eqs.(3.7), (3.62) and (3.63) as follows:

$$C^* = C^\circ - \frac{1}{\frac{m}{\rho_2 L}\left(\frac{K_2}{\beta_2} - \rho_2 C p_2\right)} \tag{3.64}$$

C_s^* is obtained with Eq.(3.45) as follows:

$$C_s^* = kC^* \tag{3.65}$$

Assuming the concentration of the solute at the liquidus position is equal to that of bulk liquid, T^{o} and T^{*} are obtained by Eq.(3. 6) and (3.8). The condition (3.60) which closes the simultaneous equations, is formulated using Eqs.(3.1) and (3.42) as follows:

$$\left[\frac{(T^{*}-T^{o})\{1-\mathrm{erf}(\eta_2^{o})\}}{\{\mathrm{erf}(\eta_2^{*})-\mathrm{erf}(\eta_2^{o})\}}+T^{o}-T_{\mathrm{M}}\right]\frac{F^{o}}{\mathrm{m}}+G^{o}=(T^{\infty}-T_{\mathrm{M}})\frac{F^{o}}{\mathrm{m}}+G^{o}=0 \tag{3.66}$$

where F^{o}=1 as shown in Eq.(3.59), G^{o} is expressed in terms of T^{*} by substituting Eqs.(3.9), (3.10), and (3.61) into Eq.(3.55) and $T^{\infty}$is expressed in terms of T^{*}, η_2^{*}, η_2^{o} and T^{*}as in Eq.(3.41). Substituting these G^{o}, F^{o}, and T^{∞} into Eq.(3.66) gives the following equation which shows the requirement for three unknown constants η_2^{*},η_2^{o} and T^{*},

$$\frac{T^{\infty}-T^{\circ}}{T^{*}-T^{\circ}}=\frac{\{1-\mathrm{erf}(\eta_2^{\circ})\}}{\{\mathrm{erf}(\eta_2^{*})-\mathrm{erf}(\eta_2^{\circ})\}}=\frac{2(1-\mathrm{k})}{(2-\mathrm{k}-\alpha\mathrm{k})}C^{\circ}\lambda+\frac{(1+\alpha\mathrm{k})\mathrm{k}}{(2-\mathrm{k}-\alpha\mathrm{k})}-\frac{\alpha\mathrm{k}D}{E-\alpha\mathrm{k}D} \tag{3.67}$$

where λ is given with T^{*} using Eq.(3.9). It should be noted that E in the right-hand of Eq.(3.67) should satisfy the following equation given by Eqs.(3. 27) and (3.61).

$$\frac{2(E-\alpha\mathrm{k})}{(2-\mathrm{k}-\alpha\mathrm{k})}=\frac{K_2}{\rho_2 Cp_2+\dfrac{\rho_2 L}{T^{\circ}-T^{*}}} \tag{3.68}$$

Eqs.(3.23),(3.24), and (3.25) give the following expressions:

$$\eta_2^{*}=\sqrt{\frac{\beta_1}{\beta_2}}\,\eta_1^{*} \tag{3.69}$$

$$\eta_2^{o}=\sqrt{\frac{\beta_3}{\beta_2}}\,\eta_3^{o} \tag{3.70}$$

Substituting Eqs.(3.32), (3.36), (3.41), and (3.69) and (3.70) into the boundary conditions, (3.18) and (3.19) give

$$\frac{K_1(T^{*}-T^{\circ})\exp\left\{(1-\dfrac{\beta_2}{\beta_1})(\eta_2^{*})^2\right\}}{(T^{*}-T^{\circ})\mathrm{erf}(\sqrt{\dfrac{\beta_2}{\beta_1}}\,\eta_2^{*})\sqrt{\beta_1}}=\frac{K_2}{\left\{\mathrm{erf}(\eta_2^{*})-\mathrm{erf}(\eta_2^{\circ})\right\}\sqrt{\beta_2}} \tag{3.71}$$

$$\frac{K_3(T^{i}-T^{\circ})\exp\left\{(1-\dfrac{\beta_2}{\beta_3})(\eta_2^{\circ})^2\right\}}{(T^{*}-T^{\circ})\left\{1-\mathrm{erf}(\sqrt{\dfrac{\beta_2}{\beta_3}}\,\eta_2^{\circ}\right\}\sqrt{\beta_3}}=\frac{K_2}{\left\{\mathrm{erf}(\eta_2^{*})-\mathrm{erf}(\eta_2^{\circ})\right\}\sqrt{\beta_2}} \tag{3.72}$$

Three unknown constants T^{*}, η_2^{*}, and η_2^{o} are easily fixed to match Eqs.(3. 67), (3.71), and (3.72) with

the try and error method (the process is shown in Appendix 3.2), where K_1, K_2, K_3, β_1, and β_3 are given by the reported physical properties, and T^i, T^s, and T^o are given as initial conditions. The liquidus temperature T^o is estimated with the reported formula [23] and both β_2 and λ are expressed in terms of T^* by Eq.(3.27) and (3.9). It should be noted that the third term in the right-hand of Eq.(3.67) is negligible because D is significantly smaller than E. Consequently, the three equations exclusively involve the three unknown constants (T^*, η_2^*,and $\eta_2{}^o$), such that these unknown constants should be able to be fixed. Fixing the three unknown constants takes several minutes by manual calculation with spreadsheets or, alternatively, it can be instantly obtained if the algorithm shown in Appendix 3.2 is used either with a personal or a tablet computer.

The interdiffusion coefficient E is estimated with Eq.(3.61) or Eq.(3.68) after closing the simultaneous equations (i.e., after fixing T^*, η_2^*, and $\eta_2{}^o$). The interdiffusion coefficient D in the solid is referred to reported measurements. Finally, the solidus and liquidus positions $x^*$and x^o, respectively, as a function of time are given by Eq.(3.24) with η_2^* and η_2^o as follows:

$$x^* = 2\eta_2^*\sqrt{\beta_2 t} \tag{3.73}$$

$$x^o = 2\eta_2^o\sqrt{\beta_2 t} \tag{3.74}$$

Thus, the heat- and solute-transfer equations are simultaneously solved without the measured solidification constants (as required in the previous model [22]. The fractions of solid in the mushy zone are predicted by Eq.(3.2). The temperature in the solid, mushy, and liquid zones are predicted with Eqs.(3.32), (3.36), and (3.41), respectively. The solute concentration in the mushy zone is also predicted with Eq. (3.1) or (3.51). It should be noted that the predicted solidus temperature T^* is determined as a part of the simultaneous solutions.

3.3 Model Validations and Discussions

3.3.1 Physical Properties

The physical properties used in the model are listed in Table 3.1. The values selected for the thermal conductivity in the mushy zone warrants discussion because the measurements have not been made under the conditions corresponding to this solid–liquid region, particularly with respect to the fluid flow.

Thermally driven flow adjacent to the solidification front can give rise to estimated velocities of 0.001–0.01 m/s [8,25] while solidification shrinkage may generate a fluid velocity of 0.001 m/s [26–28]. Consequently, the thermal conductivity in the mushy zone could be larger than that measured in a stagnant liquid. However, this difference is not expected to be great because heat flow via conduction is larger as compared to convection at the low fluid velocities used herein. Moreover, a significant fraction of solid of the

mushy zone consisted of fixed solid dendrites unaffected by the fluid flow. Thus, the thermal conductivities [29] measured under stagnant conditions, were used in the present model.

The same argument does not hold when considering the interdiffusion coefficients in the interdendritic liquid because the rate of solute transport by diffusion is low as compared to convection. Hence, the interdiffusion coefficients measured in a stagnant liquid cannot be used for the interdendritic region. However, the diffusivity and interdiffusion coefficients of carbon can be estimated with Eq.(3.68). This approach used herein was also employed in the previous model [22]. The estimated interdiffusion coefficient, including the influence of the fluid flow, should be greater than the values measured under stagnant conditions.

In general, a molten steel at a temperature of around 1812 K (1539 °C) is poured into a water-cooled mold. Initial solidification begins upon chilling with the water cooled mold and subsequent cooling by water spraying. The slab surface temperature is generally measured with optical instruments generally installed in the lower positions of a caster because of the facility restrictions. Under such circumstances, Meng et al. [30] performed a reliable and continuous measurements of a continuously cast 0.45%C steel by means of a thermocouples with a block fed into a mold. Considering their analysis, the surface temperature is assumed to remain at 1423 K (1150 °C) during solidification. The molten steel super-heat (i.e., the over heat of the bulk liquid against the liquidus temperature) was assumed to be 15 K (15 °C) as is common for a general continuously cast steel.

The influence of the carbon partition ratio on the solidus temperature is high while the reported carbon partition ratios k for a δ phase are in the range of 0.13–0.29 [31,32] except for the low carbon steel (0.023% C). The representative value [33,34] of this range (k = 0.225) was used in this model . This k value can be changed as discussed in later chapters.

Table 3.1 Physical properties employed in the model

	Property		Value
I zone	ρ_1	density	7.7×10^3 Kg/m^3
	Cp_1	specific heat	0.77 kJ/kgK
	K_1	thermal conductivity	30.6 W/mK
	L	heat of fusion	276 kJ/kg
II zone	ρ_2	density	7.5×10^3 Kg/m^3
	Cp_2	specific heat	0.77 kJ/kgK
	K_2	thermal conductivity	31.8 W/mK
	k	partition ratio of C in δ-Fe	0.225[33,34]
	D	interdiffusion coefficients of solid	6.6×10^{-10} m2/sec [40]
III zone	ρ_3	density	7.4×10^3 Kg/m^3
	Cp_3	specific heat	0.77 kJ/kgK
	K_3	thermal conductivity	31.8 W/mK
Liquidus temperature [23]			$T^\circ = 1809 - 78(\%C) - 4.9(\%Mn) - 7.6(\%Si)$ K

3.3.2 Thermal Analysis

The temperature transition of a plain steel (0.15% C) slab with 0.22 m in thickness as predicted by the present model after 240 s lapse from the solidification start is shown in Fig. 2. The surface T^s and initial T^i temperatures were 1423 and 1812 K (1150 and 1539 °C) (superheat $\Delta T = 15$ K (15 °C)), respectively. The thickness of the mushy zone was 1.4×10^{-2} m and the solidification constants for the solidus and liquidus points were 2.55×10^{-3} and 3.44×10^{-3} m/s$^{1/2}$, respectively, which are in the range of generally accepted values [1,15]. The temperature gently decreased from the center of the slab to the liquidus point. Subsequently, the slope increased toward the solidus point while smoothly passing the solidus point.

The numerical heat analysis was separately performed (shown by a dashed line). The consistencies with respect to the solidus and liquidus points between the analytical solutions and the numerical heat analysis were examined by using the solidus temperature T^* estimated by the present model. The conventional equivalent specific heat method (according to the procedure by Katayama et al. [35]) and the upwind finite difference methods were adopted in the numerical analysis, assuming a linear relationship between the solid fraction and the temperature, as assumed in the model. The boundary conditions (3.18), (3.19), and the symmetric condition at the center region of the slab were adopted.

As shown in Fig. 3.2, the analytical solutions and the numerical analysis were in good agreement with respect to the temperature and both the solidus and liquidus positions. Better agreements were obtained upon increasing the partitioning of the objective slab (e.g., the accuracy of the solidus point obtained by the numerical analysis was less than 0.3% with a partitioning of 4000 for a half thickness slab).

Concerning to the drop of temperature in the center region, it was estimated to be 3 K (3 °C) with the numerical analysis, and this value is within the accuracy range of the temperature measurements [36]. Consequently, the assumption of constant temperature at the center of the slab made in the model formulations was reasonable, at least it should be allowed from the practical viewpoint.

It should be noted that a conventional numerical heat analysis that satisfies the solute-transfer equation needs extensive computation to search for the solidus temperature with the associated solid fraction in a mushy zone which is obtained by the model while accounting for the heat and solute balances in a large quantity of volume elements.

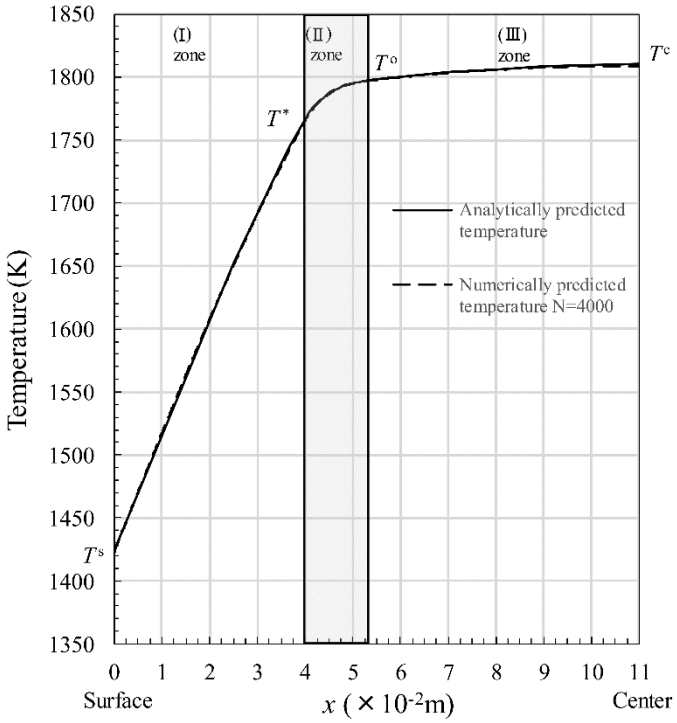

Fig. 3.2 Temperature distributions predicted by the model and numerical analysis of a continuously cast steel. (0.15% C, T^s = 1423 K (1150 ℃), ΔT = 15 K (15 ℃), t = 240 s, slab thickness = 0.22 m, N = partitioning number of the half thickness of a slab).

3.3.3 Material Analysis

The transition of the solute concentration and the liquid fraction in the mushy zone predicted by the

model is shown in Fig. 3.3. The estimated carbon interdiffusion coefficient E for a 0.15% C steel was 3.8 $\times 10^{-7}$ m^2/s which was in good agreement with the reported values by Asai et al. [16] (4.7 $\times$ 10^{-7} m^2/s) and by Fujimura et al. [22] (3.98 $\times$ 10^{-7} m^2/s) estimated for a Fe-0.15%C-0.70%Mn-0.22% Si continuously cast steel. Although the estimated interdiffusion coefficient obtained by the model was somewhat larger than that measured by Grace et al. [37] (2–4 $\times$ 10^{-7} m^2/s) under stagnant conditions, this is reasonable as discussed earlier.

The carbon concentration at the solidus point (defined as C/C^o) predicted by the present model was 3.9 and was in good agreement with that estimated by the previous model [22] for a 0.15%C low-alloyed steel (C/C^o = 3.8). The effective carbon partition ratio k^{ef} (0.89) was in the range of reported findings [15], k^{ef} = 0.9 (0.85–1.0). Moreover, as shown in Fig. 3.3, a good agreement between the numerical solute analysis by directly solving Eq. 43) with the C^* and T^* values estimated by the model (long dashed line) and those predicted from the conventional heat analysis using the solidus temperature T^* estimated by the model (carbon concentration was estimated by Equation 1), thin solid line) was obtained. Thus, conventional heat analysis such as the equivalent specific heat method using the solidus temperature estimated by the model provides the solutions not only for the temperature but also for the solute concentrations. Thus, the present model is considered to simplify the extensive computations required to simultaneously solve the heat- and solute-transfer equations while searching the solidus temperature and the fraction solid as part of simultaneous solution.

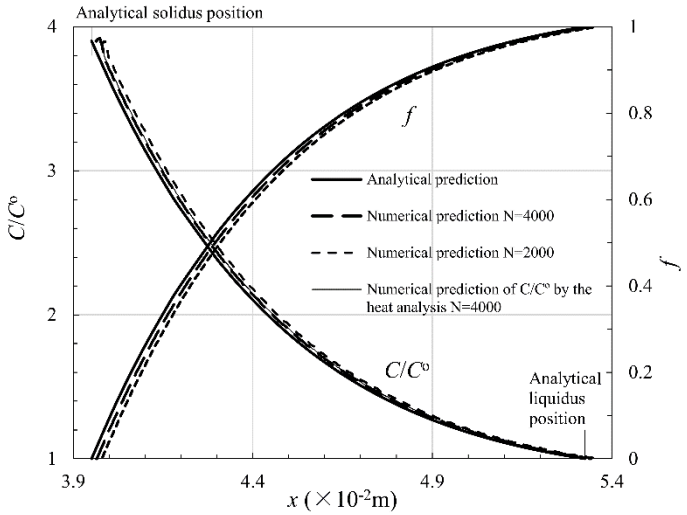

Fig. 3.3 Solute concentration C/C^o and liquid fraction predicted by the model and numerical analysis of a continuously cast steel. (0.15% C, T^s = 1423 K(1150 °C), ΔT = 15 K(15 °C), t = 240 s, slab thickness = 0.22 m, N = partitioning number of the half thickness of a slab).

3.3.4 Comparisons with Neumann's solution

The temperature transitions in the mushy zone predicted by the model and the Neumann's solution[24] for pure iron are shown in Fig. 3.4. Again, the surface temperature was kept at 1423 K (1150 °C) and the superheat of the initial temperature (ΔT) was 15 K (15 °C) for all cases. Accordingly, the initial temperature for the low carbon steels was higher than that of the high carbon steels to keep the same superheat (ΔT). As shown in Fig. 3.4, the temperature profile approached that of the Neumann's solution as the carbon concentration decreased. The changes in the solidification constants of the solidus and liquidus points with respect to the carbon concentration are shown in Fig. 3.5. The solidification constants of the solidus point increased and that of liquidus decreased while decreasing the carbon concentration. These values converged with the Neumann's solution for carbon concentration lower than 0.025%. The errors of the solidus temperature T^* in the process shown in Appendix 3.2 exceeded 0.1 K (0.1 °C) at carbon concentrations lower than 0.025%, and this should be considered the limitation to use the model. However, this convergence of the model predictions with the Neumann's solution [24] is indicative of a good consistency between the model and the Neumann's solution at low carbon range.

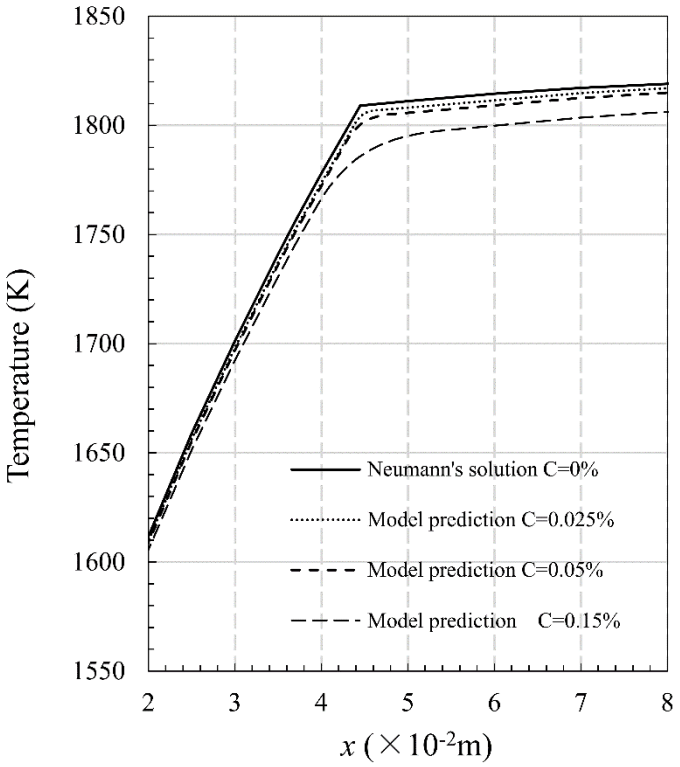

Fig. 3.4 Transitions of temperature predicted by the model and the Neumann' solution (C= 0%) of a continuously cast steel. (C=0%–0.15%, T^s = 1423 K (1150 °C), ΔT = 15 K (15 °C), t = 240 s, slab thickness = 0.22 m).

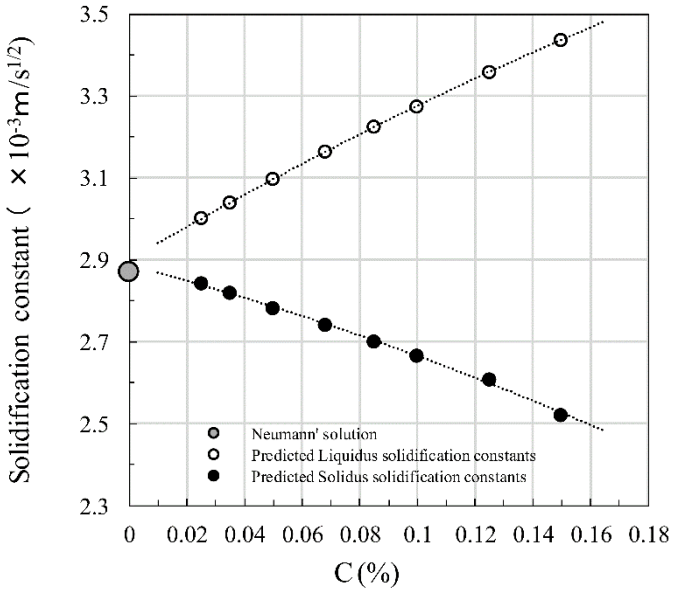

Fig. 3.5 Predicted liquidus and solidus solidification constants and the Neumann's solution of a continuously cast steel. (0.025%–0.15% C, T^{s} = 1423 K (1150 °C), ΔT = 15 K(15 °C),t = 240 s, slab thickness = 0.22 m).

3.3.5 Solidus Temperature

As shown earlier, the solidus temperature T^* was obtained by matching the three of Eqs. (3.67), (3.71), and (3.72) with a set of T^*, η_2^*, and η_2^{o}. However, this T^* can be explicitly given by Eq.(3.68) as follows:

$$T^* = T^{\circ} - \frac{L}{\dfrac{(2-\mathrm{k}-\alpha\mathrm{k})K_2}{2\rho_2(E-\alpha\mathrm{k}D)} - Cp_2} \tag{3.75}$$

The solidus temperature T^* estimated with (3.75) exactly matches with the set of solutions satisfying Eq.(3.67), (3.71), and (3.72). It should be noted that the inter-diffusion coefficient E for the liquid used in (3.75) is given by (3.68).

The evolution of the solidus temperature T^* and the estimated E as the physical properties changed by 1% are shown in Table 3.2. The estimated E value changes almost evenly with the heat conductivity K_2, while the influence of the carbon partition ratio k is prominent as compared with other independent physical properties. The solidus temperatures estimated with different carbon partition ratios k and those calculated with other reported formulas are shown in the Fe–C binary phase diagram (Fig. 3.6). The solidus temperatures estimated by the model are represented with solid lines while dotted lines correspond to the approximation errors of (Eq.3.57) exceeding 1% for the higher carbon concentration range. The solidus temperatures estimated by the model exist in the intermediate range between those calculated with formulas by Hirai et al. [3] and Suzuki et al. [4] and those calculated by Kawawa et al. [2] and Jablonka et al. [5] The

colored area seems to be reasonable because the effective partition ratio is larger than 0.85 as in the case of a real continuously cast steel (mostly close to 0.9) and the approximation errors remain lower than 1%. The solidus temperature predicted by the model is 10 and 20 K higher than that calculated with the Kawawa's formula [2] for a Fe-0.15%C steel when k = 0.19 and k = 0.225 are used, respectively.

Table 3.2 Effect of an increase of 1% in the parameters over T^* and E.

	ΔT^*(K)	ΔE (%)
K_2	−0.0072	1.02
ρ_2	−0.044	−0.86
Cp_2	−0.041	−0.2
L	−0.042	−0.93
k	4.161	−1.43

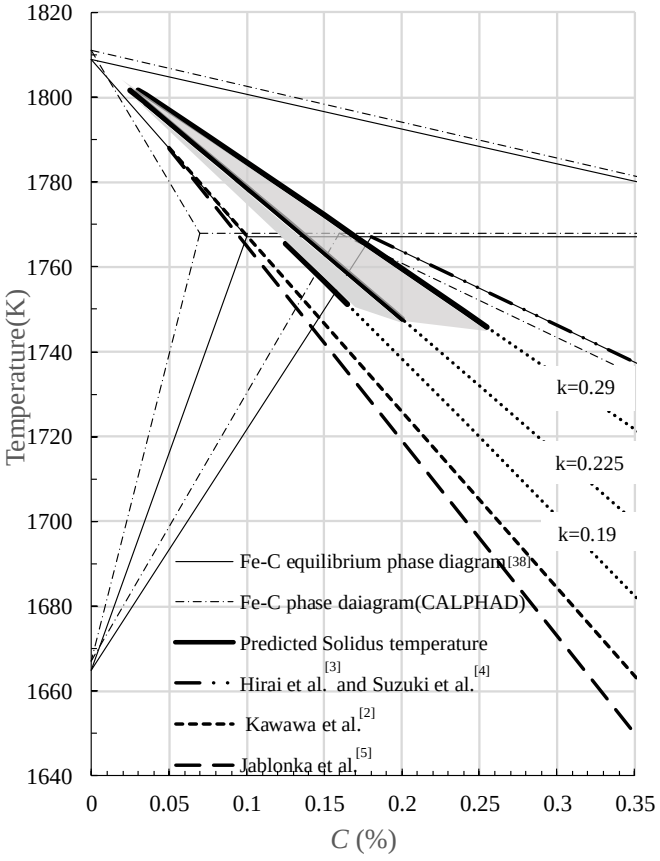

Fig. 3.6 Solidus temperature predicted by the model with different k values and the reported solidus temperature (phase diagram of a Fe–C binary system).

3.3.6 Applications of the Present Analytical Solutions to the Steel Casting Operations

To check the consistency between the model predictions and the actual values, the model predictions have been compared with the reported measurements by Kawawa et al. [1] adopting the shoot bullet technique for a continuously cast carbon steel (Fig. 3.7). The solidus positions were determined at the points where the bullets stuck with the steel shell. On the other hand, the points where the bullet fully melted and the composition became homogeneous with the molten bulk steel were defined as the liquidus positions (i.e., $fs = 0.2 - 0.6$).

It should be noted that the liquidus temperature of the present model (Fe–C binary alloy model) was corrected (5 K down) in accordance with the formula by Kawawa et al. [23] because of the effect of additional alloy components (i.e., 0.7% Mn and 0.22% Si). This approach for low-alloyed or low-carbon steels belonging to the Fe–C binary system was previously used by Fujimura et al. [22], and Esaka et al. [38]. The further decrease of the solidus temperature as a result of the enrichment of Mn and Si in the mushy zone estimated to be 3.3 K (3.3 °C) according to the previous model for a multi-component alloy system (a 2.8 K (2.8 °C) decrease was expected according to the formula by Esaka et al.[38] was neglected because it is low as compared to that produced by carbon enrichment (the error of solidus point, the 240 s after the solidification started was estimated to be 2×10^{-4} m). The estimated k^{ef} value for carbon ($k^{ef} = 0.9$) was in good agreement with generally accepted values. As shown in Fig. 3.7, good agreements between the measured and the estimated liquidus (f_s = 0.2–0.6) and solidus lines were also obtained.

The changes in important parameters predicted by the model for a 0.15%C steel with respect to the surface temperature are shown in Fig. 3.8. The effective partition ratio and the solidus temperature remained nearly constant. The solidification constants of the solidus and liquidus points slightly increased with the decrease of surface temperature. Thus, increasing the shell thickness by intensive cooling is not easy and can possibly result in an increase of surface defects in cast steel as a result of intensified non-uniform water spray cooling. Thus, it is easy to study the operational actions and results with the model proposed herein. The validation of α that represents the homogeneity of the carbon concentration in the solid within a mushy zone along the dendrite radius direction was made as follows:

The numerical analysis regarding to the carbon redistribution by diffusion in the solid was made (Appendix 3.3). It was assumed that a cylindrical dendrite sequentially grew up to 500 μm in diameter according to f_s and the carbon concentration at the solid/liquid interface changed according to the model predictions. The total solidification time from the beginning until the end of the solidification process was

213 s. The carbon diffusion coefficient in the solid used in the calculation was $D = 6.6 \times 10^{-10}$ m^2/s [39]. The carbon concentration in the solid mostly followed the enrichment of carbon in residual liquid, although a small diffusion delay in the central region was observed after the middle stage of solidification. However, the final averaged carbon concentration in the dendrite reached 97%. Thus, it is considered that α remained close to 1 during solidification.

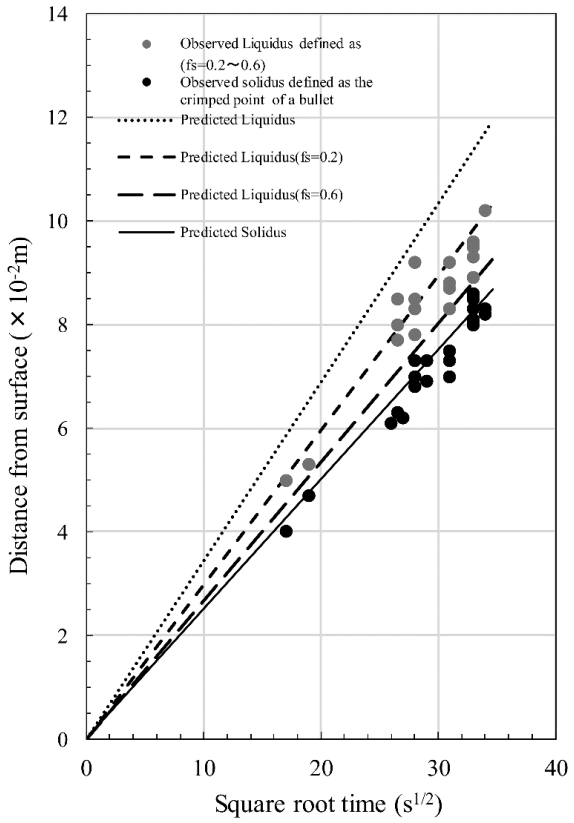

Fig. 3.7 Measured and estimated liquidus and solidus positions in a continuously cast steel as measured by the shoot bullet technique [1] and the model predictions (the observed liquidus positions are defined as *f*s = 0.2–0.6. Steel composition 0.15%C, 0.22% Si, and 0.70% Mn).

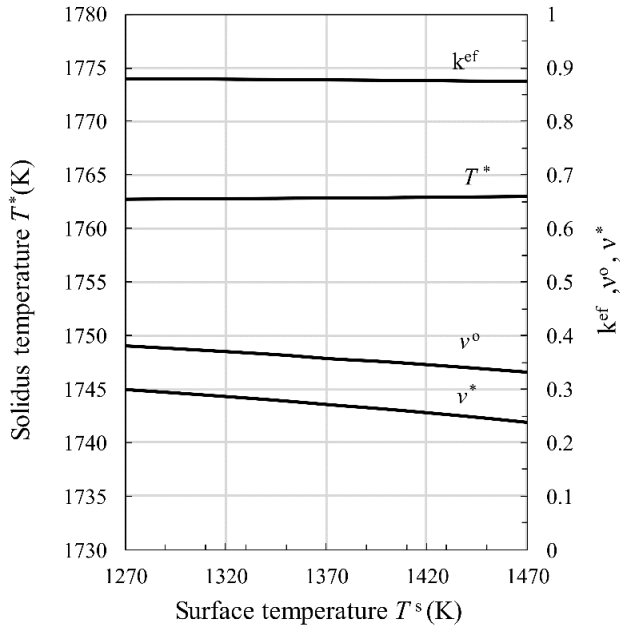

Fig. 3.8 Influence of the surface temperature T^s on the solidus temperature T^*, the effective partition ratio k^{ef} and the solidification constants $\nu^*$and ν^o. (0.15% C, k = 0.225, and the others properties are listed in Table 3.1).

3.4 Conclusions of this Chapter

The solidus temperature, parameters directly related to the solidification constants of the solidus and the liquidus points were obtained as a part of the solutions of the nonlinear heat- and solute-transfer equations assuming a linear relationship between the solid fraction and the temperature. As a result, an estimation of the temperature profile and solute concentration in the mushy zone with the overall temperature profiles in the solid and liquid is easily obtained. The model predictions were in good agreements with generally accepted values for a continuously cast steel. The solidification constants were also in the range of those of continuously cast carbon steels. Furthermore, the predicted solidus temperature lied in the intermediate temperature range between the values calculated with formulas by Hirai et al. and Suzuki et al. and those estimated by Kawawa et al. and Jablonka et al.

The analytical solutions of the model were in good agreement with the numerical analysis, and showed good consistency with the Neumann's solution at low carbon ranges. It should be noted that conventional heat analyses (e.g., the equivalent specific heat method), with the solidus temperature predicted by this model, provide the temperature and the solute concentration in the mushy zone with respect to time. The model simplifies the extensive computation to simultaneously solve the heat- and solute-transfer equations while searching for the solidus temperature and the fraction solid as part of simultaneous solutions. This model would

be beneficial for simplifying the complicated analysis considering the heat- and solute-transfer phenomena in the mushy zone.

Appendix 3.1

The error of the approximation of the erf(η) is kept smaller than 0.2% for η > 1.73, as shown in Fig.9.

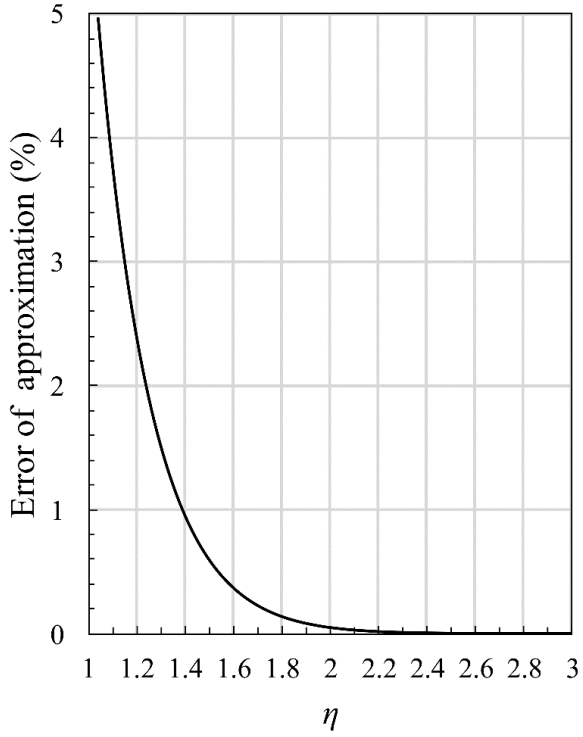

Fig. 3.9 Error of approximation for the erf(η) used in the model.

Appendix 3.2

The unknown variables, important physical properties are shown in Table 3.3. The typical carbon partition ratio k in the δ phase (a wide range of values is reported) is used. The left and right sides of Eqs.(3.71) and (3.72) are denoted as A, B, and C (B is commonly used). The unknown parameters minimizing the aimed function Z defined as follows were sought:

$$Z=(1-A/B)^2 + (1-C/B)^2$$

$$A = \frac{K_1(T^* - T^s)\exp\{(1-\frac{\beta_2}{\beta_1})\eta_2^{*2}\}}{(T^* - T^o)\,\mathrm{erf}(\sqrt{\frac{\beta_2}{\beta_1}}\eta_2^*)\sqrt{\beta_1}}$$

$$B = \frac{K_2}{\{\mathrm{erf}(\eta_2^*) - \mathrm{erf}(\eta_2^o)\}\sqrt{\beta_2}}$$

$$C = \frac{K_3(T^i - T^o)\exp\{(1-\frac{\beta_2}{\beta_3})\eta_2^{o2}\}}{(T^* - T^o)\{1-\mathrm{erf}(\sqrt{\frac{\beta_2}{\beta_3}}\eta_2^o)\}\sqrt{\beta_3}}$$

$$D: \frac{\{1-\mathrm{erf}(\eta_2^\circ)\}}{\{\mathrm{erf}(\eta_2^*)-\mathrm{erf}(\eta_2^\circ)\}} = \frac{2(1-k)}{(2-k-\alpha k)}\lambda C^\circ + \frac{(1+\alpha)k}{(2-k-\alpha k)} - \frac{\alpha k D}{E-\alpha k D}$$

(1) First, the initial values for T^*, η^*, and η^o are given. The T^* calculated with the reported formula is used as the initial value for T^*. The initial η^o was 1.0. The η^* was given as $\eta^* = \gamma\,\eta^o$ where the initial $\gamma = 0.3$.

(2) Second, the η^o is changed to minimize Z for the initial T^*. Convergence is quickly obtained.

(3) Next, η^* minimizing Z is obtained by changing γ ($\eta^* = \gamma\,\eta^o$).

(4) Substituting η^*, η^o obtained by the above process to the left side of Eq.(3.67) provides λ (used in the right side of the Eq.(3. 67), (D: shown above). Substituting this λ into Eq.(3.9), yields the new T^*. Using this T^* as the initial T^* and repeating the same process mentioned above (2) to (4) yields the set of (T^*, η^*, and η^o) as the three Eqs.(3.67), (3.71), and (3.72) match.

(5) This process is repeated until Z < 0.1, and the four decimal digits does not change in the present analysis.

Table 3.3 Unknown variables and physical properties used in the model and the equations to determine unknown properties

T^*	Solidus Temp.	●
η_2^*	η for solidus point in mushy zone	●
η_2^o	η for liquidus point in mushy zone	●
T^o	Liquidus temp.	○
T^i	Initial Temp.	○
T^s	Surface Temp.	○
C°	Solute concentration in bulk liquid	○
K_1, K_2, K_3	Thermal conductivity reported value	○
Cp_1,Cp_2,Cp_3	Specific heat reported value	○
m	Temperature gradient of the liquidus line	○
k	Partition ratio of solute	◎

β_1 , β_3	Thermal properties defined by eq. 26),28)	○
β_2	Thermal properties defined by eq. 27)	△
λ,S	parameter determined by eq. 62),63)	△
E	Interdiffusion coefficient in liquid estimated by eq. 61)	△
D	Interdiffusion coefficient in solid	○

● unknown properties

◎ known property with wide variety

○ known values or properties

△ properties obtained by T *, η_2*, η_2^o

Appendix 3.3

The carbon concentration in a cylindrical dendrite becomes almost homogeneous at the end of solidification due to the rapid diffusion, as shown in Fig. 3.10.

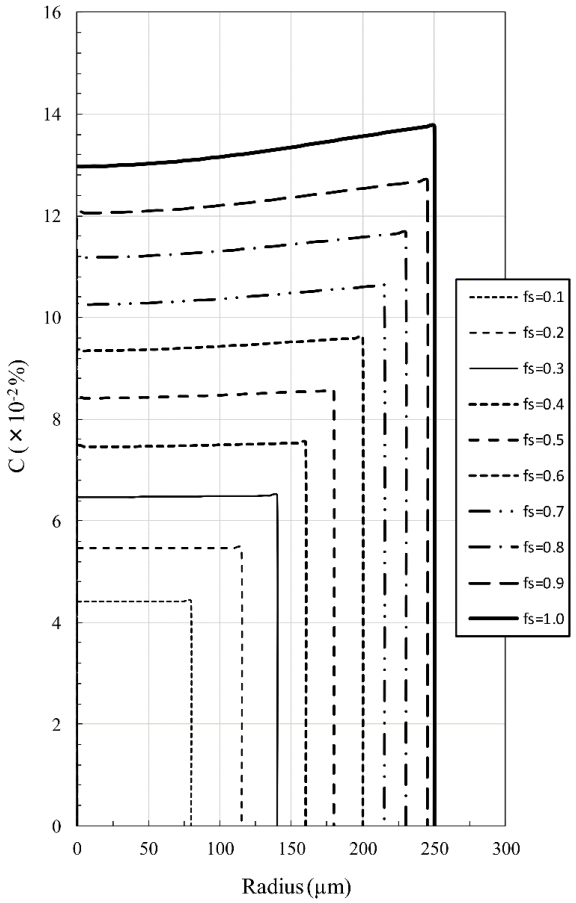

Fig. 3.10 Transition of C in the solid during the growth of a dendrite. C in the liquid was increased according to the model predictions. (C^o/0.15%, C_s^*/0.138%, $D = 6.6 \times 10^{-10}$ m^2/s, solidification time = 213 s, dendrite diameter = 500 μm).

References

[1] T. Kawawa, H. Sato, S. Miyahara, T. Koyano and H. Nemoto, Determination of Solidifying Shell Thickness of Continuously Cast Slab by Rivet Pin Shooting, Tetsu-to-Hagane 60 (1974) 206–216.

[2] T. Kawawa and H. Tuchida, Tekko-no-Gyouko (Solidification of steel), Appendix 4, ed. By Solidification Comm., Joint Sc. on Iron and Steel Basic Research of ISIJ, ISIJ, Tokyo, 1977.

[3] M. Hirai, K. Kanamaru and H. Mori, Tekko-no-Gyouko (Solidification of steel), Appendix 4, ed. By Solidification Comm., Joint Sc. on Iron and Steel Basic Research of ISIJ, ISIJ, Tokyo, 1977.

[4] A. Suzuki, T. Suzuki, Y. Nagaoka and Y. Iwata, On Secondary Dendrite Arm Spacing in Commercial Steels Having Different Carbon Contents, J. Jpn. Inst. Met. 32 (1968) 1301–1305.

[5] A. Jablonka, K. Harste, and K. Schwerdfeger, Steel Res., 62 (1991) 24-33.

[6] K. Gryc, B. Smetana, M. Zaludova, K. Michalek, P. Klus, M. Tkadleckova, L, Socha, J. Dobrovska, P. Machovcak, L. Valek, R. Pachlopnik and B. Chmiel, Determination of the Solidus and Liquidus Temperatures of the Real-Steel Grades with Dynamic Thermal-Analysis Methods, Mater. Technol. 47 (2013) 569–575.

[7] E. A. Mizikar, Mathematical Heat Transfer Model for Solidification of Continuously Cast Steel Slabs, Trans. AIME, 239 (1967) 1747-1753.

[8] J. Szekely and V. Stanek, On Heat Transfer and Liquid Mixing in the Continuous Casting of Steel, Metall. Trans. 1 (1970) 119–126.

[9] J. Matsuno, H. Nakato and H. Ohi, An analysis of Solidification Rate and Surface Temperature of Continuous Casting Slabs, Tetsu-to-Hagane 60 (1974) 1023–1032.

[10] Y. K. Chuang and K. Schwerdfeger, Arch. Eisenhüttenwes. 44 (1973) 341-347.

[11] P.H. Shingu, K. Takeshita, R. Ozaki and T. Akiyama, An analysis of the Solidification of a Binary Eutectic System Considering Temperature and Solute Distribution, J. Jpn. Inst. Met. 42 (1978) 172–179.

[12] H.D. Brody and M.C. Flemings, Solute Redistribution during Dendritic Solidification, Trans. Met.

Soc. AIME 236 (1966) 615–624.

[13] T.W. Clyne and W. Kurz, Solute Redistribution during Solidification with Rapid Solid State Diffusion, Met. Trans. 12A (1981) 965–971.

[14] I. Ohnaka and T. Fukusako, Calculation of Solidification of Castings by a Matrix Method, Trans. Iron Steel Inst. Jpn. 17 (1977) 410–418.

[15] K. Kumai, A. Sano, T. Ohashi, E. Nomura and H. Fujii, Study on Solidification Behavior, Solute Segregation and Fluid Flow in Continuously Cast Slab, Tetsu-to-Hagane 7 (1974) 894–914.

[16] S. Asai and I. Muchi, Analysis of Effective Distribution Coefficient Based of Transport Phenomena in Liquid and Solid Region, Tetsu du-to-Hagane 64 (1978) 1685–1692.

[17] R.N. Hills, D.E. Looper and P.H. Roberts, A Thermodynamically Consistent Model of a Mushy Zone, Q. J. Mech. Appl. Math. 36 (1983) 505–539.

[18] D.V. Alexandrov, Solidification with a Quasi-Equilibrium Mushy Region: Exact Analytical Solution of Nonlinear Model, J. Crystal Growth 222 (2001) 816–821.

[19] K. Takeshita, An Analysis of the Solidification of a Binary Eutectic System in Consideration of Both Heat and Solute Diffusion, J. Jpn. Inst. Met. 47 (1983) 647–653.

[20] H.E. Huppert and M.G. Worster, Dynamic Solidification of a Binary Melt, Nature 314 (1985) 703–707.

[21] D.V. Alexandrov and V.P. Malygin, Self-Similar Solidification of an Alloy from a Cooled Boundary, Int. J. Heat Mass. Transf. 49 (2006) 763–769.

[22] T. Fujimura and J.K. Brimacombe, Mathematical Analysis of Solidification Behavior of Multicomponent Alloys, Trans. Iron Steel Inst. Jpn. 26 (1986) 532–539.

[23] T. Kawawa, Tekko-no-Gyouko (Solidification of steel), Appendix 4, ed. By Solidification Comm., Joint Sc. on Iron and Steel Basic Research of ISIJ, ISIJ, Tokyo, 1977.

[24] H.S. Carslaw and J.G. Jaeger, Conduction of Heat in Solids, 2nd ed., Oxford University Press, New York, Tronto, Tokyo, 1959, 283–291.

[25] T. Mitsuo, T. Horigome, S. Saito, E. Nomura, Y. Kitamura and R. Kohno, On the Accumulation Mechanism and the Reducing Process of Large Non-Metallic Inclusions in the Bottom Equiaxed Zone of Ingots, Tetsu-to-Hagane 57 (1971) 915-941.

[26] M. C. Flemings and G. E. Nero, *Trans.* Met. Soc. AIME, 239 (1967) 1449-1461.

[27] H. Nomura, T. Tarutani and K. Mori, Mathematical Model of Formation of Segregation Zone Caused by Volume Change in Solidification of Iron Alloys, Tetsu-to-Hagane 67(1981) 80-87.

[28] K. Miyazawa, *STA*, vol. 2 (2001) 59-65.

[29] K. Harste, Investigation of the Shrinkage and the Origin of Mechanical Tension Solidification and Successive Cooling of Cylindrical Bars of Fe-C alloys, PhD. Dissertation, Universität Clausthal,1989

[30] Y.A. Meng and B.G. Thomas, Heat-Transfer and Solidification Model of Continuous Slab Casting: CON1D, Metall. Mate. Trans. B34 (2003) 685–705.

[31] A. Hays and J. Chipman, Mechanism of Solidification and Segregation in a Low-Carbon Rimming - Steel Ingot, Trans. Met. Soc. AIME 135 (1938) 85.

[32] W.A. Fisher, H. Splizer and M. Hishinuma, Das Zonenschmelzen von Eisen und die Ermittlung der Verteilungskoeffizienten für Kohlenstoff, Phosphor, Schwefel und Sauerstoff, Arch. Eisenhüttenwes. 31 (1960) 365–371.

[33] C. E. Sims, Electric Furnace Steelmaking, vol. 2, John Wiley & Sons, 1962, p. 99.

[34] W.A. Tiller, Solute Segregation during Ingot Solidification, J. Iron Steel Inst. 192 (1959) 338–350.

[35] K. Katayama and S. Hattori, *Trans. JSME* 40 (1974) 1404-1411.

[36] R. A. Buckley and W. Hume-Rothery, J. Iron Steel Inst. 196 (1960) 403-406.

[37] R.E. Grace and G. Derge, Diffusion of Third Elements in Liquid Iron Saturated with Carbon, Trans. Metall. Soc. AIME 212 (1958) 313–337.

[38] R. Tanaka, On the Recent Iron-Carbon Equilibrium Diagram, Tetsu-to-Hagane 53 (1967) 1586-1604.

[39] H. Esaka and S. Ogibayashi, Estimation of Primary Dendrite Arm Spacing and Solidified Interface Morphology in Low Carbon Steel by Introducing Quasi Fe-C Binary Alloy, Tetsu-to-Hagane 84 (1998) 49-54.

[40] D.F. Kalinovich, I.I. Kovenskii and M.D. Smolin, Carbon State in Austenite with 0, 4 and 0, 6 Weight Percent Content of C, Izv. Vyssh. Ucheb. Zaved., Fiz. 9 (1971) 116.

Chapter 4

Model III

Mathematical Analysis of the Solidification Behavior of Multi-Component Alloy Steel Based on Heat- and Solute-Transfer Equations in the Liquid–Solid Zone

Abstract

An approximate analytical model has been developed to obtain simultaneous solutions for nonlinear solute- and heat-transfer equations for multi-component alloy steels; in this model, a linear relation between the solid fraction and the temperature in the mushy zone was assumed. This model predicts important parameters, such as the solidus temperature for the multi-component steel materials that have not been well confirmed by the reliable measurement in a real process. The predicted temperature, solidification constants, and effective partition ratios of solutes were in good agreement with both the reported measurements and generally accepted values. The predicted solidus temperatures were also in reasonable agreement with the reported zero ductile temperature of Fe–C–Mn steel and the thermo-analytically measured solidus temperatures of steels of various grades. The solutions were also in good agreement with those separately performed numerical thermal analysis. The model involves the solution for Fe-C binary alloy which is consistent with the Neumann's solution in the low carbon range. Thus, this model provides approximate analytical solutions that can reduce the computational load, saving time and cost.

4.1 Introduction

Numerical methods are effectively used to simulate heat-transfer phenomena during solidification processes. While these methods provide reliable surface temperatures (*i.e.*, those calibrated with the measured values), inner temperatures are not generally confirmed with the actual (measured) values. In particular, the solidus points were hardly checked by measurements with the associated solidus temperature.

The main reason for these problems lies in the difficulty [1] of achieving reliable measurements of the solidus temperature of general steel. In addition, the fraction of solid in a solid–liquid coexisting zone (*i.e.*, mushy zone) remains unclarified. According to Crepau et al. [2], the morphology of a mushy zone is difficult to predict

and no analytic solutions are known to exist that describe the relation between the size of a mushy zone and volumetric heat generation.

With respect to the liquidus temperature, while it is not also generally measured during the casting process, the problems are not serious because microsegregation at the dendrite tips is so small that super-cooling is limited to only a few degrees. Therefore, the liquidus temperature for general steel can be estimated from the phase diagram or from measurements, which are in reasonable agreement with each other. However, with regard to the solidus temperature of steel, significant discrepancies exist among the estimates based on the phase diagram and models accounting for microsegregation. (*i.e.*, 40 K discrepancies [3–5]). Recently, Gryc et al. [6] thermo-analytically measured the solidus temperature for various steel grades and reported significant discrepancies between the measurements and the values obtained from the reported formulas (up to 42 K) or thermodynamic calculations (up to 50 K). These discrepancies could lead to considerable errors in estimating the position at which the shell develops with a target thickness.

The lack of knowledge about the fraction of solid in the mushy zone has spurred the onset of numerous methods based on heat analysis. They can be classified into three major models (A)–(C): (A) methods [7–9] assuming a linear relationship between the solid fraction and the temperature (*e.g.*, equivalent specific heat model); (B) methods [10,11] based on the equilibrium lever rule, the Scheil equation, and back diffusion models [12–16]; (C) methods [17] recovering the temperature with the latent heat release after solidification. However, these methods are not always consistent with the real solidification process. For example, (C) methods assume that the primary dendrites should grow after solidification. When the (B) methods such as Scheil equation with a large domain are used along the dendrite axial direction, a flat boundary surface should be assumed for the dendritic mushy zone. The diffusions of solutes in liquid along the dendrite axial direction are neglected ,although the effective partition ratios of solutes are generally less than 1.0 [18]. Thus, the fraction of solid used in the thermal analysis should be consistent with general solidification.

Instead of a large domain, for the (B) methods with a small scale of domain, as small as a secondary arm spacing, the microsegregation in the dendritic mushy zone can be analytically evaluated assuming a constant cooling rate with the uniform temperature in a domain and neglecting the diffusion along the primary dendrite axis direction. The lever rule assumes the complete diffusion in both liquid and solid, while Scheil's equation assumes no diffusion of solutes in solid and complete diffusion in liquid, which are considered to be two significant limitations for microsegregation predictions (*i.e.*, infinite diffusion and negligible diffusion in solid). Because this small domain is considered to be blockaded by secondary arms as soon as secondary arms develop. Brody and Flemings [12] developed a model to consider the back diffusion of solutes in solid with the

assumption of finite diffusion in solid and complete diffusion in liquid. Clyne and Kurz [13] treated the Brody and Flemings model in a mathematical way that allowed the model approach the lever rule and Scheil's model for infinite and negligible diffusion in a solid, respectively. Ohnaka [14] considered a columnar dendrite rather than the plate dendrite and derived the model through solving the overall mass balance. Voller and Beckermann [15] also proposed a model that considered the coarsening of secondary arms. These models are effectively used to investigate the microsegregation of numerous alloys. However, the cooling rate considerably varies during solidification and the assumption of the constant cooling rate make it difficult to incorporate the heat-transfer equation for the general steel in these models.

To resolve the issue, an enlarged domain as large as a primary dendrite arm divided into small volume elements is considered. This enlarged domain involves the continuum liquid, which allows the diffusion of the solutes along the primary dendrite axis direction (solidification direction). It should be noted that taking account of diffusion in liquid, which is much larger (generally two order magnitude larger) than that in solid, composes the limitation at the end of solidification and makes it easier to incorporate the heat transfer along the solidification direction in the diffusion model. Considering the large domain wherein both solute and heat are transferred along the primary dendrite axis direction (solidification direction), Asai and Muchi [19], Hills and Looper [20], and Alexandrov [21] obtained analytical or approximate analytical solutions for the solute- and heat-transfer simultaneous equations under a steady-state conditions (*i.e.*, constant solidification velocity). However, these analytical solutions cannot be directly used for general heat analysis because the solidification velocity significantly changes with time.

Regarding the unsteady state solidification, Takeshita [22] obtained simultaneous solutions for unsteady state solidification using an extensive numerical computation model for a NH_4Cl aqueous eutectic system (a binary system); in advance of the numerical computation, the model analytically eliminated the solid fraction-related terms in the equations in the case of negligible solute diffusion in a solid. However, to use this model for multi-component alloy steel, more complicated computations are required. Huppert and Worster [23] and Alexandrov and Malygin [24] proposed models for aqueous chimney-type unsteady state solidifications (a binary system); their models, however, focused on particular scenarios, such as if a liquidus point develops, whereas the solidus point barely develops. This limits the applicability of their models for the solidification of steel, because the solidus point of the general steel typically develops along with an associated liquidus point during solidification. Fujimura and Brimacombe [25] obtained approximate analytical solutions to nonlinear heat- and solute-transfer equations for a case where the solidification front develops with the square root of time by considering the diffusion of the solutes along the solidification direction. The solutions thus obtained were in good

agreement with the reported measurements. These solutions, however, were obtained by assigning the measured solidification constants as boundary conditions rather than by using the conditions generally adopted in conventional heat analyses; consequently, the accuracy of the predictions made by that model strongly depends on the measured solidification constants, and the analyses are not fully consistent with the conventional heat analyses because of the insufficient boundary conditions.

In that direction, Fujimura et al. [26] recently proposed an approximate analytical model for the heat- and solute-transfer equations for Fe–C binary plain steel by considering the boundary conditions that are generally used in heat analyses (*i.e.*, the measured solidification constants were not used). The solutions were in good agreement with the numerical analysis that was performed separately. Furthermore, they were consistent with Neumann's solution [27] in the low carbon range.

However, the applicability of this model is limited to carbon plain steel. Expanding the model's applicability to the general steel, the solidus temperature of the general steel is pursued in the present study. The model predictions and the solidus temperatures of the multi-component alloy steel obtained as the part of the approximate analytical solution are compared with the numerical analysis and the reported measurements. In the present model, the solidification at the middle stage between the early stage and the end stage is investigated.

4.2 Governing Equations of Solidification

4.2.1 Basic Assumptions

The solidification problems mathematically modeled are schematically shown in Fig. 4.1. The volume element in a domain, which is as large as a primary dendrite, is considered wherein the representative fraction solid is defined as the total fraction solid of both a primary dendrite and a secondary arm (a shaded area in Fig. 4.1). Heat is unidirectionally extracted and a solid shell is considered to grow from the surface. In the mushy zone, heat and solute are considered to transfer by conduction and diffusion, respectively. The main assumptions made in the model, which are consistent with the previous model [25,26], are as follows:

(1) Heat is exclusively extracted by heat conduction along the solidification direction (primary dendrite axis direction, *i.e.*, x axis).

(2) The density and specific heat of the liquid are the same as those of the solid in a mushy zone.

(3) The solute is exclusively transported by diffusion via moderate fluid flow in a mushy zone.

(4) The effect of the dendrite tip curvature on the liquidus temperature is negligible.

(5) Undercooling within the mushy zone is negligible.

(6) The diffusion of the solute, carbon, in the liquid within a mushy zone is sufficiently rapid to achieve a homogeneous composition in the direction normal to that of the solidification direction (*i.e.*, primary dendrite radial direction) over a distance in the order of the primary dendrite arm spacing (generally, the magnitude of the primary dendrite arm spacing in continuously cast steels is in the range of 50–500 μm except in the chill zone).

(7) Local equilibrium between the liquid and the solid surfaces in a volume element is achieved (This assumption was also considered by Asai and Muchi [19], Takeshita [22], Huppert and Worster [23] and Fujimura and Brimacombe [25] and Fujimura et al. [26].

(8) As considered in a conventional heat analysis, the fraction of solid in the mushy zone is assumed to be linear to the temperature.

It should be noted that the present model does not discriminate between the primary dendrites and the secondary arms as the solid in a mushy zone. Therefore, the precise micro-segregations between the secondary arms are not considered in the present model.

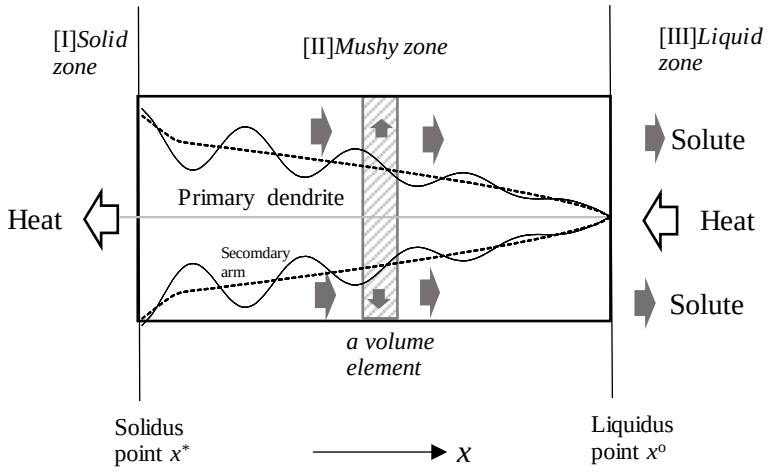

Fig. 4.1 Schematic of the solidification problem studied in the model.

4.2.2 Mathematical Formulations

The preconditions and assumptions made in the model are as follows, which correspond to three zones,

[I] solid zone, [II] mushy zone, and [III] liquid zone. In [II] mushy zone, the mathematical process for the multi-component solutes developed in the multi-component alloy model [25] is used to expand the binary model [26] to the multi-component system model. (Some of the equations refer to Appendix 4.A to 4.D.)

[I] zone

(I-1) The liquid initially held at T^i is instantaneously kept at T^s at the surface (x = 0) and solidification begins.

(I-2) This T^s is assumed to be the temperature that results the same amount of heat extraction from the surface with the real continuous casting (Appendix 4.D).

(I-3) The temperature of the boundary (I/ II), solidus temperature T^* is kept constant.

[II] zone

(II-1) The liquidus temperature is coupled with the dilute solute concentrations by the liquidus lines of the phase diagram that can be represented by the following equation, as proposed by Kawawa et al. [28]:

$$T = T_M + \sum_i m_i C_i \tag{4.1}$$

T_M : Solidus temperature of pure liquid (K)

m_i : Temperature gradient of the liquidus line with respect to the concentration of i (K/%)

C_i : Concentration (%) of solute i in the liquid

(II-2) The liquid fraction f is assumed to be linear to the temperature T in a mushy zone as follows:

$$f = \frac{T - T^*}{T^\circ - T^*} \tag{4.2}$$

f : Liquid fraction

T : Temperature (K)

T° : Liquidus temperature (K)

T^* : Solidus Temperature (K)

(II-3) The linear relationship between the liquid fraction and the concentration of each solute is obtained for the binary system adopting Eq. (4.1) to Eq. (4.2), and then Eq. (4.3) is obtained if the negligible solute-solute interaction is assumed [25]. (the reported measurement [29], which showed the similarities between the concentration profile of each solute against the solid fraction in a mushy zone, partially supports this assumption).

$$f = \lambda_i C_i + s_i = \lambda_j C_j + s_j \tag{4.3}$$

$\lambda_i, \lambda_j, s_i, s_j$: unknown constants

(II-4) $T = T^*, C = C_i^*$ are constant at I/II boundary (x = x^* solidus point).

C_i^* : Concentration of the solute i at the solidus point

(II-5) $T = T^{\circ}, C = C_i^{\circ}$ *a*re constant at II/III boundary ($x =$ x° liquidus point).

C_i° : Concentration of the solute *i* at the liquidus point

[III] zone

(III-1) The liquid initially held with T^i remains in the central region (as will be discussed in 4.4.2.1), the numerical analysis showed that this assumption is practically reasonable).

The density, the specific heat, and the thermal conductivity of each zone are denoted as $\rho_i, \mathrm{Cp}_i, \mathrm{K}_i$ (i represents the zone), while L represents the latent heat. The heat balance equations are as follows:

[I] zone

$$\rho_1 Cp_1 \frac{\partial T}{\partial t} = K_1 \frac{\partial^2 T}{\partial x^2} \tag{4.4}$$

$$x = 0 \quad : T = T^s \tag{4.5}$$

$$x = x^* \ : T = T^* \tag{4.6}$$

T^s : Surface Temperature (K)

[II] zone

$$\rho_2 Cp_2 \frac{\partial T}{\partial t} + \rho_2 L \frac{\partial f}{\partial t} = K_2 \frac{\partial^2 T}{\partial x^2} \tag{4.7}$$

$$x = x^* \ : T = T^* \tag{4.8}$$

$$x = x^{\circ} \ : T = T^{\circ} \tag{4.9}$$

By substituting Eq. (4.2) into Eq. (4.7), we obtain

$$\left\{\rho_2 Cp_2 + \rho_2 L/(T^{\circ} - T^*)\right\} \frac{\partial T}{\partial t} = K_2 \frac{\partial^2 T}{\partial x^2} \tag{4.10}$$

The following equation is obtained by Eq. (4.3).

$$C_j = \frac{\lambda_i}{\lambda_j} C_i + \frac{\mathrm{s}_i - \mathrm{s}_j}{\lambda_j} \tag{4.11}$$

Eq.(4.1),(4.3) and (4.11) yields Eq.(4.12), (Appendix 4.A)

$$T^* = T^{\circ} - \sum_i \frac{\mathrm{m}_i}{\lambda_i} \tag{4.12}$$

[III] zone

$$\rho_3 Cp_3 \frac{\partial T}{\partial t} = K_3 \frac{\partial^2 T}{\partial x^2} \tag{4.13}$$

$$t = 0 \quad : T = T^i \tag{4.14}$$

$$x = x^{\circ} \ : T = T^{\circ} \tag{4.15}$$

At the center, the following equation is given by the assumption (III-1):

$$x = x^c \quad : T = T^c \approx T^i \tag{4.16}$$

These equations are transformed with the following similarity variables [22,25–27] defined as Eqs. (4.17), (4.18), and (4.19). We denote the upper right suffix as the solute *i* and the lower right suffix as zone [I], [II], and [III].

$$\eta_1^i = \frac{x}{2\sqrt{\beta_1^i t}} \tag{4.17}$$

$$\eta_2^i = \frac{x}{2\sqrt{\beta_2^i t}} \tag{4.18}$$

$$\eta_3^i = \frac{x}{2\sqrt{\beta_3^i t}} \tag{4.19}$$

$$\beta_1^i = \frac{K_1}{\rho_1 Cp_1} \tag{4.20}$$

$$\beta_2^i = \frac{K_2}{\rho_2 Cp_2 + \dfrac{\rho_2 L}{(T^\circ - T^*)}} \tag{4.21}$$

$$\beta_3^i = \frac{K_3}{\rho_3 Cp_3} \tag{4.22}$$

It is obvious that $\beta_1^i, \beta_2^i, \beta_3^i$ and $\eta_1^i, \eta_2^i, \eta_3^i$ are independent on the solute types, as shown in Eqs. (4.17)–(4.22). Hence, the upper suffix *i* is omitted and denoted as $\beta_1, \beta_2, \beta_3$ and η_1, η_2, η_3. The following ordinary differential equations and solutions are obtained as follows:

[I] zone

$$-2\eta_1 \frac{\mathrm{d}T}{\mathrm{d}\eta_1} = \frac{\mathrm{d}^2 T}{\mathrm{d}\eta_1^2} \tag{4.23}$$

$$x = 0 \quad , \ \eta_1 = 0 \qquad : T = T^s \tag{4.24}$$

$$x = x^* \ , \ \eta_1 = \eta_1^* \quad : T = T^* \tag{4.25}$$

$$T = \frac{(T^* - T^s)}{\mathrm{erf}(\eta_1^*)} \mathrm{erf}(\eta_1) + T^s \tag{4.26}$$

[II] zone

$$-2\eta_2 \frac{\mathrm{d}T}{\mathrm{d}\eta_2} = \frac{\mathrm{d}^2 T}{\mathrm{d}\eta_2^2} \tag{4.27}$$

$$x = x^* \ , \ \eta_2 = \eta_2^* \quad : T = T^* \tag{4.28}$$

$$x = x^\circ \ , \ \eta_2 = \eta_2^\circ \quad : T = T^\circ \tag{4.29}$$

$$T = \frac{(T^* - T^\circ)\left\{\mathrm{erf}(\eta_2) - \mathrm{erf}(\eta_2^\circ)\right\}}{\left\{\mathrm{erf}(\eta_2^*) - \mathrm{erf}(\eta_2^\circ)\right\}} + T^\circ \tag{4.30}$$

[III] zone

$$-2\eta_3 \frac{\mathrm{d}T}{\mathrm{d}\eta_3} = \frac{\mathrm{d}^2 T}{\mathrm{d}\eta_3^{\,2}} \tag{4.31}$$

$$t = 0 \ , \ \eta_3 = \infty \quad : T = T^i \tag{4.32}$$

$$x = x^\circ \ , \ \eta_3 = \eta_3^\circ \quad : T = T^\circ \tag{4.33}$$

$$x = x^c \ , \ \eta_3 = \eta_3^c \quad : T = T^c \approx T^i \tag{4.34}$$

$$T = \frac{(T^\circ - T^i)\{1 - \mathrm{erf}(\eta_3)\}}{\{1 - \mathrm{erf}(\eta_3^\circ)\}} + T^i \tag{4.35}$$

Where $T^c(\eta_3^c) \approx T^i$ as assumed in Eq. (4.16), assumption (III-1).

The Neumann's boundary condition [27] is required if a mushy zone does not exist. However, the boundary conditions generally adopted in the conventional heat analysis are used in the present case wherein a mushy zone was found to have developed, as generally used in the numerical analysis. It is noted that the latent heat generation in the mushy zone is taken into account in Eq.(4.36) and Eq.(4.37).

$$-K_1 \left.\frac{\partial T}{\partial x}\right|_{x^*} + K_2 \left.\frac{\partial T}{\partial x}\right|_{x^*} = 0 \tag{4.36}$$

$$-K_2 \left.\frac{\partial T}{\partial x}\right|_{x^\circ} + K_3 \left.\frac{\partial T}{\partial x}\right|_{x^\circ} = 0 \tag{4.37}$$

Eqs. (4.23), (4.24), and (4.19) gives the followings:

$$\eta_2^* = \sqrt{\frac{\beta_1}{\beta_2}}\eta_1^* \tag{4.38}$$

$$\eta_2^\circ = \sqrt{\frac{\beta_3}{\beta_2}}\eta_3^\circ \tag{4.39}$$

Substituting Eqs. (4.17), (4.18), (4.35), (4.38), and (4.39) to Eqs. (4.36) and (4.37) gives the following equations:

$$\frac{K_1(T^* - T^s)\exp\left\{(1 - \frac{\beta_2}{\beta_1})(\eta_2^*)^2\right\}}{(T^* - T^\circ)\mathrm{erf}(\sqrt{\frac{\beta_2}{\beta_1}}\ \eta_2^*)\sqrt{\beta_1}} = \frac{K_2}{\{\mathrm{erf}(\eta_2^*) - \mathrm{erf}(\eta_2^\circ)\}\sqrt{\beta_2}} \tag{4.40}$$

$$\frac{K_3(T^i - T^\circ)\exp\left\{(1 - \frac{\beta_2}{\beta_3})(\eta_2^\circ)^2\right\}}{(T^* - T^\circ)\left\{1 - \mathrm{erf}(\sqrt{\frac{\beta_2}{\beta_3}}\ \eta_2^\circ)\right\}\sqrt{\beta_3}} = \frac{K_2}{\{\mathrm{erf}(\eta_2^*) - \mathrm{erf}(\eta_2^\circ)\}\sqrt{\beta_2}} \tag{4.41}$$

The solidus and liquidus positions with respect to time are estimated using Eqs. (4.42) and (4.43).

$$x^* = 2\eta_2^*\sqrt{\beta_2 t} \tag{4.42}$$

$$x^{\circ} = 2\eta_2^{\circ}\sqrt{\beta_2 t} \tag{4.43}$$

4.3 Heat and Solute Transportations in the Mushy Zone

The solutes discharged from the growing solid are transferred to the solidification direction (along the primary dendrite axis direction) by diffusion. The diffusivity, inter-diffusion coefficient, of the solute *i* in the solid was denoted as D_{ij}, whereas that in the liquid is denoted as E_{ij}, where *j* represents all solutes.

The variation of the concentration of solute *i* within a volume element with respect to time is given by (Appendix 4.A)

$$\begin{aligned}\frac{\partial \overline{C}_i}{\partial t} &= \frac{\partial(f C_i + f_s \overline{C_{si}})}{\partial t} \\ &= \frac{\partial(f C_i)}{\partial t} + C_{si}\frac{\partial f_s}{\partial t} + \alpha_i f_s \frac{\partial C_{si}}{\partial t}\end{aligned} \tag{4.44}$$

$\overline{C_i}$: averaged concentration of solute *i* in a volume element

C_i : concentration of solute *i* in liquid

$\overline{C_{si}}$: averaged concentration of solute *i* in solid

C_{si} : concentration of solute *i* at the surface, which is in equilibrium with liquid

f_s : solid fraction

where α_i is a parameter [19,25,26] having a value of 0 or 1 that defines the diffusion limits of the solute *i* in the solid (*i.e.*, α_i = 0 when the diffusion of the solute *i* in the solid is negligible and α_i = 1 when the diffusion of the solute *i* in the solid, such as the case of carbon, is rapid enough to result in homogeneous composition over distances in the order of the primary dendrite diameter).

C_{si} is related to C_i with the partition ratio k_i by the following equation:

$$C_{si} = \mathrm{k}_i C_i \tag{4.45}$$

The solute flux of the solute *i* due to diffusion in a multi-component alloy [25] is

$$J_i = -\sum_j f\, E_{ij}\frac{\partial C_j}{\partial x} - \sum_j \alpha_j f_s D_{ij}\frac{\partial C_{sj}}{\partial x} \tag{4.46}$$

Eqs. (4.44), (4.45), and (4.46) give the following:

$$\begin{aligned}&(1-\alpha_i \mathrm{k}_i) f \frac{\partial C_i}{\partial t} + (1-\mathrm{k}_i) C_i \frac{\partial f}{\partial t} + \alpha_i \mathrm{k}_i \frac{\partial C_i}{\partial t} \\ &\qquad = \sum_j (E_{ij} - \alpha_j \mathrm{k}_j D_{ij})\frac{\partial}{\partial x}\left(f\frac{\partial C_j}{\partial x}\right) + \sum_j \alpha_j \mathrm{k}_j D_{ij}\frac{\partial^2 C_j}{\partial x^2}\end{aligned} \tag{4.47}$$

At the liquidus point and the solidus point,

$$x = x^{\circ} \ : \ f = 1 \quad , \quad C_i = C_i^{\circ} \tag{4.48}$$

$$x = x^{*} \ : \ f = 0 \quad , \quad C_i = C_i^{*} \tag{4.49}$$

Substituting Eq. (4.11) into Eq. (4.47) yields

$$\begin{aligned}(1-\alpha_i \mathrm{k}_i) f \frac{\partial C_i}{\partial t} + (1-\mathrm{k}_i) C_i \frac{\partial f}{\partial t} + \alpha_i \mathrm{k}_i \frac{\partial C_i}{\partial t} \\ = \left\{ \sum_j (E_{ij} - \alpha_j \mathrm{k}_j D_{ij}) \frac{\lambda_i}{\lambda_j} \right\} \frac{\partial}{\partial x} \left(f \frac{\partial C_i}{\partial x} \right) + \left\{ \sum_j \alpha_j \mathrm{k}_j D_{ij} \frac{\lambda_i}{\lambda_j} \right\} \frac{\partial^2 C_i}{\partial x^2}\end{aligned} \tag{4.50}$$

Rewriting Eq. (4.50) gives

$$(1-\alpha_i \mathrm{k}_i) f \frac{\partial C_i}{\partial t} + (1-\mathrm{k}_i) C_i \frac{\partial f}{\partial t} + \alpha_i \mathrm{k}_i \frac{\partial C_i}{\partial t} = M_i \frac{\partial}{\partial x} \left(f \frac{\partial C_i}{\partial x} \right) + N_i \frac{\partial^2 C_i}{\partial x^2} \tag{4.51}$$

$$M_i = \sum_j (E_{ij} - \alpha_j \mathrm{k}_j D_{ij}) \frac{\lambda_i}{\lambda_j} \tag{4.52}$$

$$N_i = \sum_j \alpha_j \mathrm{k}_j D_{ij} \frac{\lambda_i}{\lambda_j} \tag{4.53}$$

Transforming the solute-transfer equation, Eq. (4.51) with Eq. (4.18) provides the following ordinary differential equation.

$$\begin{aligned}\left\{ \lambda_i (2 - \mathrm{k}_i - \alpha_i \mathrm{k}_i) C_i + s_i (1 - \alpha_i \mathrm{k}_i) + \alpha_i \mathrm{k}_i \right\} (-2\beta_2 \eta_2) \frac{\mathrm{d}C_i}{\mathrm{d}\eta_2} \\ = \lambda_i M_i \left(\frac{\mathrm{d}C_i}{\mathrm{d}\eta_2} \right)^2 + (\lambda_i M_i C_i + s_i M_i + N_i) \frac{\mathrm{d}^2 C_i}{\mathrm{d}\eta_2^2}\end{aligned} \tag{4.54}$$

Substituting Eq. (4.11) to Eq. (4.1) and then adopting the obtained equation to the heat-transfer equation Eq. (4.27) gives a simple equation as follows:

$$-2\eta_2 \frac{\mathrm{d}C_i}{\mathrm{d}\eta_2} = \frac{\mathrm{d}^2 C_i}{\mathrm{d}\eta_2^2} \tag{4.55}$$

The boundary conditions Eqs. (4.28) and (4.29) can be characterized as follows:

$$x = x^{*} \ , \quad \eta_2 = \eta_2^{*} \ : \ C_i = C_i^{*} \ , \ f = 0 \tag{4.56}$$

$$x = x^{\circ} \ , \quad \eta_2 = \eta_2^{\circ} \ : \ C_i = C_i^{\circ} \ , \ f = 1 \tag{4.57}$$

To simultaneously solve Eqs. (4.54) and (4.55), the unknown constants are determined to match both the first-order differential equation obtained by Eq. (4.55) and that obtained by eliminating the second-order differential terms from Eq. (4.54). Integrating Eq. (4.55) twice with Eqs. (4.56) and (4.57) yields

$$C_i = \frac{(C_i^{*} - C_i^{\circ}) \left\{ \mathrm{erf}(\eta_2) - \mathrm{erf}(\eta_2^{\circ}) \right\}}{\left\{ \mathrm{erf}(\eta_2^{*}) - \mathrm{erf}(\eta_2^{\circ}) \right\}} + C_i^{\circ} \tag{4.58}$$

Differentiating Eq. (4.58) gives

$$\frac{\mathrm{d}C_i}{\mathrm{d}\eta_2} = \frac{(C_i^* - C_i^\circ)}{\left\{\mathrm{erf}(\eta_2^*) - \mathrm{erf}(\eta_2^\circ)\right\}} \frac{2\exp\left\{-(\eta_2)^2\right\}}{\sqrt{\pi}} \tag{4.59}$$

Eliminating the second-order differential terms from Eq. (4.54) with Eq. (4.55) and defining the constants F_i° and G_i° as follows yields

$$\frac{\mathrm{d}C_i}{\mathrm{d}\eta_2} = (-2\eta_2)(F_i^\circ C_i + G_i^\circ) \tag{4.60}$$

$$F_i^\circ = \frac{(2 - \mathrm{k}_i - \alpha_i \mathrm{k}_i)}{\mathrm{M}_i} \beta_2 - 1 \tag{4.61}$$

$$G_i^\circ = \frac{s_i}{\lambda_i} \left\{ \frac{(1 - \alpha_i \mathrm{k}_i)}{M_i} \beta_2 - 1 \right\} + \frac{\alpha_i \mathrm{k}_i \beta_2 - N_i}{\lambda_i M_i} \tag{4.62}$$

Substituting Eq. (4.58) into Eq. (4.60) gives

$$\frac{\mathrm{d}C_i}{\mathrm{d}\eta_2} = -2\eta_2 \left[\left[\frac{(C_i^* - C_i^\circ)\left\{\mathrm{erf}(\eta_2) - \mathrm{erf}(\eta_2^\circ)\right\}}{\left\{\mathrm{erf}(\eta_2^*) - \mathrm{erf}(\eta_2^\circ)\right\}} + C_i^\circ \right] F_i^\circ + G_i^\circ \right] \tag{4.63}$$

The following equation is a good approximation [25,26] (Appendix 4.B) of the error function for large η_2 (the error of this approximation will be checked after solving the equations, as shown in the later chapter):

$$\mathrm{erf}(\eta_2) \approx 1 - \frac{\exp(-\eta_2^{\,2})}{\eta_2 \sqrt{\pi}} \tag{4.64}$$

Adopting this approximation to Eq. (4.63) yields

$$\frac{\mathrm{d}C_i}{\mathrm{d}\eta_2} = F_i^\circ \frac{(C_i^* - C_i^\circ) 2\exp(-\eta_2^{\,2})}{\left\{\mathrm{erf}(\eta_2^*) - \mathrm{erf}(\eta_2^\circ)\right\}\sqrt{\pi}} - 2\eta_2 \left[\left[\frac{(C_i^* - C_i^\circ)\left\{1 - \mathrm{erf}(\eta_2^\circ)\right\}}{\left\{\mathrm{erf}(\eta_2^*) - \mathrm{erf}(\eta_2^\circ)\right\}} + C_i^\circ \right] F_i^\circ + G_i^\circ \right] \tag{4.65}$$

The following equations are obtained to match Eq. (4.59) and Eq. (4.65):

$$F_i^\circ = 1 \tag{4.66}$$

$$\left[\frac{(C_i^* - C_i^\circ)\left\{1 - \mathrm{erf}(\eta_2^\circ)\right\}}{\left\{\mathrm{erf}(\eta_2^*) - \mathrm{erf}(\eta_2^\circ)\right\}} + C_i^\circ \right] F_i^\circ + G_i^\circ = 0 \tag{4.67}$$

Eqs. (4.61) and (4.66) give

$$\beta_2 = \frac{2M_i}{(2 - \mathrm{k}_i - \alpha_i \mathrm{k}_i)} \tag{4.68}$$

Substituting Eqs. (4.12), and (4.68) into Eq. (4.67) gives the following equation as the constraint conditions of the solutes:

$$\frac{\left\{1 - \mathrm{erf}(\eta_2^\circ)\right\}}{\left\{\mathrm{erf}(\eta_2^*) - \mathrm{erf}(\eta_2^\circ)\right\}} = \frac{2(1 - \mathrm{k}_i)}{(2 - \mathrm{k}_i - \alpha_i \mathrm{k}_i)} \lambda_i C_i^\circ + \frac{(1 + \alpha_i)\mathrm{k}_i}{(2 - \mathrm{k}_i - \alpha_i \mathrm{k}_i)} - \frac{N_i}{M_i} \tag{4.69}$$

The effective partition ratio is obtained as follows:

$$\alpha_i = 1 \ : \quad \mathrm{k}^{\mathrm{ef}} = \mathrm{k}_i C_i^* / C_i^\circ = \mathrm{k}_i (1 - 1/\lambda_i C_i^\circ) \tag{4.70}$$

$$\alpha_i = 0 \ : \quad \mathrm{k}^{\mathrm{ef}} = \int_0^1 C_{si} / C_i^\circ \, \mathrm{d}f_s = \mathrm{k}_i (1 - 1/2\lambda_i C_i^\circ) \tag{4.71}$$

Eqs. (4.70) and (4.71) are convenient to evaluate the extent of back diffusion of the solute in solid. Both the equations correspond to the lever rule where complete diffusion can be adopted, such as for carbon, and the Scheil equation for the slow diffusion solute, respectively.

The four unknown parameters (constants) T^*, η_2^*, η_2°, and λ_i can be readily obtained to match Eqs. (4.12), (4.40), (4.41), and (4.69) through a trial-and-error method (as shown in Appendix 4.C), where $\mathrm{K}_1, \mathrm{K}_2, \mathrm{K}_3, \beta_1$, and β_3 are given by the reported physical properties and T^i is given as the initial condition. T^s is given such that the same heat extraction as that produced in a real process (Appendix 4.D). The liquidus temperature T° is estimated using the reported formula [28] and both β_2 and λ_i are related to T^* by Eqs. (4.21) and (4.12). Consequently, the four equations involve only the four unknown parameters (T^*, η_2^*, η_2°, and λ_i), which should be fixed. It takes several minutes to fix these four parameters by manual calculations using spreadsheets. Alternatively, they can be fixed instantly using the algorithm shown in Appendix 4.C either with a personal computer or a tablet computer.

It should be noted that the solutions of heat, Eqs. (4.26), (4.30), and (4.35), are the exact analytical solutions and the solutions for solutes are determined by employing the approximation, Eq. (4.64), to match Eqs. (4.54) and (4.55) (*i.e.*, the material (solutes) solutions are obtained to be consistent with the heat solution). This approximation [25,26] is accurate for the large η_2 (*e.g.,* the errors of the approximation for the case $\eta_2 > 1.24$, $\eta_2 > 1.39$ and $\eta_2 > 1.72$ are less than 2.0%, 1.0%, and 0.2%, respectively, Appendix 4.B).

It is also noted that the existence of the unique solution of the heat and mass transfer simultaneous equations Eqs.(4.55) and (4.54) are shown in Appendix 4.I and 4.J..

4.4 Results

4.4.1 Physical Properties

The physical properties [30–40] used in the model are listed in Table 4.1. The compositions of the steel investigated in this study are listed in Table 4.2, in which the measured and predicted solidus temperatures are shown along with the corresponding partition ratios of carbon used in the model. Selection of the values for thermal conductivity in the mushy zone warrants discussion because measurements have not been made under

conditions that correspond to this solid-liquid region, particularly with respect to fluid flow. Thermally driven flow adjacent to the solidification front can give rise to estimated velocities of 0.1 to l cm/s [8,41] while solidification shrinkage may generate a fluid velocity of about 0.01 cm/s [42]. Consequently, the thermal conductivity in the mushy zone could be larger than that measured in a stagnant liquid. However, the difference is not expected to be great because heat flow by conduction is large compared to that by convection at the low fluid velocities estimated in the inter-dendritic region. Moreover, a significant fraction of the mushy zone consists of fixed solid dendrites unaffected by fluid flow. Thus a thermal conductivity measured under stagnant conditions has been used for the mushy zone, Table 4.1.

The same argument does not hold when considering inter-diffusion coefficients in the inter-dendritic liquid because the rate of solute transport by diffusion is low relative to that by convection. Hence, inter-diffusion coefficients measured in a stagnant liquid cannot be adopted for the inter-dendritic region.

However, the inter-diffusion coefficients in the inter-dendritic liquid can be obtained as the parts of the solution of the simultaneous heat- and mass- transfer equations. This is the approach taken in the present model. Hence, the estimated inter-diffusion coefficients of the solutes include the influence of fluid flow and should be larger than values obtained under stagnant conditions [43].

It should be noted that temperature changes such as liquidus temperature, resulting from the individual alloys are additive as long as solute-solute interactions are negligible as assumed in (II-1) in the Chapter 4.2.2. This assumption may not be always correct, however Kirkaldy and Baganis [44] found that the assumption of the negligible interactions between solutes is valid as long as the total alloy elements(solutes) is less than 6% and the Si content<1%. Therefore, the general steel of the total solutes less than 3.5% were subjected to investigate in the model. It is also noted that the difference of the densities of the solid and the liquid in the mushy zone (3-4%) was neglected because the magnitude of the error caused by this neglect was estimated to be less than 0.1% (the influence of the latent heat is dominant comparing with that of the heat conduction due to this neglect in the mushy zone).

It is known that the enrichment of sulfur in inter-dendritic liquid results in sulfide precipitations during solidification [44,45]. Ueshima et al. [45] demonstrated that MnS precipitation predicted by their thermodynamic investigation agreed with the measurements obtained for Si- and Al-killed steel. Accordingly, the maximum sulfur concentration in a mushy zone is restricted by the precipitations of MnS (*i.e.*, the solubility product of [%Mn] [%S] in a mushy zone). However, taking into account this restriction would complicate the model proposed in this study. Therefore, the influence of sulfur was excluded in the model when MnS precipitation is expected but is estimated separately (*i.e.*, typically, in the cases of steel K and M in Table 4.2).

Regarding phosphorus, phosphates have been found to be precipitated in high-carbon steels [46]; however, phosphate precipitations are not expected in the present study due to the larger partition ratio of [P] than that of [S] in low- and intermediate-carbon ranges (the primary phase is δ Fe). Therefore, [P] is accounted for as like as other alloy solute in the present model.

The solidification of a liquid begins using a water-cooled mold, followed by water spraying in the continuous casting process of steel. The surface temperature of a slab of steel is generally measured using optical instruments that are installed in the lower positions of a caster because of facility restrictions. Under such circumstances, Meng and Thomas [47] performed reliable and continuous measurements of a continuously cast 0.45% C steel using a thermocouple with a block fed into a mold. The surface temperature T^s that results in almost same amount of heat extraction as that estimated by Meng and Thomas [47] is used in the present model (Appendix 4.D). In this study, the superheat in a mold (*i.e.*, the overheating of the bulk liquid to the liquidus temperature) was assumed to be 15 K (15 °C) if it is not specified in the later chapter.

The solidification of the steel in the low and intermediate carbon is complicated due to the peritectic reaction. You et al. [48] proposed the model to adopt the variable partition ratio of carbon coupled with the thermodynamic library and with both commercial and self-optimized databases in the back ground. The present model adopts the similar concept to change the value of the partition ratio of carbon k_C in accordance with the increase of the carbon concentration of the steel.

Only δ -Fe precipitates in the range of the carbon concentration less than the peritectic composition, so that $k_C = 0.19$ was adopted for the steel in this low carbon range C<0.15%. The γ -Fe with partition ratio of carbon (0.3–0.4) larger than that of δ -Fe begins to precipitate when the carbon concentration in the steel exceeds 0.15%, so that the larger partition ratio of carbon, $k_C = 0.225$, was adopted for the intermediate carbon steel. From the viewpoint of the mathematical limitation of the model, it is also reasonable to adopt a larger k_C for the higher carbon steel to keep the error of the approximation Eq.(4.64) as small as possible, because the adopting larger k_C yields the larger η^* obtained as the solution of the model. The selected values for k_C from the reported are, $k_C = 0.19$[30]; C < 0.15%, $k_C = 0.225$[31,32]; 0.15 ≤ C < 0.25%, $k_C = 0.25$[32]; 0.25 ≤ C < 0.30% and $k_C = 0.29$[33]; 0.30 ≤ C ≤ 0.35% (Appendix 4.E).

The partition ratios of other solutes used in the model are listed in Table 1. The formula for the liquidus temperature by Kawawa et al. [28] was used in the model.

Table 4.1 Physical properties used in the present model.

		Property	Value
I zone	ρ_1	Density	7.7×10^3 kg/m^3
	C_{p1}	Specific heat	0.77 kJ/kgK
	K_1	Thermal conductivity	30.6 W/mK
	L	Heat of fusion	276 kJ/kg
II zone	ρ_2	Density	7.5×10^3 kg/m^3
	C_{p2}	Specific heat	0.77 kJ/kgK
	K_2	Thermal conductivity	31.8 W/mK
	k_C	Partition ratio of C in δ-Fe	0.19 [30]
			0.225 [31,32]
			0.25 [32]
			0.29 [33]
	k_{Mn}	Partition ratio of Mn in δ-Fe	0.76 [34]
	k_{Si}	Partition ratio of Si in δ-Fe	0.77 [33]
	k_P	Partition ratio of P in δ-Fe	0.23 [34]
	k_S	Partition ratio of S in δ-Fe	0.05 [35]
	k_{Cr}	Partition ratio of Cr in δ-Fe	0.95 [35]
	k_{Ni}	Partition ratio of Ni in δ-Fe	0.8 [36]
	α_C	Parameter for diffusion in solid	1
	$\alpha_{Mn}, \alpha_{Si}, \alpha_P, \alpha_S, \alpha_{Cr}, \alpha_{Ni}$	Parameter for diffusion in solid	0
	D_C	Inter-diffusion coefficient of C in solid	6.6×10^{-10} m^2/s [37]
	D_{Mn}	Inter-diffusion coefficient of Mn in solid	1.7×10^{-11} m^2/s [38]
	D_{Si}	Inter-diffusion coefficient of Si in solid	3.5×10^{-11} m^2/s [34]
	D_P	Inter-diffusion coefficient of P in solid	3.2×10^{-10} m^2/s [39]
	D_S	Inter-diffusion coefficient of S in solid	2.1×10^{-10} m^2/s [40]
III zone	ρ_3	Density	7.4×10^3 kg/m^3
	C_{p3}	Specific heat	0.77 kJ/kgK
	K_3	Thermal conductivity	31.8 W/mK
Liquidus temperature for general steel		$T° = 1809 - 78*(\%C) - 4.9*(\%Mn) - 7.6*(\%Si) - 34.4*(\%P) - 38*(\%S) - 1.3*(\%Cr) - 3.1*(\%Ni)$ K [28]	

Table 4.2 Chemical compositions of the various grade steels (in mass %) and the solidus temperature T^*.

(For steel G1, interactions between silicon and carbon was neglected because carbon concentration is low)

Steel	C	Mn	Si	P	S	Cr	Ni	Measured solidus emperature	Predicted Solidus temperature	k_c
G1	0.04	—	3.0	—	—	—	—	1754^{+}	1760*	0.19
G2	0.25	1.4	0.25	—	—	0.1	0.75	1729^{++}	1721*	0.25
G3	0.35	1.3	0.08	—	—	0.25	0.2	1710^{++}	1709*	0.29
Jernkontoret 201	0.11	1.25	0.12	0.04	0.018	0.06	0.03	1728^{++}	1751**	0.19
Jernkontoret 202	0.12	1.53	0.27	0.01	0.005	0.02	0.03	1733^{++}	1747*	0.19
Jernkontoret 203	0.18	1.26	0.44	0.016	0.025	0.01	0.02	1733^{++}	1735**	0.225
Jernkontoret 204	0.19	1.42	0.4	0.012	0.007	0.07	0.13	1733^{++}	1728**	0.225
Jernkontoret 209	0.2	0.9	0.25	0.014	0.039	0.81	1.05	1718^{++}	1727**	0.225
Jernkontoret 211	0.29	0.62	0.21	0.012	0.006	1.11	0.15	1723^{++}	1711*	0.25
Jernkontoret 213	0.35	0.67	0.24	0.01	0.02	0.92	0.05	1698^{++}	1699**	0.29
Smetana et al.	0.077	0.635	0.291	0.021	0.008	0.049	0.027	1765^{+++}	1765*	0.19
S1	0.06	1.05	0.008	0.0007	0.0006	—	—	1767	1779*	0.19
S2	0.13	1.04	0.005	0.0005	0.0006	—	—	1752	1753*	0.19
S3	0.18	1.06	0.007	0.0006	0.0006	—	—	1744	1745*	0.225
S4	0.27	1.04	0.01	0.0007	0.0006	—	—	1725	1724*	0.25
K	0.15	0.7	0.22	0.017	0.019	—	—	—	1751**	0.225
M	0.2	1.33	0.36	0.029	0.038	—	—	—	1727**	0.225
W11	0.044	1.05	0.015	0.0009	0.0008	—	—	—	1785*	0.19
W12	0.18	1.05	0.015	0.0009	0.0008	—	—	—	1745*	0.225
W21	0.044	0.61	0.24	0.015	0.009	—	—	—	1778*	0.19
W22	0.18	0.61	0.24	0.015	0.009	—	—	—	1738*	0.225
W31	0.044	1.52	0.34	0.012	0.015	—	—	—	1775**	0.19
W32	0.18	1.52	0.34	0.012	0.015	—	—	—	1735**	0.225

(+): DSC −0.1 K/s

(++): DSC+0.017–0.025 K/s

(+++): DTA +0.17 K/s

(*): [P] accounted, [S] accounted

(**): [P] accounted, [S] not accounted (accounted MnS precipitation)

4.4.2 Applications of the Model to General steel

4.4.2.1 Thermal Analysis

The transition temperature of general steel (in this case, steel K) cast to a thickness of 0.22 m after 240 s as predicted by the present model is shown in Fig. 4.2. The partition ratio of carbon k_C = 0.225 was used. The surface and initial temperatures, T^s and T^i, respectively, were 1423 and 1812 K (1150 and 1539 °C) (superheat ΔT = 15 K (15 °C)). [S] was not accounted for in the model, because MnS precipitation was expected; the extra drop in the solidus temperature that should occur due to [S], estimated as 0.4 K, was therefore not accounted for in the model (Appendix 4.F). The liquidus and solidus temperatures predicted by the present model, which accounts for the additional solutes ([Mn], [Si], [P], and [S]) were slightly lower than those predicted by the Fe–C binary model [26] where only carbon is considered. However, the influence of these on the solidification constants was not serious (*i.e.*, the changes in the solidification constants of the liquidus and solidus points were 0.9% and 3.9%, respectively, as shown in Table 4.3) as the constants were within the range of the dispersions (*i.e.*, 4%–6%) of the results of the shot bullets measurements [1] (Table 4.3).

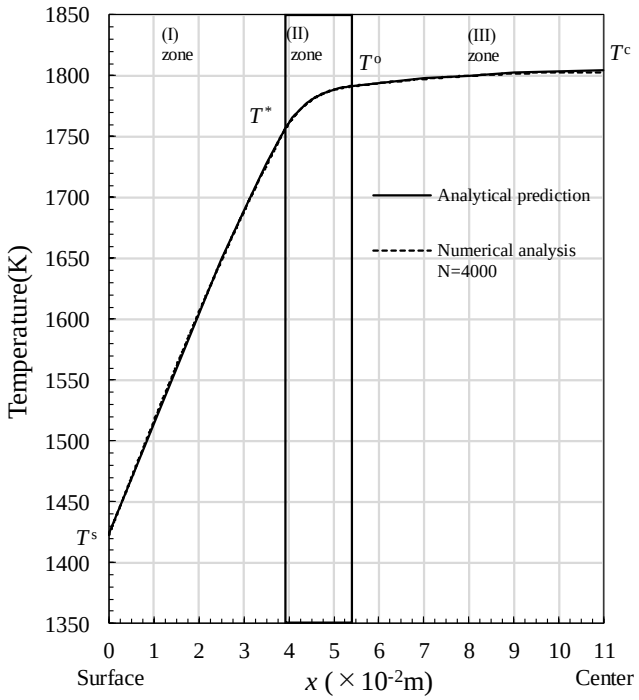

Fig.4.2 Transition temperature predicted by the model and the numerical analysis of the continuously cast steel K. (T^s = 1423 K, ΔT = 15 K, t = 240 s, slab thickness = 22 × 10^{-2} m, N = partition number of the half thickness of a slab; in this figure, [P] is accounted for but not [S]).

Table 4.3 Liquidus and solidus temperatures and solidification constants as predicted by the present model (*i.e.*, the multi-component model) and the binary model [26] for steel K (ΔT = 15 K).

	Present model (P: accounted, S: not accounted)		Binary model [26] (P: not accounted, S: not accounted)	
	T(K)	Solidification constant ($\times 10^{-2}$ m/s$^{1/2}$)	*T*(K)	Solidification constant ($\times 10^{-2}$ m/s$^{1/2}$)
Liquidus	1791	0.347	1797	0.344
Solidus	1751	0.245	1763	0.255

A numerical heat analysis was made separately (represented by the dashed line in Fig. 4.2). A conventional equivalent specific heat method [49] and an upwind finite-difference method were used in the numerical analysis, assuming that the fraction of solid is linear to temperature in the mushy zone. A symmetric condition was used at the center of the slab. The numerical analysis and the analytical solutions (*i.e.*, the present model) were in good agreement, as indicated by both Fig. 4.2 and Table 4.4. Better agreements were obtained when the partitioning of the target slab thickness was increased (*e.g.*, the difference between the solidus points predicted by the numerical analysis and the model was less than 0.5% for a partitioning of 4000 for a half thickness of a slab); this can be seen in Table 4.4.

Table 4.4 Comparison of the predicted liquidus and solidus positions by the analytical solution (present model) and the numerical analysis of the continuously cast steel K (ΔT = 15 K, t = 240 s, T° = 1792 K, T^* = 1752 K, [P] is accounted for but [S] is not).

Distance from the surface ($\times 10^{-2}$ m)		Present model	Numerical analysis	
			(N = 4000)	(N = 2000)
Liquidus point	x°	5.37	5.39	5.40
Solidus point	x^*	3.79	3.81	3.82

The decrease in temperature at the center of cast slabs was estimated to be 3 K (or 3 °C) by the numerical analysis; this value was within the accuracy range of the temperature measurements. In addition, the heat supply to the central region of the cast steel by liquid down streams from the mold and by convection in bulk liquid was considered to limit the decrease in temperature in this region. Consequently, the assumption that the

temperature at the center of the slabs is kept constant made in the model is reasonable, at least from a practical viewpoint. The errors of the approximation yielded by Eq. (4.64) for the case in Fig. 4.2 are less than 0.2%. The present model involves a Fe–C binary system model [26], which converges to Neumann's solution (*i.e.,* the solution for the pure metal) in a low carbon range (*e.g.*, [%C] < 0.03%) at t=240s as shown in Fig.4.3. This convergence with Neumann's solution in a low carbon range (*e.g.*, [%C] < 0.03%) was also found at the early stage of the solidification (Appendix 4.G). The good agreements of the present model predictions of the shell thickness at the early stage of solidification with the measurements of the breakout shell thickness by Meng and Thomas [47] were also obtained (Appendix 4.G).

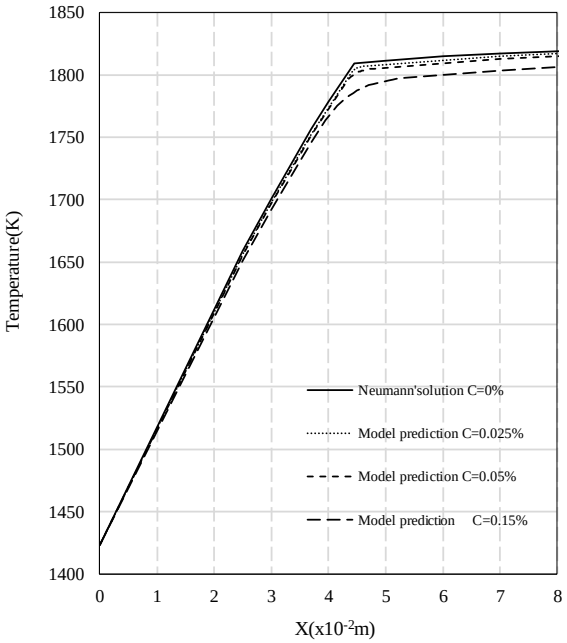

Fig.4.3 Transitions of temperature predicted by the model and the Neumann' solution (*C*= 0%) of a continuously cast steel. (C=0%–0.15%, T^s = 1423 K (1150 °C), ΔT = 15 K (15 °C), t = 240 s, slab thickness = 0.22 m) [26].

4.4.2.2 Material Analysis

The transitions of the solute concentrations and the liquid fraction in the mushy zone of steel K predicted by the model are shown in Fig.4.4 The thick lines indicate the segregation ratios ($C/C°$) of the solutes. The segregation ratio of [C] at the solidus point is larger than those of [Mn] and [Si]. The effective partition ratios of [C], [Mn], and [Si] shown in Table 4.5 are in the range of 0.88–0.98; these are in good agreement with the generally accepted values (0.85–1.0). However, the effective partition ratio of [P] is somewhat smaller than the general findings; this may be due to the development of secondary dendrites or because the precipitation

of phosphate was neglected in the model.

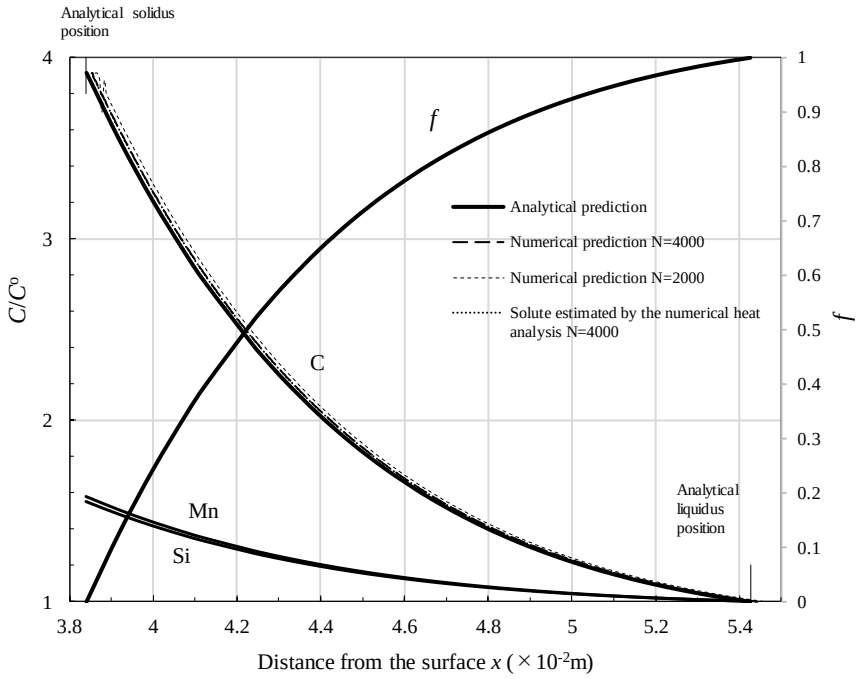

Fig. 4.4 Solute concentration and liquid fraction predicted by the model and numerical analysis of the continuously cast steel K (T^s = 1423 K, ΔT = 15 K, t = 240 s, slab thickness = 22 × 10^{-2} m, and N = partition number of the half thickness of a slab. In this figure, [P] is accounted for but not [S]).

Table 4.5 Predicted segregation ratios, effective partition ratios, and Mi (diffusivity) of the continuously cast steel K (ΔT = 15 K, t = 240 s).

	Present model ([P]: accounted, [S]: not accounted)			Model by Fujimura et al. [25] wherein measured solidification constants were used ([P],[S] : not accounted)		
Solute	C^*/C°	k^{ef}	Mi(m^2/s)	C^*/C°	k^{ef}	Mi(m^2/s)
C	3.91	0.88	4.11×10^{-7}	3.86	0.91	3.98×10^{-7}
Mn	1.58	0.98	3.36×10^{-7}	1.69	0.98	3.30×10^{-7}
Si	1.55	0.98	3.26×10^{-7}	1.56	0.99	3.20×10^{-7}
P	5.76	0.78	5.01×10^{-7}	–	–	–

$M_C = E_{CC} + 1.07E_{CMn} + 0.30E_{CSi} + 0.20\,E_{CP}$ $M_C = E_{CC} + 1.12E_{CMn} + 0.29E_{CSi}$

$M_{Mn} = 1.07E_{MnC} + E_{MnMn} + 0.30E_{MnSi} + 0.20E_{MnP}$ $M_{Mn} = 0.89E_{MnC} + E_{MnMn} + 0.26E_{MnSi}$

$M_{Si} = 3.61E_{SiC} + 3.36E_{SiMn} + E_{SiSi} + 0.67\,E_{SiP}$ $M_{Si} = 3.49E_{SiC} + 3.92E_{SiMn} + E_{SiSi}$

$M_P = 5.40E_{PC} + 5.03E_{PMn} + 1.50E_{PSi} + E_{PP}$

The estimated carbon diffusivity, parameter M_C, 4.11 $\times 10^{-7}$ m^2/s, was in good agreement with the carbon inter-diffusion coefficient estimated by Asai and Muchi [19] (4.7 $\times$ 10^{-7} m^2/s) and by Fujimura and Brimacombe [25] (3.98 $\times$ 10^{-7} m^2/s) estimated for a Fe-0.15%C-0.70%Mn-0.22% Si continuously cast steel. Although these values are somewhat larger than that measured by Grace and Derge [50] (2–4 $\times$ 10^{-7} m^2/s) under stagnant conditions, these are reasonable as discussed earlier (Chapter 4.4.1).

The present analytical predictions for the concentration of carbon (thick solid line) and those predicted by the conventional heat analysis, which provides the solute concentration by Eq. (4.58), adopting the solidus temperature T^* (thin dotted line), were in good agreement, as shown in Fig.4.4; the results are close and overlapped each other. The concentration of carbon predicted by the numerical analysis, which directly solved the solute-transfer equation Eq. (4.60) with a lager partitioning N = 4000 (thick dashed line), was also in good agreement with the present analytical predictions (thick solid line) where T^* predicted by the model was used.

These agreements show that a conventional heat analysis such as the equivalent specific heat method adopting the solidus temperature predicted by the model provides solutions not only for the temperature but also for the solute concentrations, which are consistent with each other. In other words, this model provides a simple numerical heat analysis, which is consistent with the simultaneous solutions to the heat- and solute-transfer equations without solving them, when T^* predicted by the model is used. Thus, the present model is considered to significantly simplify the extensive computations required to solve the simultaneous equations and search the solidus temperature with associated solutes diffusivities as parts of simultaneous solution.

4.4.2.3 Temperature in a Mushy Zone

The model was evaluated using the measurement of the temperature in the mushy zone of a continuously cast steel (steel M), a 24 $\times$ 10^{-2} m $\times$ 24 $\times$ 10^{-2} m square bloom, which was measured by Mori et al. [51] using hybrid shot bullets made of different metals. The temperatures measured at different locations relative to the liquidus point are shown in Fig.4.5. The superheat of the liquid poured into the mold was assumed to be 20 K. MnS was expected to be precipitated for this steel, as shown in Appendix 4.F. Hence, [S] was not accounted for in the model. The extra drop of the solidus temperature due to [S] is considered to be negligible or at least less than 0.4 K because the solubility of sulfur is limited by the [Mn][S] product. The predicted temperature profile shown with the thick line (*i.e.*, in which [P] was accounted for but not [S]) in this figure is in good agreement with the measured temperature profile. The predicted temperature profiles shown by the thick dotted

line (in which neither [P] nor [S] was accounted for) and the thin dotted line (in which both [P] and [S] were accounted for) deviate from the measured profiles. Thus, the better agreement is obtained for steel M when [S] is not accounted for but [P] is. The solidus temperatures predicted by the model are in the intermediate range of those estimated by the reported formulas [3–5]. The errors of the approximation, as yielded by Eq. (4.64), are less than 1.4%.

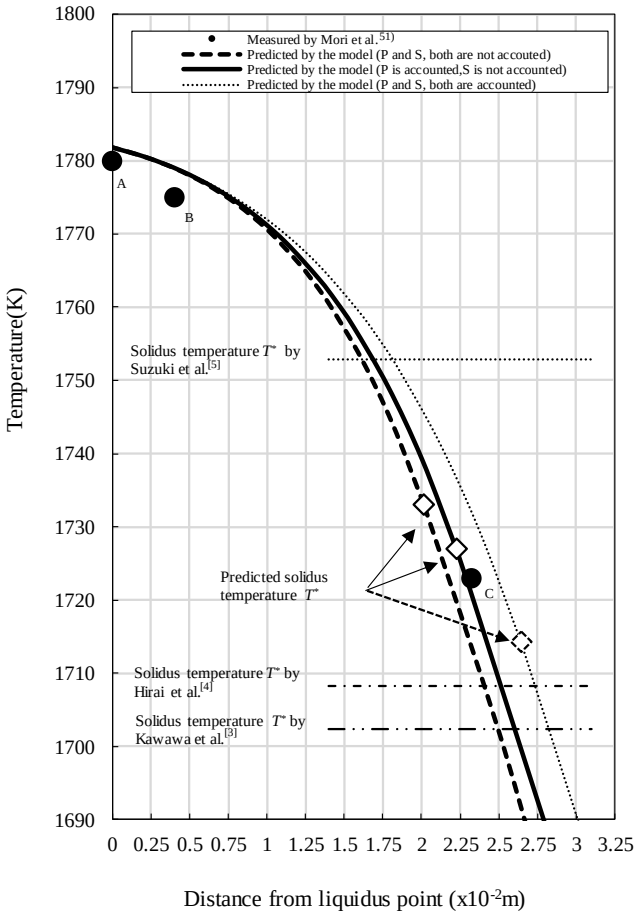

Fig. 4.5 Transitions temperature predicted by the model and measurements [51], with shot bullets in the continuously cast steel M (T^s = 1423 K, ΔT = 20 K, and t = 317 s; [P] is accounted for, but not [S]). In the figure, the points denoted by A, B, and C correspond to the liquidus position of the studied steel, the position of a melted bullet shell, and the position of a melted Ni rod in a bullet, respectively).

4.4.2.4 Solidus Temperature

As shown earlier, the solidus temperature T^* was obtained as the part of the simultaneous solutions of heat- and solutes-transfer equations Eqs. (4.54) and (4.55). However, this T^* can be explicitly obtained using Eqs.

(4.21) and (4.68), as shown in Eq. (4.72), which is the goal of the present model.

$$T^* = T^\circ - \frac{L}{\frac{(2-\mathrm{k}_i-\alpha_i\mathrm{k}_i)K_2}{2\rho_2\mathrm{M}_i} - Cp_2} \tag{4.72}$$

The solidus temperature T^* estimated with Eq. (4.72) exactly matches the set of solutions satisfying Eqs. (4.12), (4.40), (4.41), and (4.69). Parameter M_i corresponds to the inter-diffusion coefficients predicted by the simultaneous solutions. The changes of the important parameters predicted by the model for Steel S3 in table 4.2, for example, with respect to the surface temperature are shown in Fig.4.6. The solidus temperature T^* and parameter *Mi* remained almost constant. In contrast, the solidification constants ν°, ν' and the averaged cooling rate *R* of a mushy zone slightly increased with the decrease of surface temperature (the cooling rate *R* is defined as the averaged cooling rate of the liquidus point at t=240s to complete the solidification.). This suggests that the stronger cooling of the surface increases the cooling rates but not the solidus temperature and the associated *Mi*. It should be noted that the solidus temperature predicted by Eq.(4.72) does not involve the physical properties which are sensitive to the cooling rate.

4.5 Discussion

The solidus temperature T^* of the model was compared with the zero strength temperature (ZST) and zero ductile temperature (ZDT). Above the ZST, solidifying steel has no strength and no ductility but does have some strength due to the mechanical network between dendrites. As long as some liquid remains, the steel fails in brittle manner due to a rapid strain concentration and failure of the inter-dendritic film. Below the ZDT, the solidifying steel behaves as a solid with strength and ductility. The ZDT should, therefore, theoretically be found at the nonequilibrium solidus temperature [16]. It was also considered that the measured ZDT depends on the cooling rate as many of back diffusion models predict [12-16]. However, measurements of the ZDT [52,53,54] are much less sensitive to cooling rate. Soel et al. [52] determined that increasing the cooling rate 1K/s to 10K/s decreased measured ZDT only 5-10K for 0.12%C and 0.45%C steel. This insignificant dependency of the solidus temperature on the cooling rate can be readily explained by the present model, Eq. (4.72) and Fig. 4.6. Shin et al. [53] measured the ZST and the ZDT for steels S1–S4, as shown in Fig. 4.7. A nonequilibrium phase diagram of Fe–C–1.0% Mn calculated by Shin et al. [53] (CALPHAD method) is also shown in Fig. 4.6. The ZST and the ZDT were measured under a cooling rate of 0.17 K/s, while the averaged cooling rates in a mushy zone expected by the model were 0.16 K/s at t = 240 s, the instantaneous cooling rates

at liquidus and solidus point are 0.053 K/s and 0.53 K/s at t = 240 s, respectively.

The solidus temperatures predicted by the present model were in reasonable agreement with the ZDT measured by Shin et al. [53]. Won and Thomas [16] obtained a solidus temperature (the two-dotted chain line in the figure) by assuming a constant cooling rate of 0.17 K/s and considering the back diffusion of the solutes (the parameters obtained by the dendrite coarsening model [15] was adopted in Clyne and Kurz model [13]). The solidus temperatures predicted by the present model were also in reasonable agreement with the solidus line predicted by Won and Thomas [16].

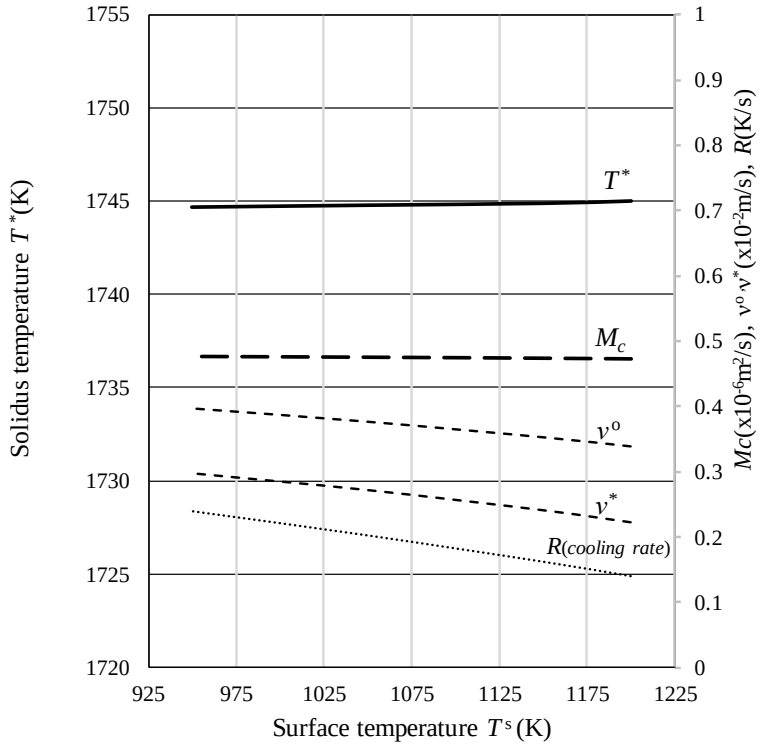

Fig.4.6 Effect of the surface temperature on the solidus temperature T^*, the solidification constants ν°,ν^* and the cooling rate R. Steel S3:0.18%C,1.06%Mn,0.07%Si,0.0006%P,0.0006%S, ΔT=15K, and t=240s.

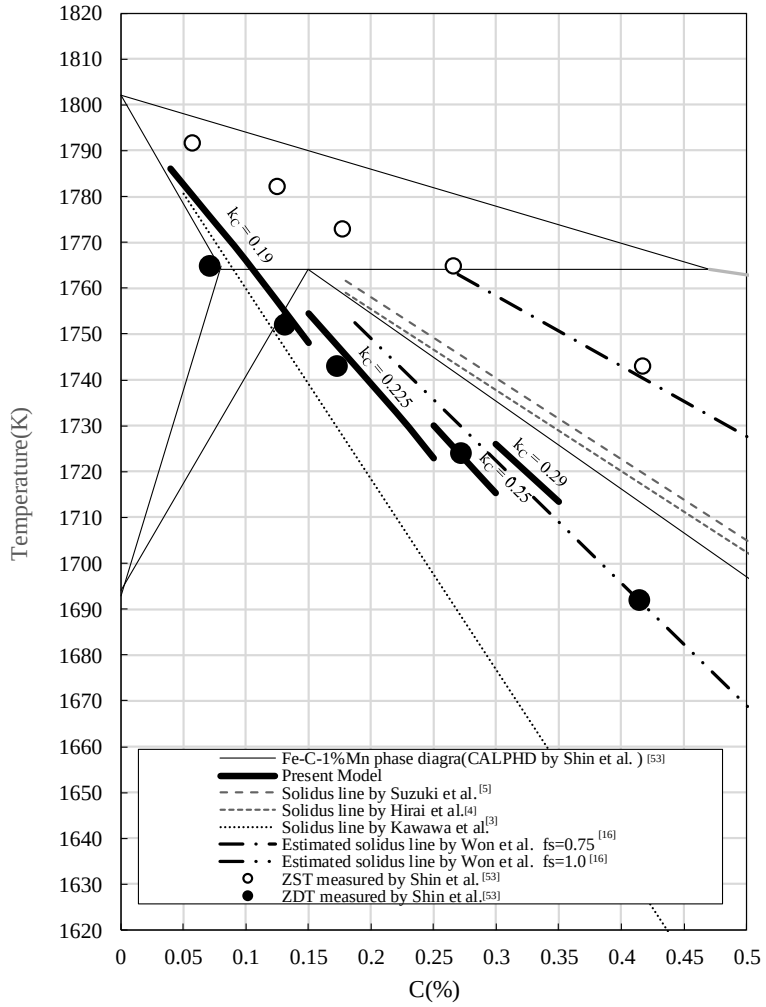

Fig.4.7 Solidus temperature predicted by the model for different k_C values, solidus temperatures estimated with reported formulas [3–5], ZST and ZDT values of 1.05% Mn–0.015% Si–0.0007% P–0.0006% S steel (S1–S4 in Table 4.2) measured by Shin et al. [53] and Fe–C–1.0% Mn phase diagram (calculated by Shin et al. [53] using the CALPHAD method). The model predictions were obtained with different k_C in accordance with carbon concentration range (Appendix 4.E). The approximation errors of Eq. (4.64) remained lower than 2.0%.

Finally, the solidus temperature predicted by the model was validated against the thermo-analytical measurements [6,55,56] as shown in Fig.4.8 (the thick line is an ideal line); the solidus temperatures estimated by the reported formulas [3–5] and by the computations [6,16,56] are also shown in Fig.4.8.

The solidus temperatures predicted by the present model (Table4.2) are in reasonable agreement with that measured by Gryc et al. [6] and Smetana et al. [56] within ±8 K and Jernkontret steel [55] within ±12 K,

while those of Jernkontret steel 201 (0.11%C) and 202 (0.12%) shows the larger deviations (23K,15K respectively). Jernkontret steel 201 and 202 are the steel at which typically peritectic reaction(δ-Fe+liquid→γ-Fe) occurs. The phosphorous in δ-Fe rapidly discharged to the residual liquid due to the peritectic reaction depresses the solidus temperature. This is because phosphorous has very low partition ratio, which are even smaller for the γ-Fe than for δ-Fe. Furthermore, the amount of the solidified δ-Fe to transform to γ-Fe within the range of carbon concentration from 0.1% to 0.15% is relatively larger than in that of carbon concentration larger than 0.15%, so that the depression of the solidus temperature due to the enrichment of the solutes is more significant for Jernkontret steel 201 and 202 than for the higher carbon steel (*e.g.* Jernkontret steel 203 or 204). The similar depression of the ZDT in the rage of 0.1%C to 0.2%C were observed in the measurements by Schmidtmann et al. [54] at the higher cooling rate 10k/s. Accordingly, the considerable underestimations of the present model for Jernkontret steel 201 and 202 are because the present model does not account for the influence of the rapid peritectic reactions in the range of 0.1%C to 0.15%C.

The present model predictions are in fair agreement with the thermodynamic estimations by Sugden and Bhadeshia [57]. The predictions of the present model are roughly 10K lower than those by Sugden et al.. These underestimations are reasonable because the micro-segregation are not accounted in the thermodynamic model by Sugden and Bhadeshia. The present model predictions are also roughly in good agreement with those of the back diffusion model by Won and Thomas [16]. even though the approaches to obtain the solidus temperature by the present model are completely different from those by Won and Thomas. The comparison of the both models to obtain the solidus temperature is shown in Table 4.6. The computed results obtained via the commercial software by Gryc et al. [6] for steels G2 and G3 were also in good agreement with both the measured values and those predicted by the model, while the considerable deviation of the computed for steel G1 (*i.e.*, a high-Si steel) from others was observed. This extreme overestimation for steel G1 computed by Gryc et al. is conceivably attributed to the limitation of the commercial software for the high Si steel [6]. The model predictions were in the intermediate range of those calculated using reported formulas [3–5].

The solidus temperatures of the present model are explicitly formulated in accordance with the carbon concentration, as shown in Appendix 4.H. The estimations by these formulations are within ±9 K of the model predictions for the steel listed in Table 4.2.

Thus, accordingly, it is considered that the present model can provide the reasonable solidus temperature for the various grades steel, which are in reasonable agreement with the reported values. The benefits of the

present model are as follows: (1) The present model provides the solidus temperature for various grades steel which is instantly obtained by the algorithm shown in Appendix 4.C either with a personal computer or a tablet computer. (2) The present model also provides the numerical heat analysis (*i.e.* equivalent specific heat method) which is consistent with the solute- transfer equations by adopting the solidus temperature predicted by the model. The model is also consistent with Neumann's solution at the low carbon concentration. (3) This model can reduce the large amount of computational power to search for the solidus temperature and to solve the heat- and solutes- transfer simultaneous equations in a mushy zone of the multicomponent alloy steel.

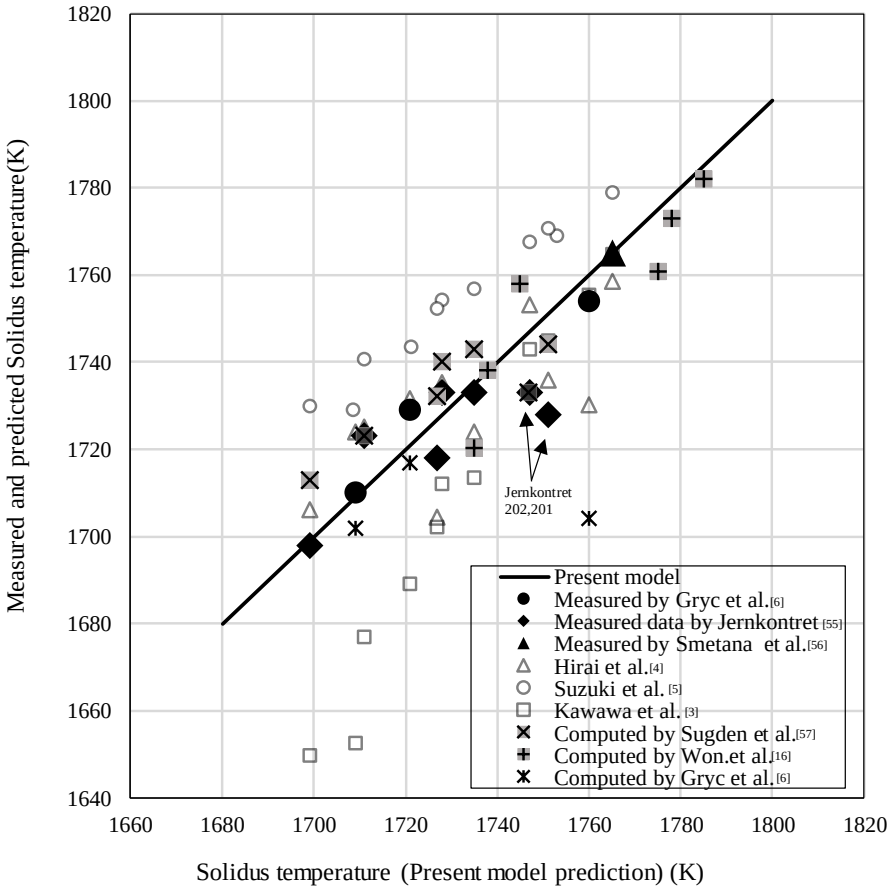

Fig.4.8 Comparison of the solidus temperatures predicted by the present model and those estimated with the reported formulas [3-5], measurements [6,55,56], and those computed [6,16,57].

4.6 Conclusions of this Chapter

An approximate analytical model was developed to obtain simultaneous solutions, such as the solidus temperature for a multi-component alloy steel for nonlinear solute- and heat-transfer equations in the unsteady state mushy zone; in this model, a linear relation between the solid fraction and temperature in the mushy zone was assumed. The model predictions agree well with the conventional numerical heat analyses such as the equivalent specific heat method. The predicted solidification constants and the effective partition ratios of solutes were also found to be in good agreement with both the reported measurements and generally accepted values. Good agreement was also found for predictions made by the model and shot bullet measurements made in the mushy zone of high-manganese steel. The predicted solidus temperatures for various grades steel were in reasonable agreement with the measured ZDT and the reported thermo-analytical measurements. Furthermore, the predictions were also in fair agreement with those by a thermo-dynamic model and a back diffusion model for the high-manganese steel.

Large amount of computational power is required to solve simultaneous solutions for the heat- and solute-transfer equations of the mushy zone of multi-component alloy steel. This model provides approximate analytical solutions that can reduce the required computational load, saving both time and cost. This model also involves the Fe-C binary alloy model [26] which is consistent with the Neumann's solution in the low carbon concentration range. The present model also shows that conventional heat analyses (such as an equivalent specific heat analysis method) that use solidus temperatures obtained by the model provide not only temperature but also solute concentrations as simultaneous solutions for the heat- and solute-transfer equations of multi-component alloy steels.

Appendix 4.A

(1) Derivation of Eq.(4.12)

The following equations are obtained from Eq.(4.3).

$$f = 1 \ : 1 \ = \lambda_i C_i^{\circ} + s_i \tag{4.A1}$$

$$f = 0 \ : 0 = \lambda_i C_i^{*} + s_i \tag{4.A2}$$

$$C_i^{*} = -\frac{s_i}{\lambda_i} \tag{4.A3}$$

$$s_i = 1 - \lambda_i C_i^{\circ} \tag{4.A4}$$

$$(C_i^{\circ} - C_i^{*}) = \frac{1}{\lambda_i} \tag{4.A5}$$

Multiplying Eq.(4.A5) with m_i and summing with respect all solutes gives

$$\sum_i \frac{\mathrm{m}_i}{\lambda_i} = \sum_i \mathrm{m}_i (C_i^{\circ} - C_i^{*}) \tag{4.A6}$$

Eq.(4.1) and Eq.(4.A6) give Eq.(4.12).

$$T^{*} = T^{\circ} - \sum_i \frac{\mathrm{m}_i}{\lambda_i} \tag{4.12}$$

(2) Derivation of Eq.(4.44)

The more detailed derivation of Eq.(4.44) was shown as the second line of the following equation.

$$\begin{aligned} \frac{\partial \overline{C_i}}{\partial t} &= \frac{\partial (f C_i + f_s \overline{C_{si}})}{\partial t} \\ &= \frac{\partial (f C_i)}{\partial t} + \left[\overline{C_{si}} \frac{\partial f_s}{\partial t} \right] + \left[f_s \frac{\partial \overline{C_{si}}}{\partial t} \right] \\ &\qquad\qquad \text{A} \qquad\quad \text{B} \\ &= \frac{\partial (f C_i)}{\partial t} + C_{si} \frac{\partial f_s}{\partial t} + \alpha_i f_s \frac{\partial C_{si}}{\partial t} \end{aligned}$$

A **:** The second parenthesis in the second line, denoted as A, represents the change of the mass of the solute *i* with respect to the change of f_s. This corresponds to the amount of the solute *i* discharged from the solid surface to liquid or taken into the solid from liquid to solid. The concentrations in the solid are not constant in the solid except the case of the rapid diffusion solute, *e.g*. carbon. However, only the surface region of the dendrite melts (or solidify). Therefore, the concentration of the solute *i* discharged

from the solid surface should be, C_{si}, or solidify as the solid of which the concentration is C_{si}. No solid with the averaged value, $\overline{C_{si}}$ melts or solidify. Accordingly, C_{si} is used in the place of $\overline{C_{si}}$ in the second parenthesis A as follows:

$$\overline{C_{si}} \frac{\partial f_s}{\partial t} = C_{si} \frac{\partial f_s}{\partial t}$$

B **:** As explained in the manuscript , α_i is a parameter having a value of 0 or 1 that defines the diffusion limits of the solute *i* in the solid (*i.e.*, α_i = 0 when the diffusion of the solute *i* in the solid is negligible and α_i = 1 when the diffusion of the solute *i* in the solid, such as the case of carbon, is rapid enough to result in homogeneous composition over distances in the order of the primary dendrite diameter).
For the case of rapid diffusion solute (*i.e.*, carbon), B is rewritten with $\alpha_i = 1$ (the concentration of carbon in solid is uniform),

$$f_s \frac{\partial \overline{C_{si}}}{\partial t} = f_s \frac{\partial (\alpha_C C_{sC})}{\partial t} = f_s \frac{\partial (C_{sC})}{\partial t}$$

For the case of the slow diffusion solute, *e.g.* Mn, Cr, Ni etc. with $\alpha_i = 0$,(neglecting the back diffusion in solid)

$$f_s \frac{\partial \overline{C_{si}}}{\partial t} = f_s \frac{\partial (\alpha_{\mathrm{Mn}} C_{s\mathrm{Mn}})}{\partial t} = 0$$

These equations can be rewritten as follows:

$$f_s \frac{\partial \overline{C_{si}}}{\partial t} = f_s \frac{\partial (\alpha_i C_{si})}{\partial t} = f_s \alpha_i \frac{\partial (C_{si})}{\partial t}$$

Accordingly, as shown herein, the third line of Eq.(4.44) is obtained with A and B.

Appendix 4.B

The error of the approximation of the erf(η), Eq.(4.64) is remained smaller than 0.2% for $\eta > 1.73$, 1% for $\eta > 1.39$, and 2% for $\eta > 1.24$.

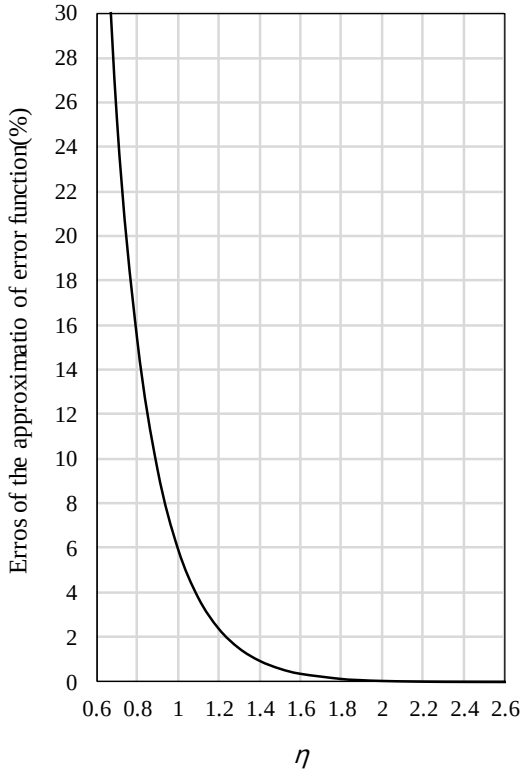

Fig.4A1 Error of the approximation of erf(η) used in the model.

Appendix 4.C

The process to obtain the set of unknown parameters (T^*, η_2^*, η_2°, and λ_i) of the multi-component system is basically same with the that of binary alloy model [26]. The left and right sides of (40) and (41) are denoted as A, B, and C (B is commonly used). The unknown parameters minimizing the aimed function Z defined as follows were sought:

$Z = (1-A/B)^2 + (1-C/B)^2$

$$A = \frac{K_1(T^* - T^s)\exp\left\{(1-\frac{\beta_2}{\beta_1})(\eta_2^*)^2\right\}}{(T^* - T^\circ)\mathrm{erf}(\sqrt{\frac{\beta_2}{\beta_1}}\ \eta_2^*)\sqrt{\beta_1}}$$

$$\mathrm{B} = \frac{K_2}{\left\{\mathrm{erf}(\eta_2^*) - \mathrm{erf}(\eta_2^\circ)\right\}\sqrt{\beta_2}}$$

$$\mathrm{C} = \frac{K_3(T^i - T^\circ)\exp\left\{(1-\frac{\beta_2}{\beta_3})(\eta_2^\circ)^2\right\}}{(T^* - T^\circ)\left\{1-\mathrm{erf}(\sqrt{\frac{\beta_2}{\beta_3}}\ \eta_2^\circ)\right\}\sqrt{\beta_3}}$$

$$\mathrm{D}: \quad \frac{\left\{1-\mathrm{erf}(\eta_2^\circ)\right\}}{\left\{\mathrm{erf}(\eta_2^*) - \mathrm{erf}(\eta_2^\circ)\right\}} = \frac{2(1-\mathrm{k}_i)}{(2-\mathrm{k}_i-\alpha_i\mathrm{k}_i)}\lambda_i C_i^\circ + \frac{(1+\alpha_i)\mathrm{k}_i}{(2-\mathrm{k}_i-\alpha_i\mathrm{k}_i)} - \frac{N_i}{M_i}$$

Note: N_i/M_i is neglected because $N_i << M_i$ in a general steel.

(1) First, the initial values for T^*, η_2^*, and η_2° are given. T^* calculated with the reported formula is used as the initial value for T^*. The initial η_2° was 1.0. η_2^* was given as $\eta_2^* = \gamma\eta_2^\circ$, where the initial γ = 0.3.

(2) Second, the η_2° is changed to minimize Z for the initial T^*. Convergence is quickly obtained.

(3) Then, η^* minimizing Z is obtained by changing γ ($\eta_2^* = \gamma\eta_2^\circ$).

(4) By substituting η_2^*, η_2° obtained by the above process to the left side of Eq.(4.69) provides λ_i (the left side of D: shown above). λ_i is obtained with same procedure. Substituting these λ_i into Eq. (4.12) yields the new T^*. Using this T^* as the initial T^* and repeating the same process mentioned above from Eq.(4.2) to (4.4) yields, the set of (T^*, η_2^*, η_2°, and λ_i) as the four Eqs. (4.12), (4.40), (4.41), and (4.69) match.

(5) This process is repeated until Z < 0.1, and the four decimal digits do not change in the analysis.

Appendix 4.D

The equivalent surface temperature that results the same amount of heat extraction of the continuously cast steel is roughly obtained assuming the step-wise decrease of the surface temperature T^s, where T^s is kept constant within a step as follows:

The temperature in solid is given as follows (Eq. (4.26)):

$$T = \frac{(T^* - T^s)}{\mathrm{erf}(\eta_1^*)}\mathrm{erf}(\eta_1) + T^s \qquad (4.A7)$$

where η_1 is given by

$$\eta_1 = \frac{x}{2\sqrt{\beta_1 t}} \tag{4.A8}$$

The heat extraction in a unit time from the surface (x = 0, η_1= 0) is given by Eq.(4.A7) and (4.A8) as follows:

$$q = -K_1 \left.\frac{\partial T}{\partial x}\right|_{x=0} = -K_1 \frac{(T^* - T^s)}{\mathrm{erf}(\eta_1^*)} \frac{1}{\sqrt{\pi\beta_1 t}} \tag{4.A9}$$

Integrating Eq.(4.A9) from t = 0 – t ° gives the total heat extraction Q^{real}

$$Q^{real} = \int_0^{t^\circ} q \, dt = -H \int_0^{t^\circ} \frac{(T^* - T^s(t))}{\sqrt{t}} dt \tag{4.A10}$$

where H is denoted as follows:

$$H = \frac{K_1}{\sqrt{\pi\beta_1}\,\mathrm{erf}(\eta_1^*)} \tag{4.A11}$$

In the case T^s is constant, the total heat extraction is obtained by Eq.(4.A10) as follows:

$$Q^{const} = -2H(T^* - T^s)\sqrt{t^\circ} \tag{4.A12}$$

The equivalent T^s is obtained by $Q^{const} = Q^{real}$ as follows:

$$T^s_{equivalent} = \frac{1}{2\sqrt{t^\circ}} \int_0^{t^\circ} \frac{T^s(t)}{\sqrt{t}} \, dt \tag{4.A13}$$

Referring the reported surface temperature by Meng et al. [47], the surface temperature of the continuously cast steel are estimated as follows:

t = 0 s T = 1753 K, t = 10.9 s T = 1573 K, t = 20.8 s T = 1543 K

t = 65.5 s T = 1513 K, t = 76.4 s T = 1453 K, t = 240. s T = 1373 K

Assuming the step-wise decrease of the surface temperature, the equivalent surface temperature, $T^s_{equivalent}$ which results the nearly same amount of heat extraction with the above continuously cast steel, is obtained as follows:

$$T^s_{equivalent} = 1420 \text{ K} \tag{4.A14}$$

In this model, T^s = 1423 K (=1150 +273 °C) has been adopted as the equivalent surface temperature, which results nearly same amount of the heat extraction during t = 0–240 s with the real continuously cast steel.

Appendix 4.E

The peritectic composition is estimated to be 0.15% by the nonequilibrium pseudobinary Fe-C diagram of 0.015%Si-1.05%Mn-0.0009%P-0.0008%S carbon steel. The partition ratio $k_C = 0.19$ was adopted in the low carbon range (C<0.15%). The γ -Fe begins to precipitate when the carbon concentration of the steel exceeds 0.15%, so that the partition ratio of carbon increases with the carbon concentration. On the other hand, η_2^* obtained with the model gradually decreases with an increase in the carbon concentration of the steel because an increase in the carbon concentration lowers T^* so that it lowers η_2^*, which represents the solidification rate at the solidus point. To minimize the approximation error of Eq.(4.64), the larger k_C is adopted in accordance with the increase of the carbon concentration of the steel. The error of the approximation remains less than 2%, as shown in Fig. 4A2.

The selected k_C is $k_C = 0.19$ [30]; C < 0.15%, $k_C = 0.225$ [31,32]; 0.15% ≤ C < 0.25%, $k_C = 0.25$ [32]; 0.25% ≤ C < 0.30% and $k_C = 0.29$ [33]; 0.30% ≤ C ≤ 0.35%.

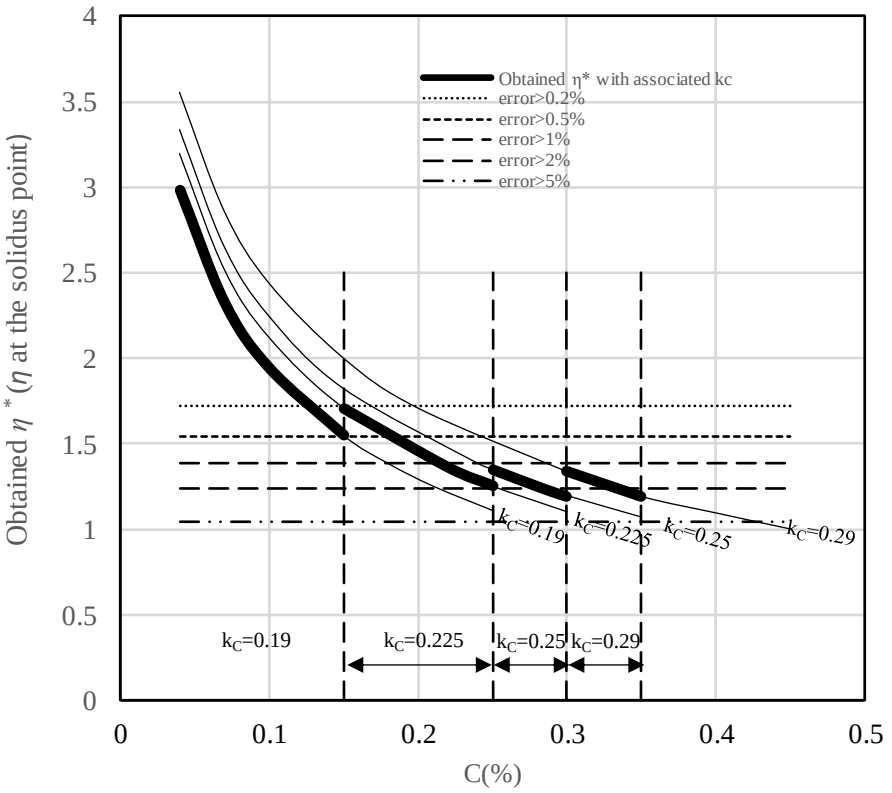

Fig. 4A2 The partition ratio of carbon k_C used in the model.

Appendix 4.F

The equilibrium solubility product of MnS of the liquid in a mushy zone is determined by Ueshima et al. [44] as follows:

$$\log[\%\mathrm{Mn}]\cdot[\%\mathrm{S}] = -10590/T + 4.302 - e_S^{Si}[\%\mathrm{Si}]$$

$$e_S^{Si} = 0.07$$

(1) Case of Steel K

Substituting the average temperature $(T^* + T^\circ)/2$ and the initial [%Mn] and [%Si] in the mushy zone of steel K, the maximum [S] concentration in a mushy zone is estimated as follows:

$$[\%\mathrm{S}]^{MnS} = 0.029\%$$

The solidus temperature drop (ΔT^*) due to the increase of the [S] concentration is estimated with the formula [15] in Eq. (4.1).

$$\Delta T^* = 1.1 \text{ K}$$

Note that the liquidus temperature drop due to the initial [S] concentration, 0.7 K obtained by the liquidus temperature formula [28] has been already accounted by this formula (the liquidus temperature dropped corresponding to the drop in the solidus temperature, as assumed in (7), section 4.2.1). Consequently, the extra solidus temperature drop due to [S] by not accounting [S] in the model is estimated to be 0.4 K.

This solidus temperature drop due to S by the formulas of Suzuki et al., [5] Kawawa et al., [3] and Hirai et al. [4], wherein the precipitation of MnS is not considered, are 0 K, 4.2 K, and 19.6 K, respectively.

(2) Case of Steel M

The maximum [S] concentration in a mushy zone is estimated as follows:

$$[\%\mathrm{S}]^{MnS} = 0.010\%$$

The solidus temperature drop (ΔT^*) due to the increase of the [S] concentration is estimated with the formula, [28], Eq. (4.1).

$$\Delta T^* = 0.4 \text{ K}$$

However, it is not necessary to take into account this extra solidus temperature drop, because the above $[\%\mathrm{S}]^{MnS}$ is much smaller than the initial [%S] = 0.029%, whereas the liquidus temperature drop due to the initial [S] has been already accounted in the model. Therefore, the solidus temperature drop due to [S] by not accounting [S] in the model is 0.4 K, which can be neglected. The solidus temperature drop due to [S] by the formulas of Suzuki et al. [5] Kawawa et al. [3], and Hirai et al. [4] where the precipitation of MnS is not considered are 0 K, 0.7 K, and 5.9 K, respectively.

(3) Case of Steel G1~3, S1~4, W11~W22

The precipitation of MnS is not expected and [S] was directly accounted in the model.

(4) Case of W31,32

The precipitation of MnS is expected and the solidus temperature were estimated with the consideration as shown in (1) and (2).

Appendix 4.G

Fig.4A3 shows the convergence of the predictions of the present model to the Neumann's solution at the early stage of the solidification (t=24s) at the low carbon concentration range (C=0.025%). It should be noted the solidus and liquidus temperature increase with decreasing of carbon concentration.

Meng and Thomas [47] demonstrated the precise model taking account the dynamic change of the heat flux in a mold due to the shrinkages and deformations of the thin shell. They calibrated their model with Neumann's solution (adopting T^s =1273K). They also compared the predictions by the numerical analysis (the predictions for the Wide Face and Narrow Face were made individually) with the measurements of the break out shells of the low carbon steel (Fig.4A4). In the numerical analysis, they assumed that the thickness of the break out shell corresponded d to the position where f_s =0.1. The drainage time of the molten metal from the shell was also accounted. The present model predictions were also compared with their measurements.

As can be seen in Fig.4A4, the predictions of the present model are in good agreement with the measurements and the predictions for the wide face by Meng and Thomas [47].

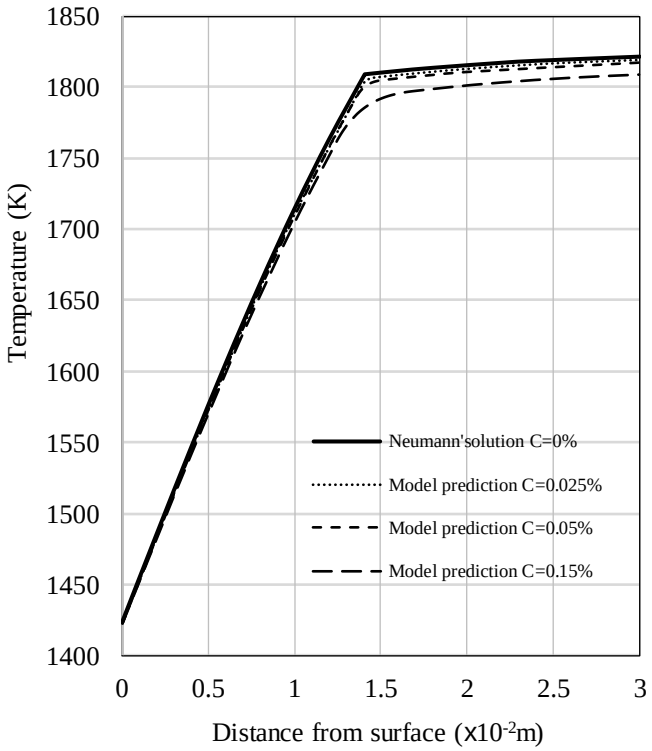

Fig.4A3 Transition of temperature predicted by the model and the Neumann's solution (C=0%, pure metal) of a continuously cast slab ($C:0-0.15\%, T^s=1423K, \Delta T=15K, t=24\sec$, slab thickness=0.22m) .

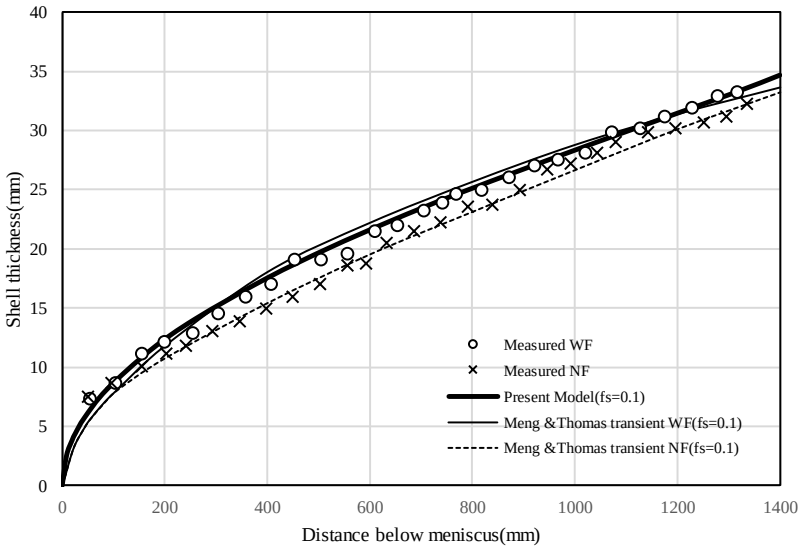

Fig. 4A4 The comparisons of the predicted shell thickness with the breakout shell thickness.

Size of slabs:0.25mx1.876m, casting speed:1.07m/min. T^s :1273K was adopted in the present model, WF and NF represent the wide face and the narrow face of the shell.

Appendix 4.H

The solidus temperature as a simultaneous solution of a multi-component alloy to the nonlinear solute- and heat-transfer equations is obtained as shown in the main text. The following formulas are the solidus temperatures that are within ±9 K of the real solutions. To minimize the approximation errors yielded by Eq. (4.64), the solidus temperatures are obtained in the different ranges of carbon with the corresponding carbon partition ratio. The influence of sulfur should not be accounted in these formulas when the precipitation of MnS is expected, as discussed in the main text (the extra solidus temperature drop due to [S] by not accounting [S] in the model is separately estimated, as shown in Appendix 4.F).

$$T^*(\mathrm{K}) = T_o + \mathrm{m_C}[\%C] + \mathrm{m_{Si}}[\%\mathrm{Si}] + \mathrm{m_{Mn}}[\%\mathrm{Mn}] + \mathrm{m_P}[\%\mathrm{P}] + \mathrm{m_S}[\%\mathrm{S}] + \mathrm{m_{Cr}}[\%\mathrm{Cr}] + \mathrm{m_{Ni}}[\%\mathrm{Ni}]$$

Carbon range	Adopted $\mathrm{k_C}$	T_o	$\mathrm{m_C}$	$\mathrm{m_{Si}}$	$\mathrm{m_{Mn}}$	$\mathrm{m_P}$	$\mathrm{m_S}$	$\mathrm{m_{Cr}}$	$\mathrm{m_{Ni}}$
0.04% ≤ C < 0.15%	0.19	1809.5	−354.4	−14.0	−7.8	−202.1	−510.0	−1.4	−4.6
0.15% ≤ C < 0.25%	0.225	1809.5	−310.0	−13.0	−7.8	−204.4	−550.4	−1.5	−4.6
0.25% ≤ C < 0.30%	0.25	1811.0	−289.3	−12.0	−7.9	−208.6	−593.1	−1.7	−4.6
0.30% ≤ C ≤ 0.35	0.29	1812.0	−257.5	−12.0	−8.2	−224.3	−619.0	−1.9	−5.3

(*) $\mathrm{m_S}$ is 0 for the case [%Mn] [%S] exceeds the solubility product of MnS (Appendix 4.F).

Appendix 4.I

The existence and the uniqueness of the solutions of the model are validated as follows:

The domain of η_2^*, η_2° is defined in the D defined in the theorems shown in Appendix 4.J.

(1) The existence and the uniqueness of the solutions of the heat balance equation.

The solution of the heat balance equation Eq.(4.27) is shown as Eq.(4.30). The existence and uniqueness of the solution can be shown with Eq.(4.59).

$$h_i(\eta_2) = \frac{dC_i}{d\eta_2} = \frac{(C_i^* - C_i^\circ)}{\left\{\mathrm{erf}(\eta_2^*) - \mathrm{erf}(\eta_2^\circ)\right\}} \frac{2\exp(-\eta_2^2)}{\sqrt{\pi}} \tag{4.59}$$

Because the initial conditions Eqs.(4.28) and (4.29) gives $\eta_2^* \neq \eta_2^\circ$, the real value L_h exists which satisfies Eq. (4.I1). Accordingly, the solution for the heat balance equation exists as the unique solution. (Appendix 4.J)

$$|h(\eta_2^*)-h(\eta_2^\circ)| = \left|\frac{(C_i^*-C_i^\circ)}{\left\{\mathrm{erf}(\eta_2^*)-\mathrm{erf}(\eta_2^\circ)\right\}}\frac{2\left\{\exp(-\eta_2^{*2})-\exp(-\eta_2^{\circ 2})\right\}}{\sqrt{\pi}}\right| \le L_h\left|C_i^*-C_i^\circ\right| \tag{4.I1}$$

(2) The existence and the uniqueness of the solutions of the mass balance equation.

Eq.(4.63) obtained by Eqs.(4.54) and (4.55) is shown as follows:

$$g_i(\eta_2)=\frac{dC_i}{d\eta_2}=-2\eta_2\left[\left[\frac{(C_i^*-C_i^\circ)\left\{\mathrm{erf}(\eta_2)-\mathrm{erf}(\eta_2^\circ)\right\}}{\left\{\mathrm{erf}(\eta_2^*)-\mathrm{erf}(\eta_2^\circ)\right\}}+C_i^\circ\right]F_i^\circ+G_i^\circ\right] \tag{4.63}$$

The term in the bracket of the right hand of Eq.(4.63) is denoted as A_i.

$$A_i=\left[\frac{(C_i^*-C_i^\circ)\left\{\mathrm{erf}(\eta_2)-\mathrm{erf}(\eta_2^\circ)\right\}}{\left\{\mathrm{erf}(\eta_2^*)-\mathrm{erf}(\eta_2^\circ)\right\}}+C_i^\circ\right]F_i^\circ+G_i^\circ \tag{4.I2}$$

Eq.(4.I3) is obtained by Eq.(4.3).

$$\lambda_i=\frac{1}{(C_i^\circ-C_i^*)} \qquad \text{where} \quad f=\lambda_i C_i+s_i,\ 1=\lambda_i C_i^\circ+s_i,\ 0=\lambda_i C_i^*+s_i \tag{4.I3}$$

The following equation is obtained by Eqs.(4.12) and (4.22).

$$\beta_2=\frac{K_2}{\rho_2 Cp_2+\dfrac{\rho_2 L}{(T^\circ-T^*)}}=\frac{K_2}{\rho_2 Cp_2+\dfrac{\rho_2 L}{\sum_j \dfrac{m_j}{\lambda_j}}} \tag{4.I4}$$

By the condition $\eta_2^* \neq \eta_2^\circ$ given by the initial conditions and the condition $M_i \neq 0$ assuming the diffusions of solutes in liquid are not negligible, the following parameters can be given as the real values.

$$F_i=\frac{(2-k_i-\alpha_i k_i)}{M_i}\beta_2-1 \tag{4.61}$$

$$G_i=\frac{s_i}{\lambda_i}\left\{\frac{(1-\alpha_i k_i)}{M_i}\beta_2-1\right\}+\frac{\alpha_i k_i \beta_2-N_i}{\lambda_i M_i} \tag{4.62}$$

$$M_i=\sum_j (E_{ij}-\alpha_j k_j D_{ij})\frac{\lambda_i}{\lambda_j} \tag{4.52}$$

$$N_i = \sum_j \alpha_j k_j D_{ij}) \frac{\lambda_i}{\lambda_j} \tag{4.53}$$

It is noted that E_{ij} can be obtained as the real values which satisfies $A_{i.}$=0, while $(T^\circ - T^*)$,i.e. λ_j in Eq.(4.I4) has not been yet obtained at this moment*1). The real value L_i exists which satisfies Eq.(4.I5).

It is also noted that even for the large η_2^*, η_2°, the real value L_i exists which satisfies Eq.(4.I5).

$$|g(\eta_2^*) - g(\eta_2^\circ)| = \left|-2(\eta_2^* - \eta_2^\circ)\cdot A_i\right| \le L_i \left|C_i^* - C_i^\circ\right| \tag{4.I5}$$

Accordingly, the unique solution for Eq.(4.63) exists (Appendix 4.J).

*1) $(T^\circ - T^*)$ and E_{ij} are obtained under the condition that Eqs.(4.59)and (4.63) becomes approximately equal by the approximation Eq.(4.64) in the model.

(3) <u>The existence and the uniqueness of the solutions of the simultaneous equations of the heat and mass balance equations.</u>

Eqs.(4.I1) and (4.I5) gives Eq.(4.I6).

$$\left|h(\eta_2^*) - h(\eta_2^\circ)\right| + \left|g_j(\eta_2^*) - g_j(\eta_2^\circ)\right| \le L_h \left|C_i^* - C_i^\circ\right| + L_i \left|C_i^* - C_i^\circ\right| \le L \left|(C_i^* - C_i^\circ)\right| \tag{4.I6}$$

It is obvious that the real value L which satisfies Eq.4.I6 exists.

Thus, accordingly, the existence of the real value L which satisfies the Lipshitz's condtion (Appendix 4.J) shows the existence of the unique solution for the simultaneous equations for the heat and mass transfer equations.

Appendix 4.J

(1) <u>Theorem of the existence and the uniqueness of the solution for the ordinary differential equation</u>

g(*x,y*) is defined as the continuous function. The differential equation J1 is defined in the square domain D.

$$dx/dy = g(x,y) \quad (x,y) \in \mathrm{D} \tag{4.J1}$$

where

$$\mathrm{D} = \left\{(x,y) \mid |x - x_\circ| \le r, |y - y_\circ| \le s\right\} \tag{4.J2}$$

The unique solution, $y = \varphi(x)$, exists which satisfies the initial condition $\varphi(x_\circ) = y_\circ$ in the region($x_\circ$ -r', $x_\circ$ +r'), if g(x,y) satisfies the Lipschitz's condition.

< Lipschitz's continuity condition(Lipschitz's condition) [58] >

The real value L exists for the arbitrary two positions $(x_1,y_1),(x_2,y_2)$ in D

$$| g(x, y_1) - g(x, y_2) | \leq L | y_2 - y_1 | \qquad (4.J3)$$

(2) Theorem of the existence and the uniqueness of the solution for the simultaneous differential equations

$g_1(x, y_1, y_2, ..., y_n), g_2(x, y_1, y_2, ..., y_n), ..., g_n(x, y_1, y_2, ..., y_n)$ are defined as the continuous function for the (n+1) variables, $x, y_1, y_2, ..., y_n$. D is defined as the hyper rectangular around the point $x^\circ, y_1^\circ, y_2^\circ, ..., y_n^\circ$.

$$\mathrm{D}=\{(x, y_1, y_2, ..., y_n) \mid |x - x^\circ| \leq r, | y_1 - y_1^\circ | \leq s, | y_2 - y_2^\circ | \leq s, .., | y_n - y_n^\circ | \leq s\} \qquad (4.J4)$$

The following simultaneous differential equations are defined in D.

$$\begin{aligned} dy_1 / dx &= g_1(x, y_1, y_2, ..., y_n) \\ dy_2 / dx &= g_2(x, y_1, y_2, ..., y_n) \\ &\vdots \\ dy_n / dx &= g_n(x, y_1, y_2, ..., y_n) \\ (x, y_1, y_2, ..., y_n) &\in \mathrm{D} \end{aligned} \qquad (4.J5)$$

The unique solution $(y_1, y_2, ..., y_n)$ which satisfies the initial conditions $y_1(x^\circ) = y_1^\circ, y_2(x^\circ) = y_2^\circ, ..., y_n(x^\circ) = y_n^\circ$ exists in the region $(x^\circ - r', x^\circ + r')$, if the real values L exists to satisfies the Lipschitz's condition for Eq.(4.J6).

< Lipschitz's continuity condition (Lipschitz's condition) for the simultaneous differential equations [58] >

The real values L exists for the arbitrary integer $1 \leq j \leq n$ and for the arbitrary points $(x, Y_1, Y_2, ...Y_n)$ and $(x, y_1, y_2, ...y_n)$ in D.

$$| f_j(x, Y_1, Y_2, ...Y_n) - f_j(x, y_1, y_2, ...y_n) | \leq L(| Y_1 - y_1 | + | Y_2 - y_2 | + \cdots + | Y_n - y_n |) | \qquad (4.J6)$$

References

[1] T. Kawawa, H. Sato, S. Miyahara, T. Koyano and H. Nemoto, Determination of Solidifying Shell Thickness of Continuously Cast Slab by Rivet Pin Shooting, Tetsu-to-Hagane 60 (1974) 206–216.

[2] J.C. Crepeau, A. Siahpush and B. Spotten, On the Stefan Problem with Volumetric Energy Generation, Heat Mass Transf. 46 (2009) 119–128.

[3] T. Kawawa and H. Tuchida, Tekko-no-Gyouko (Solidification of steel), Appendix 4, ed. By Solidification Comm., Joint Sc. on Iron and Steel Basic Research of ISIJ, ISIJ, Tokyo, 1977.

[4] M. Hirai, K. Kanamaru and H. Mori, Tekko-no-Gyouko (Solidification of steel), Appendix 4, ed. By Solidification Comm., Joint Sc. on Iron and Steel Basic Research of ISIJ, ISIJ, Tokyo, 1977.

[5] A. Suzuki, T. Suzuki, Y. Nagaoka and Y. Iwata, On Secondary Dendrite Arm Spacing in Commercial Steels Having Different Carbon Contents, J. Jpn. Inst. Met. 32 (1968) 1301–1305.

[6] K. Gryc, B. Smetana, M. Zaludova, K. Michalek, P. Klus, M. Tkadleckova, L. Socha, J. Dobrovska, P. Machovcak, L. Valek, R. Pachlopnik and B. Chmiel, Determination of the Solidus and Liquidus Temperatures of the Real-Steel Grades with Dynamic Thermal-Analysis Methods, Mater. Technol. 47 (2013) 569–575.

[7] E.A. Mizikar, Mathematical Heat Transfer Model for Solidification of Continuously Cast Steel Slabs, Trans. AIME 239 (1967) 1747–1753.

[8] J. Szekely and V. Stanek, On Heat Transfer and Liquid Mixing in the Continuous Casting of Steel, Metall. Trans. 1 (1970) 119–126.

[9] J. Matsuno, H. Nakato and H. Ohi, An analysis of Solidification Rate and Surface Temperature of Continuous Casting Slabs, Tetsu-to-Hagane 60 (1974) 1023–1032.

[10] Y.K. Chaung and K. Schwerdfeger, Experimentelle und Theoretische Untersuchung der Erstarrung einer Eisen-Kohlenstoff-Legierung mit 0.6%C, Arch. Eisenhüttenwes 44 (1973) 341–347.

[11] P.H. Shingu, K. Takeshita, R. Ozaki and T. Akiyama, An analysis of the Solidification of a Binary Eutectic System Considering Temperature and Solute Distribution, J. Jpn. Inst. Met. 42 (1978) 172–179.

[12] H.D. Brody and M.C. Flemings, Solute Redistribution during Dendritic Solidification, Trans. Met. Soc. AIME 236 (1966) 615–624.

[13] T.W. Clyne and W. Kurz, Solute Redistribution during Solidification with Rapid Solid State Diffusion, Met. Trans. 12A (1981) 965–971.

[14] I. Ohnaka, Mathematical Analysis of Solute Redistribution during Solidification with Diffusion in Solid Phase, Trans. ISIJ 26 (1986) 87–96.

[15] V.R. Voller and C. Beckerman, Approximate Models of Microsegergation with Coarsening, Metall. Trans. A 30A (1999) 3016–3019.

[16] Y.M. Won and B.G. Thomas, Simple Model of Microsegregation during Solidification of Steels, Metall. Mate. Trans. A 32A (2001) 1755–1767.

[17] I. Ohnaka and T. Fukusako, Calculation of Solidification of Castings by a Matrix Method, Trans. Iron Steel Inst. Jpn. 17 (1977) 410–418.

[18] K. Kumai, A. Sano, T. Ohashi, E. Nomura and H. Fujii, Study on Solidification Behavior, Solute Segregation and Fluid Flow in Continuously Cast Slab, Tetsu-to-Hagane 7 (1974) 894–914.

[19] S. Asai and I. Muchi, Analysis of Effective Distribution Coefficient Based of Transport Phenomena in Liquid and Solid Region, Tetsu-to-Hagane 64 (1978) 1685–1692.

[20] R.N. Hills, D.E. Looper and P.H. Roberts, A Thermodynamically Consistent Model of a Mushy Zone, Q. J. Mech. Appl. Math. 36 (1983) 505–539.

[21] D.V. Alexandrov, Solidification with a Quasi-Equilibrium Mushy Region: Exact Analytical Solution of Nonlinear Model, J. Crystal Growth 222 (2001) 816–821.

[22] K. Takeshita, An Analysis of the Solidification of a Binary Eutectic System in Consideration of Both Heat and Solute Diffusion, J. Jpn. Inst. Met. 47 (1983) 647–653.

[23] H.E. Huppert and M.G. Worster, Dynamic Solidification of a Binary Melt, Nature 314 (1985) 703–707.

[24] D.V. Alexandrov and V.P. Malygin, Self-Similar Solidification of an Alloy from a Cooled Boundary, Int. J. Heat Mass. Transf. 49 (2006) 763–769.

[25] T. Fujimura and J.K. Brimacombe, Mathematical Analysis of Solidification Behavior of Multicomponent Alloys, Trans. Iron Steel Inst. Jpn. 26 (1986) 532–539.

[26] T. Fujimura, K. Takeshita and R.O. Suzuki, Mathematical Analysis of the Solidification Behavior of Plain Steel Based on Solute- and Heat- Transfer Equations in the Liquid-Solid zone, Metall. Mate. Trans. B 49 (2018) 644–657.

[27] H.S. Carslaw and J.G. Jaeger, Conduction of Heat in Solids, 2nd ed., Oxford University Press, New York, Tronto, Tokyo, 1959, 283–291.

[28] T. Kawawa, Tekko-no-Gyouko (Solidification of steel), Appendix 4, ed. By Solidification Comm., Joint Sc. on Iron and Steel Basic Research of ISIJ, ISIJ, Tokyo, 1977.

[29] S. Kato and H. Yoshida, Tekko-no-Gyouko (solidification of steel), The Micro Segregation of SUS310S Continuously Cast SUS310S steel, ed. By Solidification Comm., Joint Sc. on Iron and Steel Basic Research of ISIJ, ISIJ, Tokyo, 1977, 61–63.

[30] Tekko-Binran (Handbook for steel), 3rd ed., ISIJ, Maruzen, Tokyo, 1981, vol. 1, 193–194.

[31] C.E. Sims, Electric Furnace Steelmaking, vol. 2, John Wiley & Sons, New York, NY, 1962, 99.

[32] W.A. Tiller, Solute Segregation during Ingot Solidification, J. Iron Steel Inst. 192 (1959) 338–350.

[33] W.A. Fisher, H. Splizer and M. Hishinuma, Das Zonenschmelzen von Eisen und die Ermittlung der Verteilungskoeffizienten für Kohlenstoff, Phosphor, Schwefel und Sauerstoff, Arch. Eisenhüttenwes. 31 (1960) 365–371.

[34] Tekko-no-Gyouko (solidification of steel), Supplement, Solidification Comm., Joint Sc. on Iron and Steel Basic Research of ISIJ, ISIJ, Tokyo, 1977.

[35] A. Hays and J. Chipman, Mechanism of Solidification and Segregation in a Low-Carbon Rimming -Steel Ingot, Trans. Met. Soc. AIME 135 (1938) 85.

[36] J. Chipman, Basic Open-Hearth Steelmaking, Physical Chemistry of Steelmaking Committee, Iron and Steel division, AIME, 1951, 632.

[37] D.F. Kalinovich, I.I. Kovenskii and M.D. Smolin, Carbon State in Austenite with 0, 4 and 0, 6 Weight Percent Content of C, Izv. Vyssh. Ucheb. Zaved., Fiz. 9 (1971) 116.

[38] J.S. Kirkaldy, R.N. Smith and R.C. Sharma, Diffusion of Manganese in Paramagnetic BCC Iron, Met. Trans. 4 (1973) 624–625.

[39] G. Seibel, Metallographie-Diffusion du Phosphore Dans le fer, Compt. Rrend. 256 (1963) 4661–4664.

[40] J.H. Swisher, Sulfurization Kinetics of Delta Iron at 1410 C, Trans. AIME 239 (1967) 110–113.

[41] T. Mitsuo, T. Horigome, S. Saito, E. Nomura, Y. Kitamura and R.Kono, On the Accumulation Mechanism and Reducing Process of Large Non-metallic Inclusions in the Bottom Equiaxed Zone of

Ingots, Tetsu-to-Hagane, 57 (1971) 915-941.

[42] H. Nomura, Y. Tarutani and K. Mori, Mathematical Model of Formation of Segregation Zone Caused by Volume Change in Solidification of Iron Steel, Tetsu-to-Hagane, 67 (1981) 1449-1461

[43] R.D. Phelke, A. Jeyarajan and H. Wada, Summary of Thermal Properties for Casting Alloys and Mold Materials, Grant DAR78-26171, The university of Michigan-National Science Foundations, Applied research division, Dec.1982

[44] J.S. Kirkaldy and E. Baganis, Thermodynamic Prediction of the Ae_3 Temperature of Steels with Additions of Mn,Si,Ni,Cr,Mo,Cu, Metall.Trans. 9A (1978) 495-501.

[45] Y. Ueshima, H. Yuyama, S. Mizoguchi and H. Kajioka, Effect of Oxide Inclusions on MnS Precipitation in Low Carbon Steel, Tetsu-to-Hagane 75 (1989) 501–508.

[46] F. Kurosawa and I. Taguchi, Precipitation Behavior of Phosphides in the Centerline Segregation Zone of Continuously Cast Steel Slabs, J. Jpn. Inst. Met. 50 (1986) 89–97.

[47] Y.A. Meng and B.G. Thomas, Heat-Transfer and Solidification Model of Continuous Slab Casting: CON1D, Metall. Mate. Trans. B34 (2003) 685–705.

[48] D. You, C. Bernhard and G. Wieser, S. Michelic, Microsegregation Model with Local Equilibrium Partition Coefficients during Solidification of Steels, Steel Res. Int, 87 (2016) 840–849.

[49] K. Katayama, S. Hattori, A Study of Heat Transfer with Freezing, Trans. Japanese Soc. Mech. Eng. 40(1974) 1401-1411.

[50] R.E. Grace and G. Derge, Diffusion of Third Elements in Liquid Iron Saturated with Carbon, Trans. Metall. Soc. AIME 212 (1958) 313–337.

[51] T. Mori, K. Ayata, J. Fujisawa and H. Sako, Temperature and Thermal Stress in the Solidifying Shell of the Continuously Cast Steel, Tekko-no-Gyouko (Solidification of steel), ed. By Solidification Comm., Joint Sc. on Iron and Steel Basic Research of ISIJ, ISIJ, Tokyo, 1977, 237–239.

[52] D.J. Soel, Y.M. Won, K. Hwan OH,Y.C.Shin and C.H.Yim, Mechanical Behavior of Carbon Steels in the Temperature Range of Mushy Zone, ISIJ international 40 (2000) 356-363.

[53] G. Shin, T. Kajitani, T. Suzuki and T. Umeda, Mechanical Properties of Carbon Steels during Solidification, Tetsu-to-Hagane 78 (1992) 587–593.

[54] E. Schmidtmann and F. Raoski, Bnfluß des Kohlenstoffgehaltes von 0,015 bis 1% und der

Gefügestruktur auf das Hochtemperaturfestigkeits-und-Zähigkeitsverhalten von Baustählen nach der Erstarrung aus der Schmelze, Arch. Eisenhüttenwes. 54 (1983) 357–362

[55] A Guide to the Solidification of Steels, Jernkontret, Stockholm, 1977.

[56] B.Smetana,M.Kawuloková,S.Zlá,A.Kalup,M.Strouhalová,L.Řeháćková,S.Rosypalová,M.Tkadlečková,K. Michalek and J. Dobrovská, Comparison of Solidus and Liquidus Temperature of Real Low Carbon Steel Grade Obtained by Use of Thermal Analysis Methods, Prace Instytutu Metalurgii Żelaza nr 2/2016, 68,33-39.

[57] A.A.B. Sugden and H.K.D.H. Bhadeshia, Thermodynamic Estimation of Liquidus, Solidus, Ae_3 Temperatures, and Phase Compositions for Low Alloy Multicomponent Steels, Materials Science and Technology 5 (1989) 977-984.

[58] Kouji Kasahara, Basis of the Differential Equation, Asakura Publishing Co.,LTD, Tokyo,1982

Chapter 5

Effect of Stirring on Crystal Morphologies and on Macro-Segregation

Abstract

To minimize the macro-segregation in continuously cast steel slabs, the effects of the stirring on the macro-segregation were studied. Industrial findings by the metallographic observations of the steel slabs showed macro-segregation was improved by the refinements of crystals. It was also found that the stirring at low fraction solid refined crystals. The unsolidified liquid core of the continuously cast slab with the optimum stirring was well packed with the refined crystals whereas it was not with coarse equiaxed crystals. The analogue study with experiments of Pb-Sn alloy showed, similarly as with steel slabs, the stirring at low solid fraction refined crystals. Also, the artificially created cavity in a mush was well packed with the refined, globular, crystals whereas it was not with the coarse dendritic crystals. Thus, it is considered the stirring at the low solid fraction is advantageous to refine crystals and to improve macro-segregation.

5.1 Introduction

The goal of continuously casting slabs with homogeneous composition is difficult to achieve owing to the strong tendency for elements such as phosphorous, sulfur and manganese to segregate. The segregation may appear on the “micro” scale between dendrite arms or on the larger “macro” or semimacro” scale. Macro and Semimacro-segregation are particularly undesirable in slabs for plate application because they may give rise to welding cracks, ultrasonic-inspection defects, hydrogen-induced cracks [1]. Ohashi et al. [2] reported the precipitated MnS inclusion deteriorated both the ductile fracture and brittle fracture of the steel plate. It was also found that manganese and phosphorous in the segregated region of the steel plate decreased the nil-ductility transition temperature in notch tensile tests due to the transformation to the multensite-bainite duplex structure [3]. The hydrogen induced cracks are also induced by the segregations of manganese and phosphorous [3]. The macro- or semimacro- segregations appear at the centerline or as spots distributed in the central region in continuously cast slabs. Macro-segregation is caused by liquid movement in the semi-solid mush during the solidification process; in the interior of slabs it is influenced by the morphology and packing of crystals, and electromagnetic stirring below the mould [4,5,6].

The objectives of this study are to elucidate the influence of the crystal morphology on macro segregation based on the industrial findings and the analogue study with Pb-Sn alloy.

5.2 Macro Segregation in the Interior of Slabs

Macro-segregation in the interior continuously cast slabs is influenced by the shape pf crystals freely moving in the liquid pool and by the closeness of packing of crystals as they settle under the influence of gravity to the bottom of the sump. Coarse dendritic crystals, for example, do not pack closely, as compared to fine "globular" (more equiaxed) crystals, leaving relatively large pockets of liquid in which elements such as manganese, phosphorous and sulphur may segregate during solidification [5]. Bulging of the slabs near the point of final solidification also is a major factor in the formation of centerline segregation as interdendritic liquid is drawn into the void created by the bulging action.

The influence of stirring on the refinement of crystal shape and macro-segregation were investigated with aid of a Pb-10% Sn alloy analogue of steel [5].

5.2.1 Industrial Findings

The specifications of the casting machine and the conditions under which the industrial trials were conducted are presented in Table 5.1. It may be noted that stirrers were located at two positions beneath the mould, 5.4 and 10.4m below the meniscus respectively. In the test, the casting speed was varied so that the thickness of the solid shell, or fraction of unsolidified core remaining, change at the stirrer position. The liquid core fraction, fc, defined as the ratio of the thickness of the unsolidified zone between the upper and bottom side of white bands, caused by the liquid flow by EMS, relative to the slab thickness, could be determined directly by measuring the position of the white bands in transverse sections of fully solidified slabs [4]. The effect of liquid core fraction, f_C at the No.2 stirrer, on centerline segregation was shown in Fig. 5.1 [4,5]. Thus it is seen that centerline segregation, expressed as an index (I.C.S. = area at the centerline occupied by segregated solutes/overall length of centerline length), is nearly the same with either both No.1 and No.2 stirrers or solely No.2 stirrer. This suggest that the No.1 stirrer is not as effective in changing the macro-segregation as the No.2 stirrer. It also is observed that the centerline segregation is a minimum when the liquid core fraction, f_C is about 0.2. It is considered, hence, that the stirring at fc=0.2 which corresponds to low fraction solid in liquid core is

effective to refine crystals, whereas the stirring at fc=0.07 which corresponds to the high solid fraction in liquid core is not.

To improve the susceptibility to Hydrogen Induced Cracking (HIC) in the steel plates for line pipe use, the solutes distributions in the transverse section (samples of 4x4cm^2, were taken from the central region of continuously cast slabs) were investigated. The extent of the segregations of manganese and phosphorous in the samples were measured by an EPMA Macroanalyzer with the 100μm diameter beam. The points of measurements to cover 4x4cm^2 section was 64x10^4. The maximum concentrations relative to those of bulk liquid decreased with the decrease of the sizes of semimacro-segregation spots, as shown in Fig.5.2. It is seen that stirring at fc=0.2 is advantageous to decrease the sizes of spots which results the decrease of the maximum concentration ratio of manganese and phosphorous in semimacro-segregation spots. Fig.5.3 shows the influence of the liquid core ration fc on the sizes of the spots, semimacro-segregations distributed in the central region of continuously cast steel slabs. It is seen that the number of the spots, semimacro-segregations with the diameter more than 1 x10^{-1} cm decreases with the decrease of fc.

Thus, it is considered that the stirring at fc=0.2 is more effective than that at fc=0.3 or fc=0.37 to refine crystals and reduce the maximum concentrations of manganese and phosphorous in the segregated spots. It is noted that this results are consistent with the results of I.C.S. in the range of the higher fc more than 0.2 (Fig. 5.1).

Thus, hence, it is considered that the refinement of crystals to obtain closer packing of crystals and smaller semimacro-segregation spots between crystals. It may be noted that the susceptibility to HIC can be improved by decreasing the phosphorous concentration of bulk liquid as to the minimum level of 0.005% [7] which may not be always available in the general mass production process. Thus, the efforts to minimize the macro- or semimacro- segregation in continuously cast slabs should be necessary.

A detailed metallographic study [4,5] was made of changes to crystal morphology in the center region of slabs cast with EMS as shown in Fig.5.4. Both crystals in B(f_C=0.2) and C(f_C=0.37) are refined and more globular than those in A (f_C=0.07). This revealed that, depending on the casting speed, No.2 EMS had the effect of changing crystal morphology from coarse dendritic to a finer globular shape. The influence of the casting speed on the thickness of the refined crystals in the core of the slab and the positions of the zone of refined crystals are shown in Fig.5.5. Thus, the strongest influence of stirring (No.2 EMS) on crystal refinement was found at casting speed 1 m/min (f_C=0.2). Below 0.9m/min (typically 0.7m/min, fc=0.07), there is virtually no refinement of crystal morphology by EMS. The refined crystal zone is seen to be displaced toward the lower side of the slab due to descending crystals settling into the curved liquid cavity. As a results, a vertical symmetry on

crystal structure at 1.0 m/min (fc=0.2) is lost at the higher casting speed (*e.g.* at 1.3 m/min(fc=0.37)), so that the upper side of liquid core is not sufficiently filled with refined crystals as compared to that at 1.0 m/min(fc=0.2). Thus, it is considered that the stirring at fc=0.2 which corresponds to low fraction solid in liquid core is effective to refine crystals and desirable to obtain a symmetry on crystal structure.

These findings are summarized as follows:

(1) The electromagnetic stirring EMS at fc=0.2 minimize the Index of Centerline segregation, I.C.S. (Fig. 5.1).

(2) The refinements of crystals are obtained when fc is larger than 0.2 and is not when fc is smaller than 0.2 (e.g. fc=0.07), so that the stirring at fc≥0.2 is essential to refine crystals (Fig. 5.4 and 5.5).

(3) The sizes of macro- or semimacro- segregation spots decrease with the decrease of fc (Fig. 5.2).

(4) (2) and (3) suggest that the extents of manganese and phosphorous of macro- or semimacro segregation spots are minimized by the stirring at fc=0.2.

(5) (4) and (1) are consistent each other.

Table 5.1 Principal specifications of the caster and test conditions

Item		Specification
Machine specification	Machine type	Vertica-Progressive bending-progressive unbending
	Length of vertical supporting	3000mm
	Metallurgical length	36.5m
Casting conditions	Slab size	230x1300mm
	Casting velocity	0.7-1.3m/min
	Superheat	18-40℃
	Chemical composition of the cast steel	0.12-0.18%C,0.014-0.024%Si, 0.55-0.80%Mn,0.009-0.023%P, 0.007-0.016%S
EMS conditions	Stirrer type	Linear mortar type
	Stirring direction	Horizontal
	Frequency	0.3-3.0 Hz
	Distance from the meniscus	No.1 EMS 5.4m No.2 EMS 10.4m

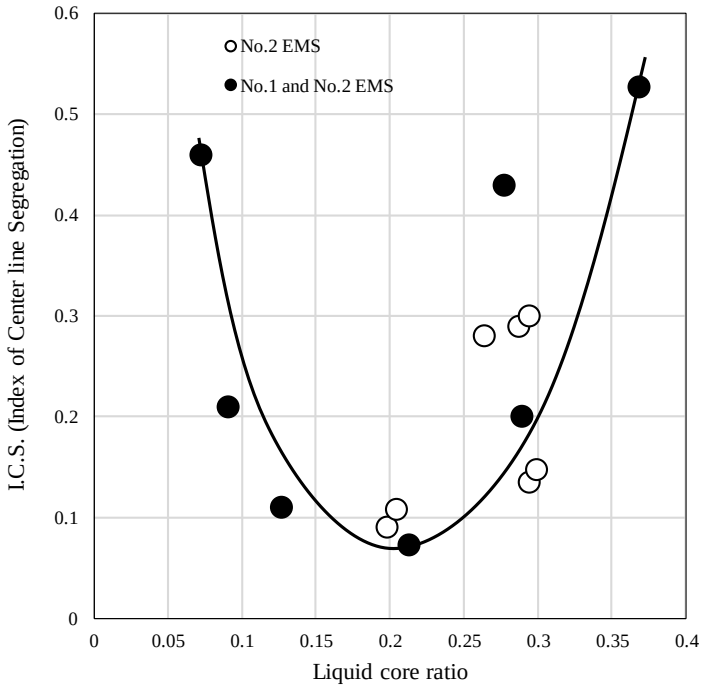

Fig. 5.1 Effect of the liquid core ratio of the slabs where liquid core was stirred by No.2 EMS [4,5].

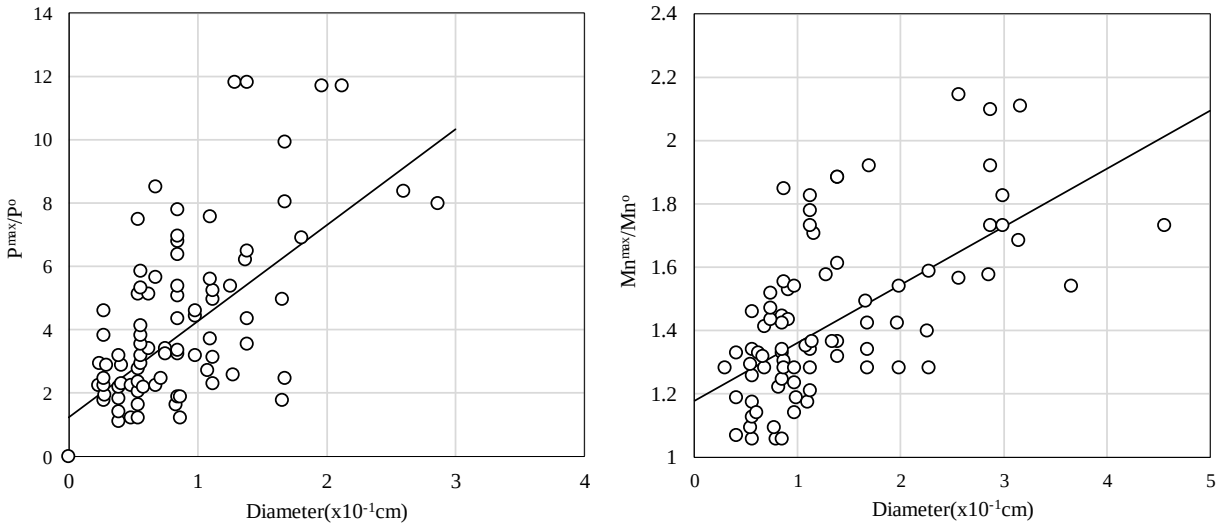

Fig. 5.2 Relations between the extents of maximum concentration of solutes and diameters of the semimacro segregation. Measure by the EPMA Macro analyzer with 100μm beam.

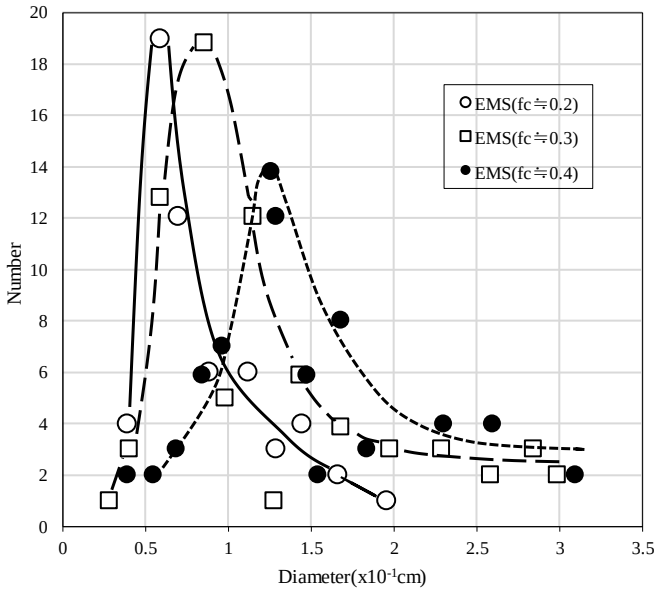

Fig. 5.3 Effect of the liquid core ratio of the slabs where liquid core was stirred by No.2 EMS on the sizes of semi-macro- segregations (spots distributed in central region of continuously cast slabs).

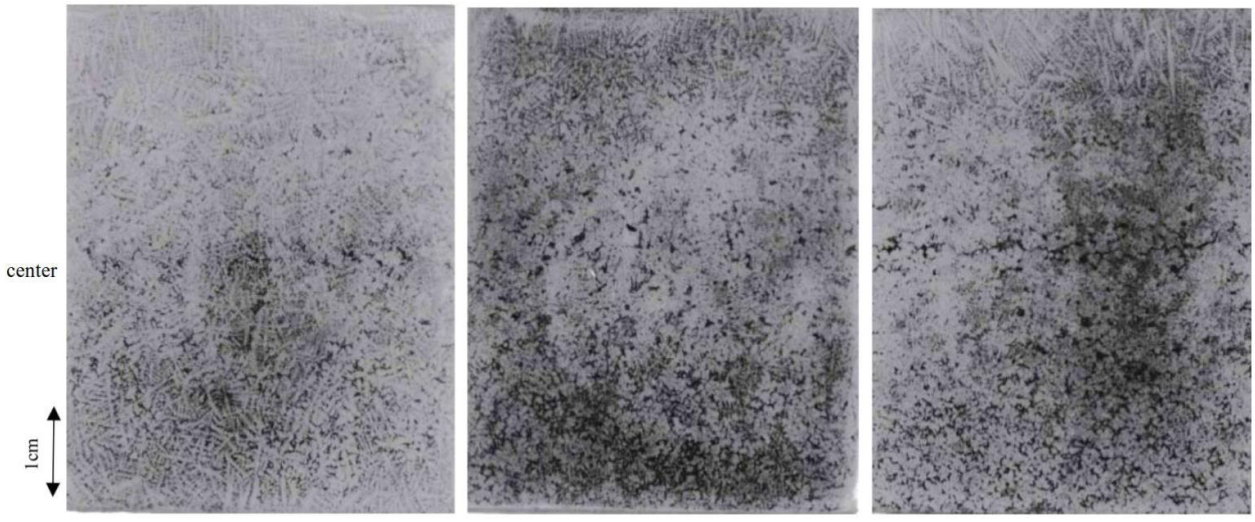

A (fc=0.07) B (fc=0.2) C (fc=0.37)

Fig. 5.4 Crystal morphologies in the transverse sections of the continuously cast slab stirred by EMS at the different liquid core ratio (Chemical composition: 0.12-0.18%C,0.014-0.024%Si, 0.55-0.80%Mn,0.009-0.023%P, 0.007-0.016%S, Casting speed 0.7-1.3m/min).

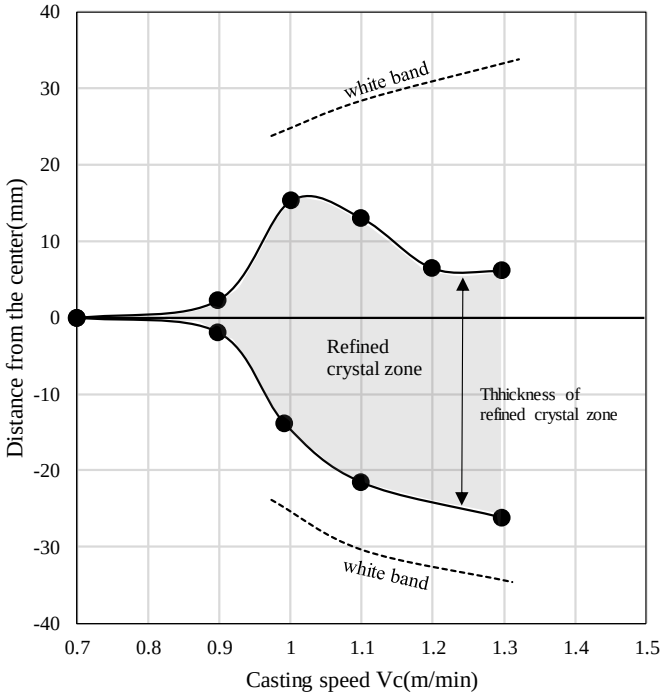

Fig. 5.5 Influence of the casting velocity on the positions of the central zone of refined crystal zone and white bands induced by No.2 EMS [5].

5.2.2 Analogue Study with Mechanical Stirring

The effect of mechanical stirring on crystal morphology and macro-segregation was studied in the laboratory using the rotary furnace shown in Fig. 5.6 [5]. The furnace was resistively heated and was rotated at a speed of 125 r.p.m. A mould shown in Fig. 5.7. was located inside the furnace. The mould was constructed of stainless steel, coated with carbon paste and was capable of disassembly to release the solidified ingot of Pb-10%Sn used as the metal analogue. The Phase diagram of Pb-Sn binary alloy [8] is shown in Fig. 5.8. The bottom of the mould also was fitted with a plunger which could be withdrawn partially prior to complete solidification of the ingot to simulate the action of slab bulging or solidification shrinkage.

In the experiments, molten alloy was cooled at 2℃/min and below 350℃ tumbled to the desired test temperature in solid -liquid region. The cooling rate below the liquidus temperature (300℃) was 0.5℃/min. The temperature then was held constant and tumbling was continued for various times. Finally, tumbling was stopped for 180s to permit the crystals to settle and thereafter the plunger rod was pulled downward to create an artificial cavity in the sedimented crystal zone. After another 180s the mould was water quenched; The Pb-

Sn ingot subsequently was sectioned axially, polished, etched and examined with respect to crystal morphology. Typical examples are shown in Fig. 5.9: Both of sample E and K were cooled stationary, but K was tumbled from 294°C to 289°C(fs=0.4-0.7) and sample D were continuously tumbled from 300°C(fs=0) to 294°C(fs=0.4).

It was found that crystal refinement was achieved by mechanical stirring (tumbling) when the fraction solid was less than 0.4(Sample D in Fig. 5.9). It was also found that the dendritic crystals precipitated in the low faction solid (fs is 0 to 0.4) are hardly refined by the mechanical stirring (Sample K in Fig. 5.9). This can be seen also in Figure 10. The fraction of solid was estimated by the lever rule because the liquid and solid were fully mixed by tumbling under slow cooling rate. It may be noted, in the range of low solid fraction, those estimated with lever rule were roughly consistent with the estimates by Scheil's equation (the partition ratio of tin, k_{Sn}=0.55, can be used as the averaged the equilibrium partition ratio of Pb-10%Sn alloy). Thus, it is considered that the stirring at low solid fraction (fs<0.4) is essential to refine crystals.

With respect to packing/macro-segregation, the fine, globular shape, crystals generated by tumbling were found to occupy the void created by the withdrawn plunger (Sample D and G). However unrefined coarse dendritic crystals did not behave similarly but remained stationary and only inter-dendritic liquid filled the cavity to create a pocket of macro-segregation (Sample E and K) as shown in Fig. 5.10.

Clearly the fine globular crystals are desirable both from the standpoint of packing and minimization of macro-segregation. It may be noted that when the artificial cavity was created with solid fraction greater than 0.75 neither crystals (of any shape) nor inter-dendritic liquid moved to fill it. This finding agrees well with results reported for steel by Takahashi et al. [9].

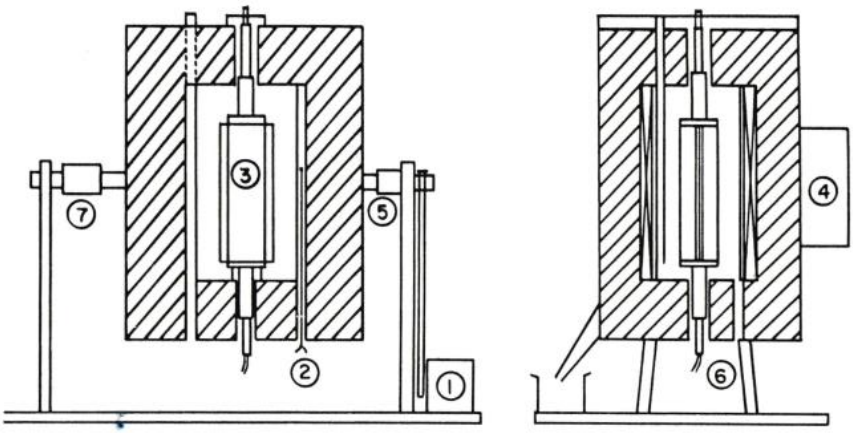

Fig. 5.6 Scematic diagram of rotary furnace: (1) motor (2)chromel-alumerl thermocouple (3) mould (4) ice cold junction (5) water inlet (6) water outlet (7) slip ring for thermocouple and power supply [5].

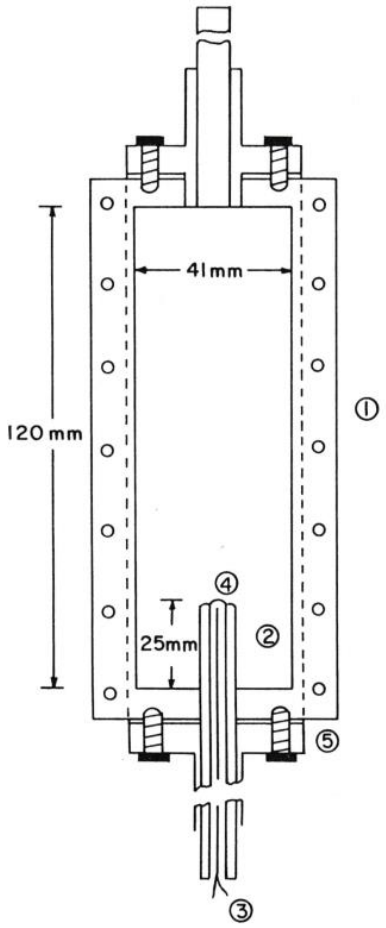

Fig. 5.7 Schematic diagram of the mould used in the mechanical stirring(tumbing) experiments. (1) stainless steel mould (2)cylindrical plunger (3)chromel-alumel thermocouple (4) 4mm glass tube (5) aluminum seal olate [5].

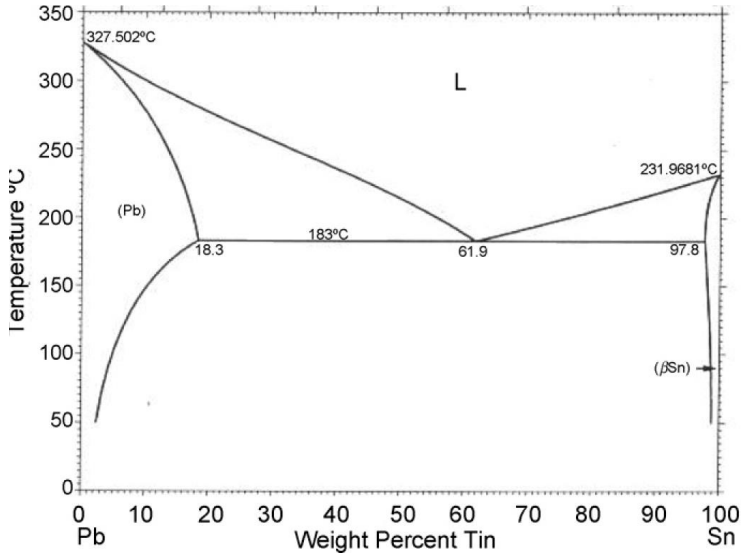

Fig. 5.8. Phase daigarm of Pb-Sn binary alloy [8].

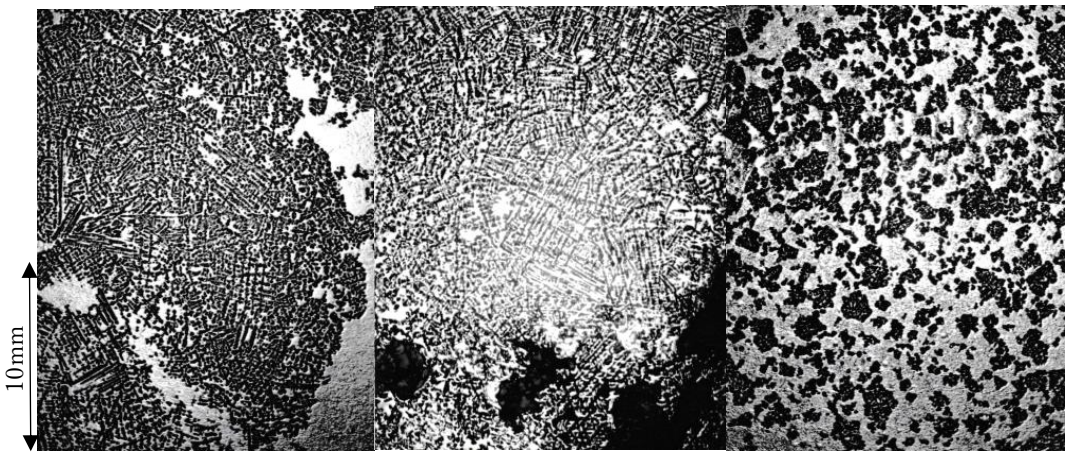

	Tumbled		Tumbling time(min)	Quenched temperature(°C)
	0< fs <0.4	0.4< fs		
E	—	—	non	294 (fs=0.4)
K	—	○	20	289 (fs=0.7)
D	○	—	20	294 (fs=0.4)

Fig. 5.9 Refinement of crystals from the dendritic crystals to the globular crystals by mechanical stirring (tumbling the mould) Note: The refined globular crystals were found in sample D (tumbled 0< fs <0.4). Dendritic equiaxed crystals in sample K were hardly refined with the tumbling at high fraction solid (fs >0.4).

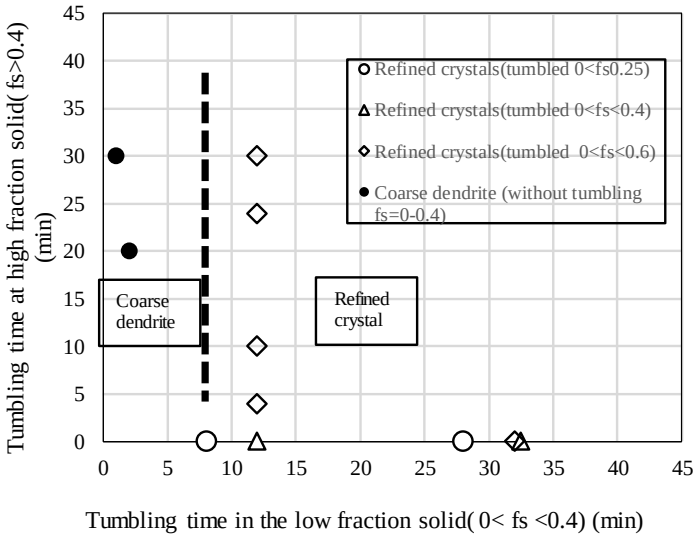

Fig. 5.10 Effect of the tumbling on crystal morophologies of Pb-10%Sn alloy.

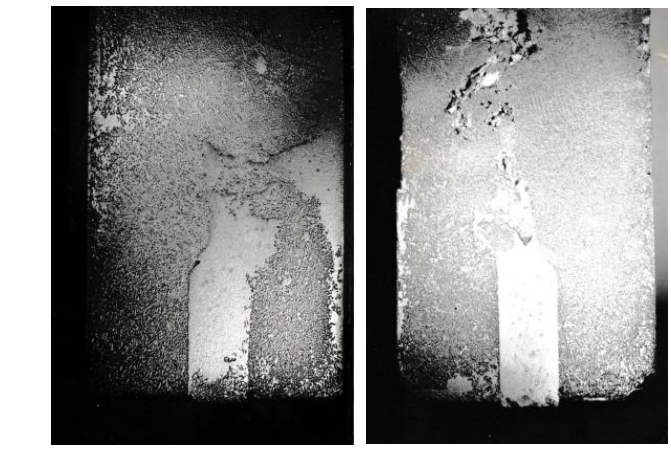

Sample E Sample K

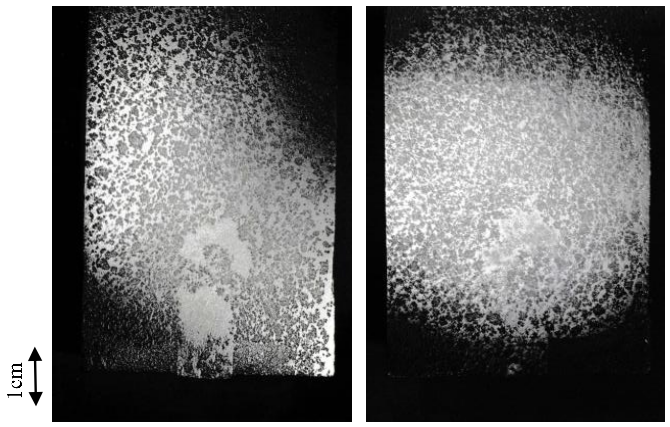

Sample D Sample G

	Tumbled		Tumbling time(min)	Temperature of the creation of a cavity by pulling down a plunger(°C)
	0< fs <0.4	0.4< fs		
E	—	—	non	294 (fs=0.4)
K	—	○	20	289 (fs=0.7)
D	○	—	20	294 (fs=0.4)
G	○	○	20	292 (fs=0.5)

Fig. 5.11. Effects of crystal morphologies on packing the void created by the withdrawn plunger
Note: a mould was kept stationary at the quenched temperature for 180s before creating the cavity.

5.3 Discussion

Laboratory experiments with Pb-Sn alloy have been conducted to explain the effect of EMS on the refinement of internal structure in continuously cast slabs [5]. These analogue study has shown that stirring at low fraction solid is essential to refine crystals. Also unrefined coarse, dendritic crystals do not move easily to fill voids created by bulging or solidification shrinkage; instead inter-dendritic liquid may fill the cavities and create zones of macro-segregation.

The numerical heat analysis on the continuous casting was performed to compare the metallographic findings of the continuously cast slabs with this analogue study. The heat analysis focusing on the interior temperature in the steel slab, however, is not easy, as compared to that on the surface temperature analysis, because of the lack of the measured temperature of the interior of slabs in the real process. Moreover, the heat generation due to solidification in a mushy zone is not sufficiently relevant and the reported formulae of the solidus temperature have not been confirmed with the reliable measurements. For example, significant discrepancies exist between the thermoanalytical measurements of the small specimen and the values obtained from the reported formulae (up to 40K) or the thermodynamic calculations (up to 50k) [10]. To overcome these issues, Fujimura and Brimacombe [11] and Fujimura, Takeshita, and Suzuki [12] obtained the approximate analytical solutions of the heat- and solute transfer equations assuming the linear heat generation in a mushy zone with respect to temperature. It was shown the solutions for continuous casting of the steel were consistent with Neumann's solution in the low carbon concentration range and the conventional numerical heat analysis, such as the equivalent specific heat method. Based on these studies, the numerical heat analysis of the continuously cast slabs by the equivalent specific heat analysis with the upwind finite-deference method was demonstrated assuming a linear heat generation in a mushy zone with respect to temperature. A symmetric condition was used at the center of a slab. The surface temperature at the early stage and both at the middle and final stage was calibrated with the reliable analysis based on the measurements by Meng and Thomas [13] and the typical process data of the caster, respectively. The physical properties, the liquidus temperature [14] and the solidus temperature predicted by the model III used in the analysis are listed in Table 5.2. It is noted that the influence of the stirring by EMS on the solidification was neglected in the heat analysis assuming that the mixing of liquid occurs only in the limited region near the EMS position.

The result of the numerical heat analysis for the case of 1.0m/min (liquid core ratio fc=0.2) was shown in Fig. 5.12. The position of the white band due to No.2 EMS measured directly in the transverse section of the fully solidified slab was also shown in Fig.5.12. The solid fraction fs at the position of white band roughly corresponds to that of 0.1 predicted by the numerical heat analysis. The exact fraction solid of the white band, unfortunately, is not sufficiently relevant even though many of the investigations focusing on white band [9,16] were conducted. However, it is considered that white band could be formed in the range from fs=0 to fs≒ 0.7(at fs>0.67, the liquid in a mushy zone cannot freely move) [9]. Thus, it is considered, at least, that the result of heat analysis is not unreasonable. Table 5.3 shows the summary of the results of both the continuous casting of steel slabs and the analogue study by Pb-Sn alloy on the refinement of crystals. The estimated fraction solid $\overline{f_s}$ defined as an averaged fraction solid in the liquid core within the white bands was 0.15 for

case A(fc=0.07) where only coarse dendritic crystals were observed. In contrast to A, the estimated $\overline{fs}$ of B(fc=0.2) and C(fc=0.37) were 0.02 and 0.03, respectively, where the refined crystals were observed in a liquid core. These results suggest that the refinement of crystals is obtained by EMS where fraction solid is low but is not obtained at the high solid fraction solid. It should be noted that the liquid core of A was considered to be stirred after coarse dendritic crystals developed, so that these coarse crystals were not refined by the stirring. These findings are, basically, well consistent with the results of the analogue study of Pb-Sn alloy (Table 5.3). Accordingly, it is considered, thus, the refinement of crystal, which is achieved by the stirring at low solid fraction, is advantageous to minimize macro-segregation by the close packing of refined crystals in the unsolidified liquid core of the continuously cast slabs.

Table 5.2 Physical properties used in the thermal analysis

Property			Value
Solid zone	ρ_1	Density	7.7×10^3 Kg/m^3
	C_{p1}	Specific heat	0.77 kJ/kgK
	K_1	Thermal conductivity	30.6 W/mK
Solid and Liquid coexisting zone	L	Heat of fusion	276 kJ/kg
	ρ_2	Density	7.5×10^3 Kg/m^3
	C_{p2}	Specific heat	0.77 kJ/kgK
	K_2	Thermal conductivity	31.8 W/mK
Liquid zone	ρ_3	Density	7.4×10^3 Kg/m^3
	C_{p3}	Specific heat	0.77 kJ/kgK
	K_3	Thermal conductivity	35.0 W/mK
Liquidus temperature (Kawawa,1977)			1793 K
Solidus temperature (Hirai, Kanamaru&Mori,1977)			1748K
Steel composition			0.15%C,0.65%Mn,0.019%Si,0.016%P,0.012%S

Table 5.3 Comparison of the effects of the stirring on crystal morphologies in continuously cast steel slabs and the PbSn alloy

	Sample		A	B	C
Continuously cast slab	Casting speed (m/min)		0.7	1.0	1.3
	Conditions of No.2 EMS	fc: liquid core ratio	0.07*	0.2*	0.37*
		$\overline{fs}$: averaged solid fraction in the liquid core (within the white bands)	0.15**	0.02**	0.03**
	Crystals observed in the liquid core		Coarse dendritic crystals	Refined crystals	Refined crystals
Analogue study by Pb-10%Sn alloy	Sample		K	D	G
	fs: solid fraction at which a mould was tumbled		0.4~0.7	0.0~0.4	0.0~0.5
	Crystals typically observed in the samples		Coarse dendritic crystals	Refined crystals	Refined crystals

(*) the ratio of the thickness of the unsolidified zone between the upper and bottom white bands relative

to the slab thickness

(**) Estimated by the numerical heat analysis

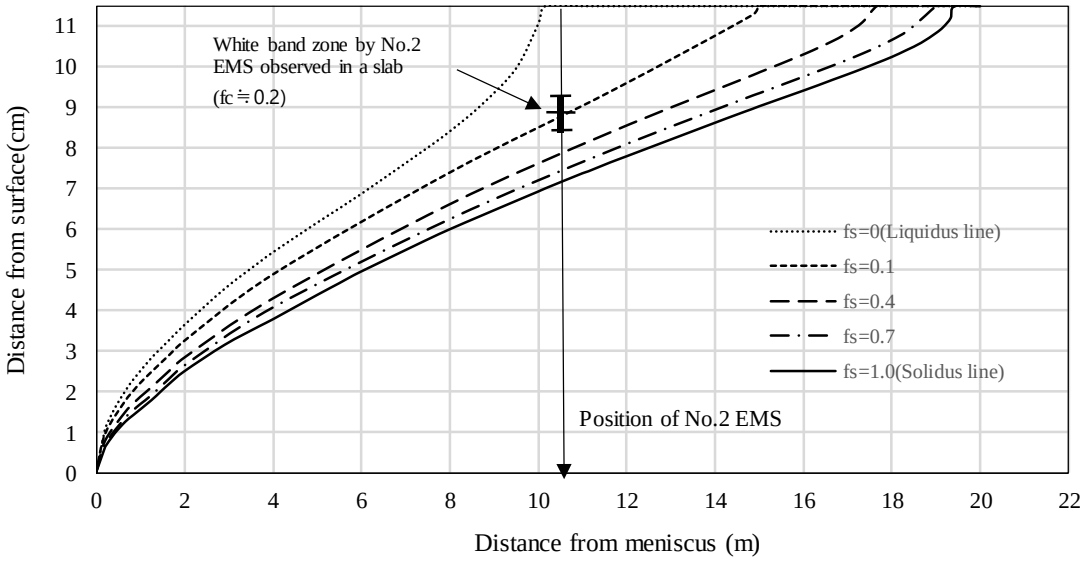

Fig. 5.12. Development of shell thickness of the continuously cast steel slabs estimated by a numerical heat analysis (Mesh size of the thickness :0.00575cm, Mesh size of time:2.5×10^{-5} s, Casting speed: 1.0 m/min, Super heat in a mould :15K, Liquids temperature: 1798K, Solidus temperature:1748K, Steel composition: 0.15%C, 0.65%Mn, 0.019%Si, 0.016%P, 0.012%S)

5.4 Conclusion of this Chapter

The metallographic observations of the continuously cat steel slabs showed that the electro-magnetic stirring applied at low fraction solid refined crystals (globular crystals). The central region of the continuously cast steel with the optimum stirring was well packed with the refined crystals whereas it was not with coarse equiaxed crystals. The analogue study with experiments of Pb-Sn alloy showed that the stirring at the low fraction solid was essential to refine crystals as found in the real process. It was also found the artificial cavity in a mush made during solidification was well packed with the refined, globular, crystals whereas it was not with the coarse dendritic crystals. Thus, hence, it is considered the stirring in the low fraction solid is important to refine crystals and improve macro-segregation in continuously cast steel slabs.

References

[1] T.Saeki,T.Komai,K.Miyamura,S.Mizoguchi and H.Kajioka, Application of Spot Segregation Evaluating Method in Continuouly Cast Slabs, Steelmaking Proceedings, ISS 68 (1985) 229-235.

[2] N.Ohashi, Effect on Ftracure Thoghness of steel, Tetsu-to-Hagane 72 (1986) 747-757.

[3] K.Yamanaka, The Microstrucure and Thoghness of Steels Corresponding to the Chemical Composition of the Segregated Zone of the Plate, Tetsu-to-Hagane 66 (1980) 1367-1373.

[4] H.Kitaoka,T.Fujimura,T.Nozaki,H.Habu,S.Kakihara,H.Bada,S.Shiraishi and H.Tanigawa, Semimacroscopic Features of Centerline Segregation in CC slabs and Their Effects on Product Quality, Tetsu-to-Hagane 69 (1983) A201.

[5] T.Fujimura,E.Takeuchi and J.K.Brimacombe, Segregation Phenomina in the Continuous Casting of Steel Slabs,Japan-Canada Seminar onSecondary Steelmaking,pp.C-5-1-15,December 3-4,1985,Tokyo,Japan,The Iron and Steel Institute of Japan,Tokyo

[6] T.Fujimura,H.Yamasaki,T.Katano and M.Kajiwara, Effect of Elctro Magnetic Stirring on The Centerline Segregation of Continuously Cast Steel,70th Steelmaking conference, AIME (1987) 213-217.

[7] O.Haida,H.Kitaoka,Y.Habu,S.Kitahara,H.Bada and S.Shiraishi, Macro- and Semimacroscopic Features of Centerline Segregation in CC slabs and Their Effects on Product Quality,Trans.ISIJ 24 (1984) 891-898.

[8] S.Gouttebroze,V.Fachimotti,M.Bellet and C.Herve, 3D-FEM Modeling of Microsegregation in Solidification of Binary Alloys,Int.J.Forming Process, 8 (2005) 213-217.

[9] T.Takahashi,M.Kudoh and S.Nagai, Estimation of Effective and Specific Permiability in the Mushy Zone of Steel Ingot by the Method of Seepage into Cylindrical Hole,Tetsu-to Hagane 68(1982) 623-632.

[10] K.Gryc,B.Smetana,M.Zaludova,K.Michalek,P.Klus,M.Tkadleckpva,L.Socha,J.Dobrovska,P.Machovcak, L.Valek,R.Pachlopnik and B.Chmiel, Determination of the Solidus and Liquidus Temperatures of the Real-Steel Grades with Dynamic Thermal-Analysis Methods,Mater.Technol. 47(2013) 569-575.

[11] T.Fujimura and J.K.Brimacombe, Mathematical Analysis of Solidification Behavior of Multicomponent alloys,Trans.Iron Steel Inst. Jpn. 26(1986) 532-539.

[12] T.Fujimura,K.Takeshita and R.O.Suzuki, Mathematical Analysis of the Solidification Behavior of Plain Steel Based on Solute-and Heat- trnsfer equations in the Liquid-Solid Zone, Metall.Mate.Trns. B49 (2018) 644-657.

[13] Y.A. Meng, B.G. Thomas, Heat-Transfer and Solidification Model of Continuous Slab Casting: CON1D,

Metall. Mate. Trans. B34 (2003) 685–705.
[14] T. Kawawa, Tekko-no-Gyouko (Solidification of steel), Appendix 4, ed. By Solidification Comm., Joint Sc. on Iron and Steel Basic Research of ISIJ, ISIJ, Tokyo, 1977.
[15] M. Hirai, K. Kanamaru and H. Mori, Tekko-no-Gyouko (Solidification of steel), Appendix 4, ed. By Solidification Comm., Joint Sc. on Iron and Steel Basic Research of ISIJ, ISIJ, Tokyo, 1977.
[16] Y. Ujiie, H. Maede, Y. Itoh, S. Ogibayashi, H. Seki, K. Wada and Y. Itoh, Improving Solidification Structure of Continuously Cast steel by Electro Magnetic Stirring, Tetsu-to-Hagane 67 (1981) 1297-1306.

Chapter 6

Conclusion

The approximate analytical solutions of the nonlinear heat- and solutes- transfer equations in the mushy zone of the multicomponent alloy steel were obtained through the three models developments (Model I, II, III). The solidus temperatures which strongly depend on the steel composition of the steel were obtained as the parts of the solutions. Because the solidus temperature of the general steel was not well clarified due to the difficulties of measurements in the real casting process. Neither analytical nor approximate solutions exist that describes the relation between the size of the mushy zone and the volumetric energy generation.

In Model I, the basic mathematical treatments to simultaneously solve the heat- and solutes transfer equations were developed adopting the simple boundary conditions (Dirichlet conditions) and the measured solidification constants. The linear relation between the solid fraction and temperature in the mushy zone of the general steel was also assumed. The good agreements of the model predictions and measurements suggested that the basic mathematical treatments developed in Model I seemed to be fair.
Model II adopted the general boundary conditions for the mushy zone, Neumann conditions, were adopted to obtain the consistency of the model with the numerical heat analysis. The Dirichlet conditions were also adopted. The Fe-C plain binary steel was chosen to make the model as simple as possible. The model predictions were in good agreement with the numerical analyses and were also consistent with Neumann's solution for the pure metal at the low carbon range.

In Model III, the binary alloy model (Model II) was expanded to the multicomponent alloy steel to obtain the solidus temperatures of the various grades steel. The solutions of Model III agreed well with the numerical heat and solute analyses and also with Neumann's solution at the low carbon range. The predicted solidification constants and the effective partition ratios of solutes were also found to be in good agreement with both the reported measurements. Good agreements of the model predictions and shot bullet measurements were obtained. The predicted solidus temperatures for various grade steels were in reasonable agreement with the measured ZDT and the reported thermo-analytical measurements. The present model also showed that

conventional heat analyses (such as an equivalent specific heat method) that use solidus temperatures predicted by the model provided not only temperature but also solute concentrations in the mushy zone with respect to time and positions. Both of them are consistent with the model. Model III provides the approximate analytical solutions that reduce the extensive computational load to search for the unknown solidus temperature with the unclarified solid fraction in the mushy zone.

Then, the predicted solidus temperature was used in the numerical heat analyses to estimate the solid fraction at which the electromagnetic stirring was applied in the continuously cast slabs. These analyses showed the stirring at low fraction solid was important to refine crystals and to improve the macro-segregations, centerline segregations in the continuously cast steel.

ACKNOLEDGEMENT

First and foremost, I would like to express my sincerest thanks and gratitude to Professor Ryosuke. O. Suzuki, Hokkaido University for the continued support, guidance and suggestions to my research works. All works were resumed with his guidance, finding the problem of the solidus temperature still remained after 30 years working on the industrial developments and management of workshops. Thank you for all the valuable suggestions and for supporting this study.

I would also like to extend my sincere thanks to Prof. Kunimasa Takeshita, Fukui University for the valuable suggestions to my research works. He has been a good friend who has dedicated himself to numerical modeling of solidification in the early 1980s. His woks were closely related to the works involved in this study and greatly encouraged the present study. I also thanks to Professor Katsutoshi Ono, Kyoto University for his warm continued support for this study.

I specially extend my thanks to the decedent, Prof. J.K. Brimacombe who supported the development of mathematical modeling of solidification and the laboratory studies made in the University of British Columbia. Many thanks also goes to the old good friends, Professor Eiichi Takeuchi, Osaka University and Prof. Indira Samaraskera, University of Alberta who made good discussions on the research made in 1980s at the Brimacombe laboratory. I also extend the gratitude to Kawasaki steel (JFE steel corporation) for granting the study leave in University of British Columbia, in 1985-1987.

I would also give my deep appreciations to CEO, Eiji Hayashida, JFE HD and Vice President Masashi Terabatake, JFE Steel for their warm support to my research works. I also extend gratitude to Vice President, Dr. Saiji Matuoka and Director Hidehiko Hayashi, JFE techno research corporation for their warm support to the recent works.

September 2018

Toshio Fujimura

LIST OF PUBLICATION

1. T. Fujimura and J.K. Brimacombe, Mathematical Analysis of Solidification Behavior of Multicomponent Alloys, Trans. Iron Steel Inst. Jpn. 26 (1986) 532–539.
2. T. Fujimura, K. Takeshita and R.O. Suzuki, Mathematical Analysis of the Solidification Behavior of Plain Steel Based on Solute- and Heat- Transfer Equations in the Liquid-Solid Zone, Metall. Mate. Trans. B 49 (2018) 644–657.
3. T.Fujimura,E.Takeuchi and J.K.Brimacombe, Segregation Phenomina in the Continuous Casting of Steel Slabs, Japan-Canada Seminar on Secondary Steelmaking,pp.C-5-1-15, December 3-4,1985,Tokyo,Japan, The Iron and Steel Institute of Japan,Tokyo
4. T.Fujimura and J.K.Brimacombe, Effect of Stirring on Crystal Morphologies and Macro-Segregation, Journal of Material Science Research,7 (2018) 37-48.
5. T. Fujimura, K. Takeshita and R.O. Suzuki, Mathematical Analysis of the Solidification Behavior of Multi-Component Steel Based on Solute- and Heat- Transfer Equations in the Liquid-Solid Zone, accepted for publication to International Journal of Heat and Mass Transfer,130 (2019) 797-812.